TRANSFORMATION TOUGHENING OF γ'-STRENGTHENED METASTABLE AUSTENITIC STEELS

by

FRODE STAVEHAUG

Bergsingenjör
Kungliga Tekniska Högskolan
Stockholm, Sweden
(1984)

Submitted to the
Department of Materials Science and Engineering
in partial fulfillment of the requirements
for the degree of

DOCTOR OF PHILOSOPHY

at the

MASSACHUSETTS INSTITUTE OF TECHNOLOGY

June, 1990

Signature of Author $\rule{6cm}{0.4pt}$ Signature redacted

Department of Materials Science and Engineering
May 4, 1990

Certified by $\rule{4cm}{0.4pt}$ Signature redacted

Morris Cohen
Institute Professor, Emeritus
Professor, Materials Science and Engineering, Emeritus
Thesis Supervisor

Certified by $\rule{4cm}{0.4pt}$ Signature redacted

Gregory B. Olson
Professor, Materials Science and Engineering
Northwestern University
Thesis Supervisor

Accepted by $\rule{4cm}{0.4pt}$ Signature redacted

Thomas W. Eagar
Acting Chairman, Departmental Committee on Graduate Students

TRANSFORMATION TOUGHENING OF γ'-STRENGTHENED METASTABLE AUSTENITIC STEELS

by

FRODE STAVEHAUG

Submitted to the Department of Materials Science and Engineering
on May 4, 1990 in partial fulfillment of the requirements for the Degree of
Doctor of Philosophy in Metallurgy

ABSTRACT

Utilizing thermodynamic principles, two series of alloys, based upon the γ'-precipitation hardened A286, containing 4% and 12% chromium, were designed for maximum transformation toughening at room temperature. Pre-cracking was done above the M_d-temperature (highest temperature at which transformation can be induced) in the absence of any transformation.

Detailed observations of crack-tip processes were conducted to examine the interaction between crack propagation and the locally-transforming martensite leading to fracture toughness enhancement. In the absence of transformation, a flat fracture mode is displayed. The presence of the mechanically-induced martensite drastically alters the localization and fracture behavior. The strain-induced martensitic transformation (nucleation at new potent sites created by yielding of the parent austenite) was found to change the shape of the fracture-toughness load-displacement curve from a negative to positive curvature thus delaying the onset of fracture instability to a higher load and larger displacement.

The mechanism responsible for fracture toughness enhancement appears to be essentially the same for both stress-assisted (nucleation at pre-existing nucleation sites) and strain-induced transformation. The martensite is initially formed in front of the crack tip. The associated high strain hardening in this region forces strain localization elsewhere, promoting crack branching and square blunting. In the strain-induced region, continued straining initiates shear fracture in the upper and lower corners of the blunted crack. Continued crack opening then occurs by shear localization along a very narrow region located at a high angle of approximately 75 degrees, until the crack opening displacement becomes so large that the crack can circumvent the transformed region ahead of the blunted crack. This point corresponds to maximum applied load and J_{IC}. Similar features occur in the stress-assisted range but toughening is apparently less effective when the fracture path can follow the more brittle fully transformed zone.

Comparison of observed localization behavior with crack-tip strain distributions predicted by application of a transformation plasticity constitutive model indicates that the pressure sensitivity of strain-induced transformation kinetics (determined by the transformation volume change) is important to the strain redistribution which favors crack-tip branching and localization at a high angle to the primary crack plane. Such modelling may ultimately allow design of transformation kinetics to allow further enhancement of transformation toughening efficiency.

2

Under optimum transformation conditions, a K_{IC} fracture toughness of 348 MPa√m (317 ksi√in) was obtained at a yield strength of 1413 MPa (204 ksi). This is more than twice the toughness of commercial precipitation-hardened steels available at comparable strength levels.

Thesis Supervisor: **Dr. Morris Cohen**
Title: Institute Professor, Emeritus
Thesis Supervisor: **Dr. Gregory B. Olson**
Title: Professor, Materials Science and Engineering, Northwestern University

TABLE OF CONTENTS

LIST OF FIGURES

LIST OF TABLES

ACKNOWLEDGEMENTS

12

CHAPTER 1

INTRODUCTION

Mechanically-induced martensitic transformations can improve uniform elongation, strain to failure, yield strength, ultimate tensile strength, and fracture toughness of metastable austenitic steels. The martensitic transformation is a function of composition, temperature, applied stress, strain rate, stress state, and prior deformation of the parent austenite phase. The essential mechanism for mechanically-induced martensitic transformations is well understood, and constitutive equations have been developed and applied to the uniaxial tension test with good agreement. The toughening effect has not yet been related to constitutive equations because of the complex processes at the crack tip. Knowledge about the explicit interaction between crack propagation and the locally-transforming material is therefore essential to the understanding of fracture-toughness enhancement.

No practical high-strength (σ_y>1300 MPa, 190 ksi) metastable austenitic steel exhibiting exceptionally high fracture toughness at room temperature has previously been developed. Leal [1], investigating various high-strength γ'-strengthened metastable austenitic steels, obtained a maximum J_{IC} fracture toughness of 250 kJ/m^2 (K_{IC}=250 MPa$\sqrt{m}$) at -25°C, while Young [2], investigating high-strength phosphocarbide-strengthened metastable austenitic steels, reached 180 kJ/m^2 at 100°C. Because of the large

temperature-sensitivity of the martensitic transformation in these steels, substantial drops in fracture toughness occur in a very narrow temperature range around the optimum temperature. The temperature-sensitivity is related to the effect of alloying and can be predicted and thus altered.

This thesis investigates the nature of the complex crack-tip processes in γ'-strengthened metastable austenitic steels. The enhancement of fracture toughness is directly related to the interaction between crack propagation and the locally-transformed martensite. The characterization of the crack-tip processes is therefore of vital importance in the development of these ultrahigh-toughness steels.

Utilizing thermodynamical principles, two series of alloys have been designed based upon the γ'-precipitation hardened A286: a 4% chromium series and a 12% chromium series. The objective for both series is to obtain maximum fracture toughness at room temperature and to achieve a yield strength of at least 1300 MPa (190 ksi). Furthermore, the 12% stainless series is expected to have a reduced temperature-sensitivity, thus maintaining near-maximum fracture toughness over a wider temperature range.

The two alloy series have been thoroughly characterized. An extensive heat treatment program was conducted to optimize the solutionizing and aging behavior in order to obtain uniform microstructure and high strength. A mechanical testing program has now provided room-temperature tensile properties, fracture-toughness data, and a better understanding of the interaction between crack propagation and the mechanically-induced martensitic transformation leading to fracture-toughness enhancement.

CHAPTER 2

BACKGROUND AND LITERATURE REVIEW

2.1 MECHANICALLY-INDUCED MARTENSITE

Metastable austenitic steels can exhibit large uniform elongation, high strength, and high fracture toughness due to the mechanically-induced martensitic transformation. This austenite-to-martensite phase transformation is a function of temperature, applied stress, composition, strain rate, stress state, and prior deformation of the parent austenite. With these variables, a wide range of mechanical properties is achievable. This thesis emphasizes the toughening enhancement due to the martensitic transformation that is induced by the deformation during testing.

The influence of the above-mentioned parameters on the austenite-to-martensite transformation will be reviewed in this section. The current level of understanding of transformation toughening due to transformation plasticity will be reviewed in Section 2.2. Elastic-plastic fracture mechanics pertaining to transformation toughening will be reviewed in Section 2.3, and finally in Section 2.4 a summary is given of the strength and toughness combinations in commercially-available stainless steels.

16

2.1.1 TRANSFORMATION KINETICS

The martensitic transformation can be triggered by an applied stress at temperatures above M_s, as schematically illustrated in Figure 2.1 [3]. M_s^σ defines the highest temperature at which an applied elastic stress induces martensitic transformation. Below M_s^σ, the nucleation is termed stress-assisted because nucleation takes place at preexisting nucleation sites. Above M_s^σ, plastic flow precedes the martensitic transformation; the plastic deformation creates new nucleation sites and the nucleation is termed strain-induced. M_d defines the highest temperature at which martensitic transformation can be induced by plastic deformation.

The martensites formed in the different regimes reveal different morphologies [4]. For stress-assisted nucleation, a plate morphology is observed while a lath morphology is predominant for strain-induced nucleation. Around the M_s^σ temperature, the morphology is mixed.

Figure 2.2 shows typical stress-strain $(\sigma\text{-}\varepsilon)$ and volume fraction martensite versus strain $(f\text{-}\varepsilon)$ curves for a TRIP steel [4]. The $\sigma\text{-}\varepsilon$ curves initially, at some temperatures, exhibit a positive curvature. At low temperatures, the $f\text{-}\varepsilon$ curves exhibit considerable linearity, while at higher temperature a sigmoidal shape is observed. The details of these interrelationships will be discussed later.

2.1.1.1 General Mechanism and Kinetics

The stability of the parent austenite depends on its chemical composition. The relative effect of different elements on the stability can be denoted by the M_s-temperature. Figure 2.3 shows that, for iron-base binary alloys, substitutional elements have a mixed influence on the M_s-temperature, whereas the interstitial elements carbon and nitrogen lower the M_s-temperature [5].
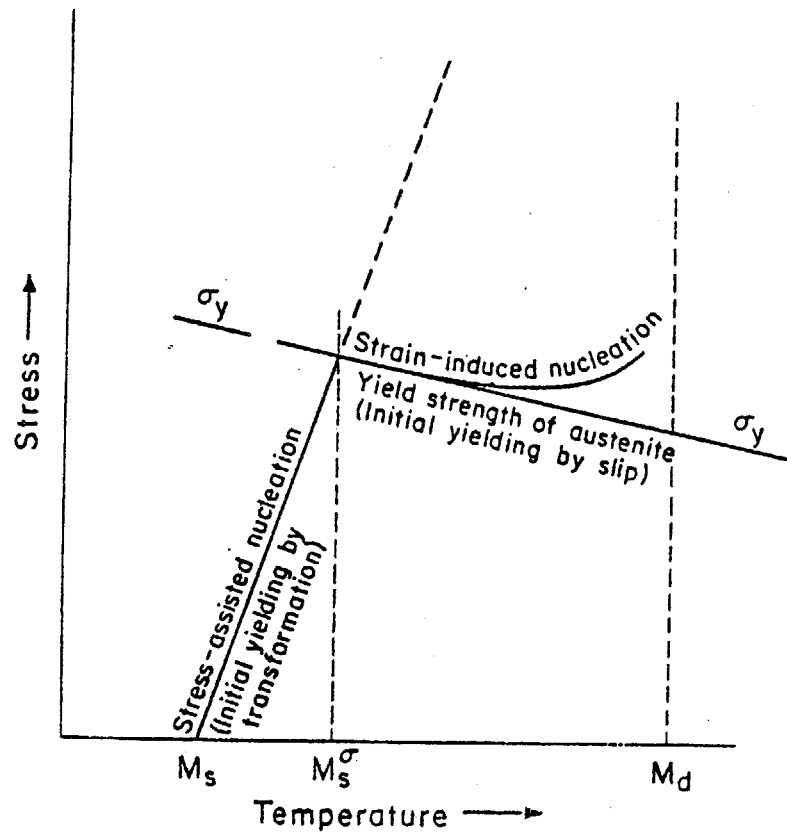
Figure 2.1 Schematic representation of interrelationships between stress-assisted and strain-induced martensitic transformation [3].

18
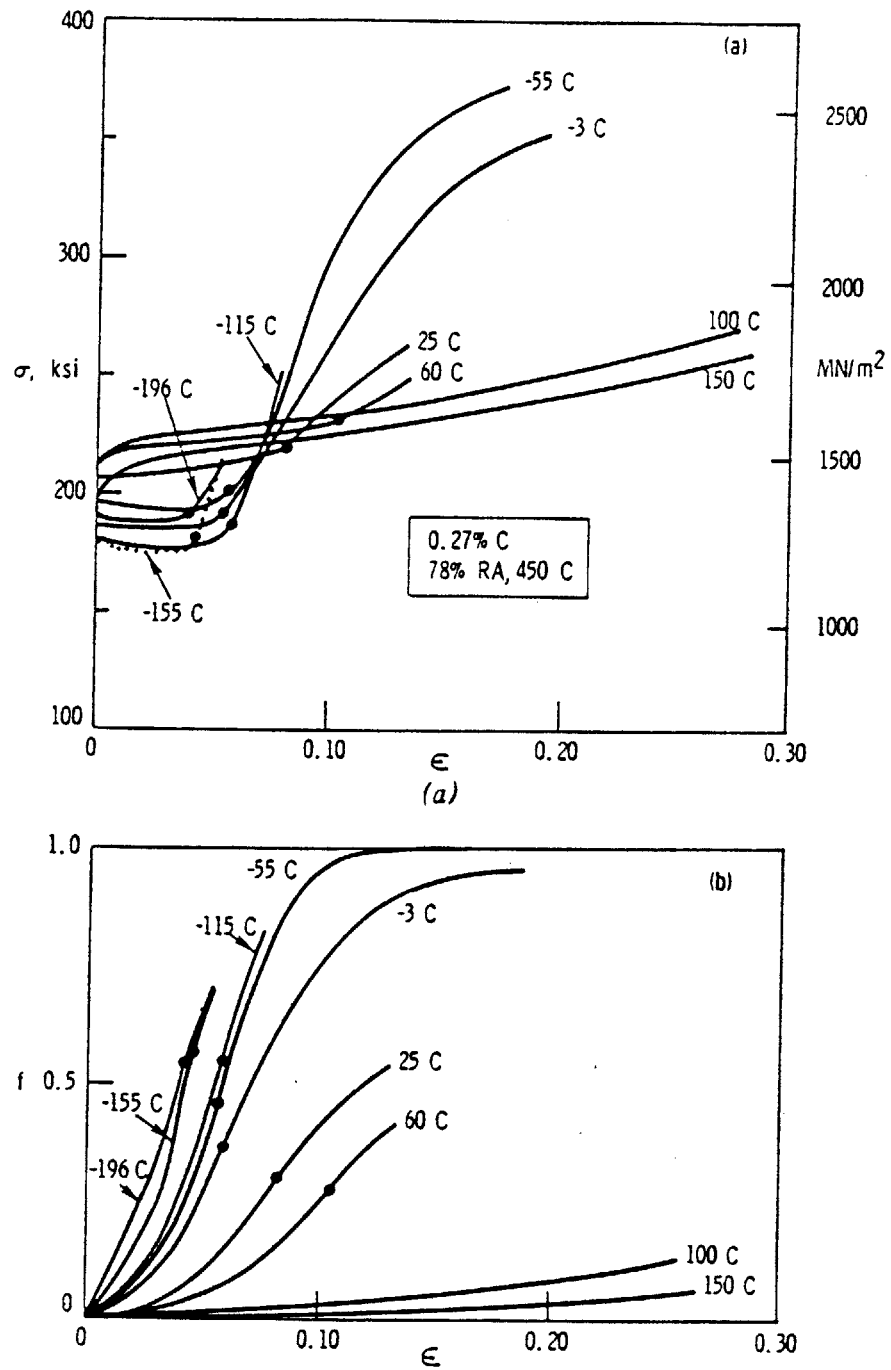
Figure 2.2 Tensile properties and transformation curves for 0.27C TRIP steel in warm-rolled condition (78pct RA, 720K). a) σ-ε curves, b) f-ε curves. Heavy points represent values at Lüders strain [4].

19
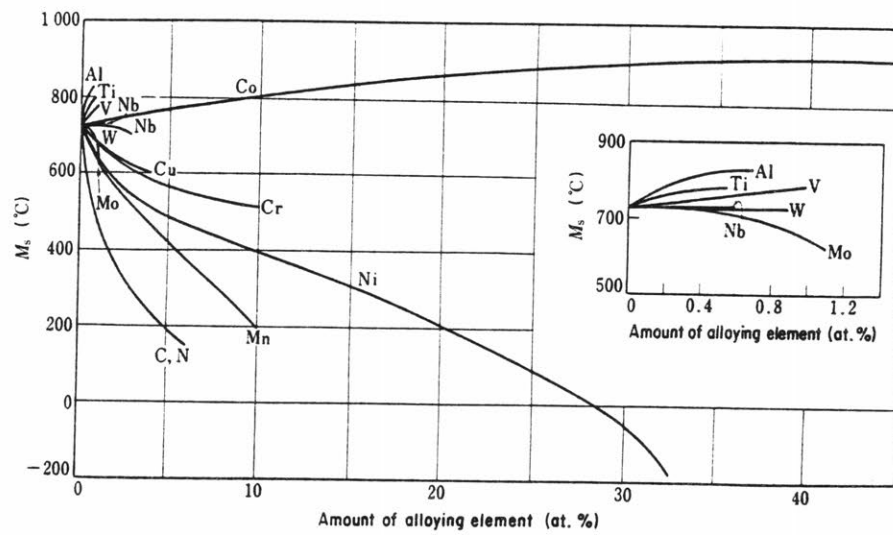
Figure 2.3 M_s-temperatures of some Fe-base binary alloys [5].

In ternary iron-base alloys the separate effects on the M_s-temperature by the interstitial elements carbon and nitrogen are approximately additive relative to one another, but not with respect to substitutional elements. The effect of substitutional elements are generally additive relative to each other with a few exceptions [6]. With addition of a third element to iron-nickel alloys, the M_s-temperature varies as shown in Table 2.1 [5].

Table 2.1 Effect of third elements on the M_s-temperature of some Fe-Ni alloys.

Fe-Ni(%) (weight percent)	Cr	Mo	Ni	Ti	V	Al	Si	Mn
22.5	down		down	up/down	up/down	no change	up/down	
27-30	down	down				no change	down	down
18, 30	down	up			up	down	down	down

up/down: initial increase, thereafter decrease.

Empirical expressions for the M_s-temperatures of low-carbon steels have been developed. The expression below, which is due to Andrews [7], correlates the M_s-temperature to different alloying elements:

$$M_s(°C) = 539-423(\%C)-30.4(\%Mn)-17.7(\%Ni)-12.1(Cr)-7.5(\%Mo) \qquad (2.1)$$

where % is in weight percent. This empirical relationship holds quite well up to the following maximum composition values: C-0.6%; Mn-Ni-Cr-Mo~5%. Because of this limited composition range, M_s-temperatures for high-alloy steels are usually determined separately. Common methods to determine M_s-temperatures are metallography, resistivity measurements, magnetometry, dilatometry, and acoustic emission.

2.1.1.2 Stress-Assisted Nucleation

In the early 50's Kulin et al. [8] found that the M_s temperature is raised by both uniaxial tension and uniaxial compression but is lowered by triaxial and hydrostatic compression. Later Patel and Cohen [9] showed quantitatively that the kinetics of stress-assisted transformation could be treated by adding the mechanical work term to the chemical driving force:

$$\Delta g^{tot} = \Delta g^{ch} + \Delta g^{\sigma} \qquad (2.2)$$

where Δg^{ch} is the chemical contribution and Δg^{σ} is the mechanical contribution to the total driving force Δg^{tot}. The mechanical contribution per unit volume can be expressed as:

$$\Delta g^{\sigma} = -\left(\tau \gamma_0 + \sigma \varepsilon_0\right) \qquad (2.3)$$

where τ and σ are the shear and normal stress components resolved along the operative habit plane, and γ_0 and ε_0 are the shear and normal components of the invariant-plane strain. By expressing the mechanical work term as a function of the orientation of a transforming martensitic plate, Patel and Cohen showed $\partial \Delta g / \partial \sigma$ to be a function of the stress-state. Estimates using the Patel-Cohen model indicated $\partial \Delta g / \partial \bar{\sigma}$, where $\bar{\sigma}$ is the equivalent stress, to be in reasonable agreement with the stress-state dependence of the condition for stress-assisted transformation [10].

During the stress-assisted martensitic transformation, experiments have shown that the relationship between volume fraction martensite, f, and true strain, ε, is linear [4]:

$$f = k\varepsilon. \qquad (2.4)$$

Assuming a constant critical driving force for transformation, Δg^{tot}, as a function of temperature and noting that the mechanical driving force, Δg^{σ}, is proportional to the applied

stress, it can be shown that the slope in the stress-assisted nucleation region, $\partial \sigma_t / \partial T$, where σ_t is the transformation stress, is proportional to the entropy term ΔS [9,11]. The temperature interval $\left(M_s^\sigma - M_s\right)$ can therefore be changed through alloy modification.

2.1.1.3 Strain-Induced Nucleation

While the M_s-temperature is related to the stability of the parent austenite, the temperature interval $M_d - M_s$ depends on the stacking-fault energy of the parent austenite. Tamura et al. [12] determined the $M_d - M_s$ temperature interval for the alloys shown in Table 2.2.

Table 2.2 $M_d - M_s$ temperature interval for some iron alloys.

ALLOY	$M_d - M_s$ (°C)
Fe-29Ni-0.26C	85
Fe-19Cr-11Ni	200
Fe-24Mn-0.26C	440

It can be seen from Table 2.2 that manganese creates a very wide $M_d - M_s$ interval while nickel gives a narrow $M_d - M_s$ interval, with chromium somewhere in between manganese and nickel. The addition of chromium or manganese to an iron-nickel alloy will therefore promote a lower temperature-sensitivity, and optimum mechanical properties can thus be retained over a wider temperature interval. Tamura et al. attribute the difference in the $M_d - M_s$ interval to the different types of martensite formed. α'(bcc/bct) martensite is formed in Fe-Ni and Fe-Ni-C alloys, ε'(hcp) martensite is predominant in Fe-high Mn alloys, while Fe-Ni-Cr exhibits a mixture of both α' and ε' martensite. The different types

of martensite produced can be related to the stacking-fault energy (SFE) of the parent austenite. ε'-martensite tends to form in austenite with low stacking-fault energy. Furthermore, the critical driving force for the $\gamma \rightarrow \varepsilon'$ transformation is relatively low in comparison with that for the $\gamma \rightarrow \alpha'$ transformation. The ε'-martensite is therefore more easily induced by strain than α'-martensite.

α'-martensite is known to nucleate at intersections of shear bands which may be in the form of ε'-martensite, mechanical twins, or stacking faults [13,14]. Lecroisey and Pineau [15] observed that in high stacking-fault energy systems, such as Fe-Ni and Fe-Ni-C alloys with SFE=50-60 ergs/cm^2, α'-martensite is formed on twins and grain boundaries while in intermediate stacking-fault energy systems, such as Fe-Ni-Cr alloys with SFE=20-30 ergs/cm^2, α'-martensite nucleates at the intersection of ε'-martensite plates and on deformation twins. As the temperature is increased, the amount of ε'-martensite is decreased and α'-martensite then forms on deformation twins. In Fe-Mn alloys where the stacking-fault energy is low and of the order of 5 ergs/cm^2, the critical driving force for the $\gamma \rightarrow \alpha'$ transformation is too high even with the possibility of nucleation on the ε'-martensite. Therefore, rarely is α'-martensite observed in austenitic Fe-Mn alloys. In almost all such cases, only the ε'-martensite forms.

By selecting different alloying elements, it is therefore possible to change both the M_s-temperature and the stacking-fault energy which modifies the M_d-M_s temperature interval, thus retaining optimum mechanical properties over a wider temperature interval.

Experiments have shown that the f-ε relationship for strain-induced martensitic transformation, as mentioned earlier, is sigmoidal [4,16]. A quantitative model for these observations has been developed using shear-band intersections as the nucleation sites [17]. The volume fraction of shear bands, f^{sb}, is assumed to be related to plastic strain, ε, by:

$$f^{sb} = 1 - \exp(-\alpha\varepsilon) \tag{2.5}$$

where α is a strain-independent constant but dependent on stacking-fault energy and strain rate. If $\overline{v}^{sb}$ is the average volume of a shear band, the number of shear bands per unit austenite volume is:

$$N_V^{sb} = \frac{f^{sb}}{\overline{v}^{sb}}. \tag{2.6}$$

It is then assumed that the number of shear-band intersections per unit austenite volume, N_V^I, can be related to N_V^{sb} by a simple power law expression of the form:

$$N_V^I = K\left(N_V^{sb}\right)^n \tag{2.7}$$

where K is a geometric constant and $n \geq 2$. The incremental increase in the number of α' martensitic embryos produced per unit austenite volume, $dN_V^{\alpha'}$, can be related to an increase in the number of shear-band intersections by:

$$dN_V^{\alpha'} = pdN_V^I \tag{2.8}$$

where p is the probability that a shear-band intersection will generate a martensitic embryo. Assuming a Gaussian distribution of the potency of intersections as nucleation sites, p will have the form of a Gaussian cumulative function with respect to chemical driving force. If ΔS is constant in the temperature range of interest, p will also have the form of a Gaussian cumulative function with respect to temperature [17].

In agreement with experimental observations, confining the strain-induced transformation to shear band intersections only, the average volume per martensitic unit, $\overline{v}^{\alpha'}$, is taken to be constant. The incremental increase in the volume fraction of martensite per unit volume of alloy can therefore be related to the increase in number of embryos per unit untransformed austenite by the expression:

$$\frac{df^{\alpha'}}{\left(1-f^{\alpha'}\right)} = \overline{v}^{\alpha'}dN_v^{\alpha'}.$$

(2.9)

Adopting the previous assumptions, substituting their expressions into Eq.(2.9), and integrating gives the following expression:

$$f^{\alpha'} = 1 - \exp\left\{-\beta\left[1-\exp\left(-\alpha\varepsilon\right)\right]^n\right\}$$

(2.10)

where $\beta = \dfrac{\left(\overline{v}^{\alpha'}Kp\right)}{\left(\overline{v}^{sb}\right)^n}.$

Eq. (2.10) shows a sigmoidal shape and approaches saturation level below 100 percent as seen in Figure 2.4. The saturation level is controlled by the β parameter while the rate of approach to saturation is controlled by both the α and β parameters.

The temperature dependence of strain-induced transformation kinetics is governed by the α and β parameters in Eq. (2.10). The α parameter, dependent on stacking-fault energy and strain rate, is temperature dependent through the temperature dependence of the stacking-fault energy. This temperature dependence has been attributed to the fcc-hcp entropy difference [15] which, as mentioned earlier, can be changed by alloy modification.

Thermomechanical treatment of the parent austenite is often employed on metastable austenitic steels. This raises the yield strength, σ_y in Figure 2.1. However, large deformations tend to stabilize the austenite mechanically while concurrent carbide precipitation (removal of carbide from solution) decreases the austenite stability chemically [18]. Therefore, the M_s temperature can be either lowered or raised, depending on the extent of prior deformation and on the amount of carbide precipitation. The change in M_s^σ temperature becomes more complex because of possible changes in the entropy of the

26
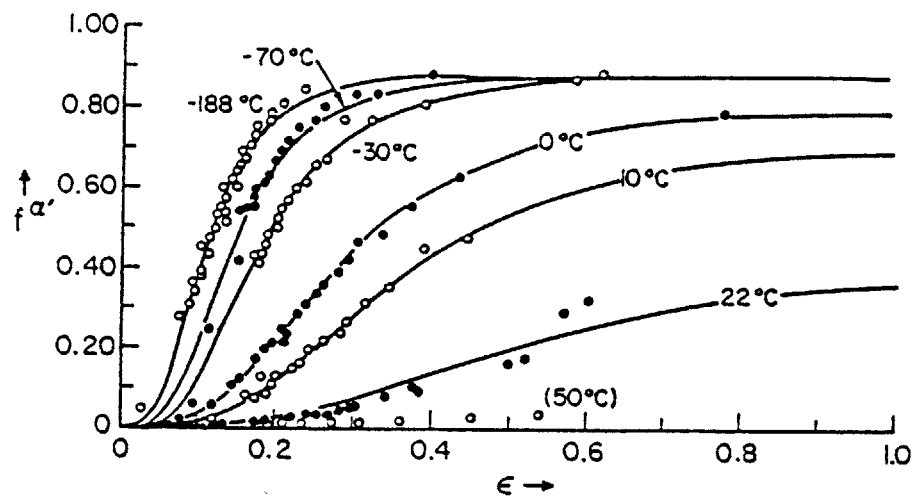
Figure 2.4 Comparison of calculated transformation curves with data for a 304 stainless steel. Experimental data are indicated by points. The solid curves represent the best fit of Equation 2.10 for each temperature dependence of the α and β parameters [17].

austenite-to-martensite transformation due to both the deformation and possible precipitation processes. Typically, the M_s^σ temperature is raised by prior deformation of the parent austenite in alloy systems with accompanying carbide precipitation , while the M_s^σ temperature is normally lowered if no carbide precipitation occurs.

Powell et al. [19], and Bressanelli and Moskowitz [20] studied the effect of strain rate on metastable austenitic stainless steels. Increasing the strain rate from 0.006 to 0.06 min^{-1} stimulated martensite formation, whereas further increases resulted in less transformation [19]. Bressanelli and Moskowitz [20] investigated strain rates greater than 0.05 min^{-1} and found that, with tensile specimens tested in air, an increase in strain rate decreased the amount of martensite formed due to adiabatic heating of the test specimen. When the same test was conducted in a water bath, no changes in the extent of transformation were found as a function of strain rate, because of the fast dissipation of heat away from the test specimen. The yield stress is increased as the strain rate is increased, but the M_d temperature does not change. An increase in yield stress usually gives an increase in the M_s^σ temperature if no other parameters affect the martensitic transformation, as discussed earlier.

Different stress states, as mentioned previously, affect the martensitic transformation through the mechanical work contribution, Δg^σ. Efforts to quantitatively express the M_s^σ temperature variation as a function of different stress states have thus far had only limited success. Experiments have shown that a higher triaxial stress state contributes more to the mechanical work, Δg^σ, giving rise to increasing M_s^σ temperature in the following order: hydrostatic pressure, biaxial compression, uniaxial compression, pure shear, uniaxial tension, biaxial tension, and the triaxial crack-tip case.

2.1.2 CONSTITUTIVE EQUATIONS

The σ-ε and f-ε curves depicted in Figure 2.2 reveal, in addition to the static hardening contribution of the transformation product, that there is an initial dynamic softening associated with the martensitic transformation. This dynamic softening is most predominant at low strains, causing the curvature of the stress-strain curve to become positive. The dynamic softening is attributed to the martensitic transformation as a deformation process, i.e., the macroscopic strain accompanying the martensitic transformation under an applied stress. This transformation plasticity increases the amount of strain initially causing the stress to drop. The initial stress drop is increased by increasing prior deformation of the parent phase. As deformation proceeds the strain-hardening effect counteracts the dynamic softening, causing the stress level to rise and the curvature $\left(\rho \sim \dfrac{d^2\sigma}{d\varepsilon^2}\right)$ to change from positive to negative.

2.1.2.1 Stress-Assisted Martensitic Transformation

By using the thermodynamics and kinetic theory of martensitic nucleation, Olson and Cohen [10] have developed constitutive relations predicting the dependence of flow stress, σ_t, on temperature, strain, strain rate, and stress-state, consistent with the observed behavior of TRIP steels. The flow stress during stress-assisted transformation can be expressed as:

$$\sigma_t(f,\dot{f},T) = -\left[B\frac{\partial\Delta G}{\partial\sigma}\right]^{-1}\left[A+B\Delta G^{ch}+RT\ln\left(\frac{\dot{f}}{(n_i + pf - N_v)(1 - f)Vv}\right)\right] \qquad (2.11)$$

where A and B are constants, ΔG is the total driving force, ΔG^{ch} is the chemical driving force, n_i is the initial density of nucleation sites, p is an autocatalytic factor accounting for new nucleation sites created during transformation, f is the volume fraction martensite, N_v

is the number of martensitic plates per unit volume, V is the instantaneous mean plate volume, and ν is the nucleation-attempt frequency. Substituting Eq. (2.4) into Eq. (2.11) generates a constitutive relation for stress-assisted transformation:

$$\sigma_t\left(\varepsilon,\dot{\varepsilon},T\right) = -\left[B\frac{\partial\Delta G}{\partial\sigma}\right]^{-1}\left[A+B\Delta G^{ch}+RT\ln\left(\frac{k\dot{\varepsilon}}{\left(n_i + pk\varepsilon - N_v\right)\left(1 - k\varepsilon\right)V\nu}\right)\right] \quad (2.12)$$

Figure 2.5 shows a comparison of calculated and observed σ-ε curves for a TRIP steel. The model accounts for the initial stress drop but as saturation is approached, the denominator goes to zero, causing the stress to rise abruptly. The discrepancy with the observed more gradual strain hardening is attributed to the assumption of a single activated process involving the most favorable-orientation nucleus as in the Patel-Cohen model [9]. Better agreement is expected by adopting a distribution of nucleus orientations. Recently Olson et al. [21] introduced a distribution of orientations to develop constitutive equations for dispersed austenite obtaining excellent agreement with experiments.

2.1.2.2 Strain-Induced Martensitic Transformation

To quantitatively predict the constitutive equations in the strain-induced regime, another factor has to be incorporated compared to the stress-assisted region. Beyond the kinetics of the martensitic transformation there is general slip. The static hardening effect, associated with the two-phase mixture of martensite and austenite, as well as the dynamic softening has to be considered.

Narutani et al. [22] separated the dynamic softening and static hardening during strain-induced martensitic transformation as shown in Figure 2.6. The experimental σ-ε curve of the metastable austenitic steel is labeled σ_{exp}. The corresponding σ-ε curves of stable austenite and martensite are labeled σ_γ and $\sigma_{\alpha'}$. The dashed curve labeled RM
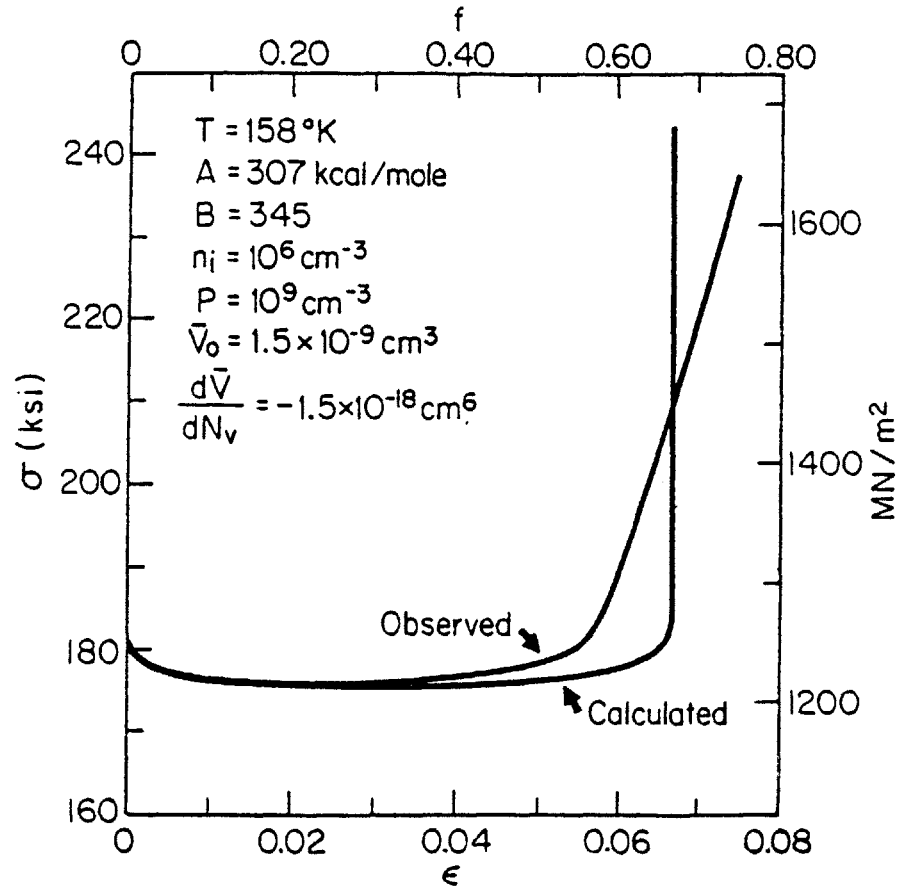
Figure 2.5 Comparison of calculated and observed true σ-ε curves for a TRIP steel [10].
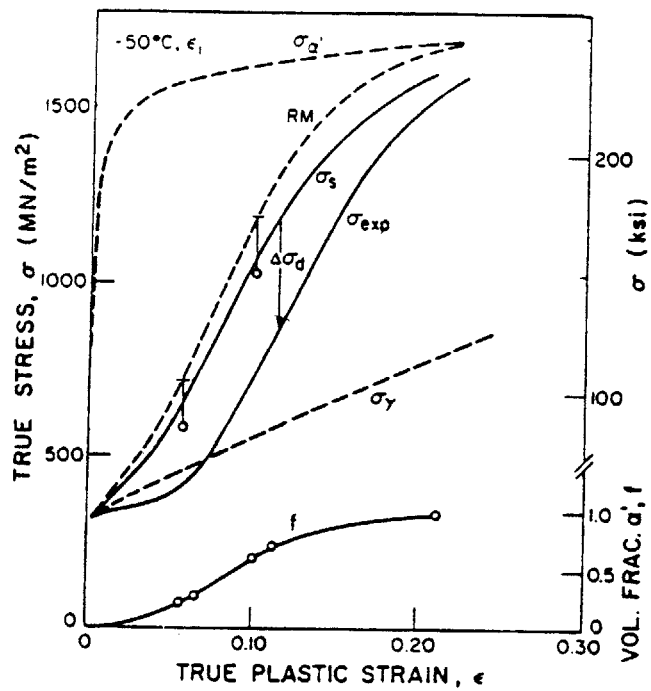
Figure 2.6 Experimental flow stress, σ_{exp}, and volume fraction martensite, f, versus plastic strain, ε, for a metastable austenitic steel [22].

32

represents a σ-ϵ curve calculated from a rule of mixtures based on the assumption that the strain in both the austenite and martensite is equal to the macroscopic plastic strain. During the martensitic transformation, a transformation strain is present that does not correspond to the working of either phase. By subtracting the transformation strain from the total strain, a strain-corrected rule of mixtures can be calculated. This "static-flow stress" is:

$$\sigma_s = [1 - f]\sigma_\gamma(\epsilon - \alpha f) + f\sigma_{\alpha'}(\epsilon - \alpha f). \tag{2.13}$$

The dynamic softening increment, $\Delta\sigma_d$, was then taken as the difference between σ_s and σ_{exp}. The flow stress was thereafter expressed as:

$$\sigma = \sigma_s - \Delta\sigma_d. \tag{2.14}$$

Experiments further showed that

$$\Delta\sigma_d = \beta\frac{df}{d\epsilon}\sigma_s \tag{2.15}$$

where β is a constant. Combining Eqs.(2.13)-(2.15) gives the constitutive equation $\sigma(\epsilon,\dot{\epsilon},T)$ for strain-induced transformation:

$$\sigma(\epsilon,\dot{\epsilon},T) = \{[1 - f]\sigma_\gamma(\epsilon - \alpha f) + f\sigma_{\alpha'}(\epsilon - \alpha f)\}\left[1 - \beta\frac{df}{d\epsilon}\right]. \tag{2.16}$$

Figure 2.7 illustrates the good agreement between calculated and experimental σ-ϵ curves.

Recently Stringfellow [23] has developed a generalized three-dimensional constitutive model, extending on the one-dimensional Narutani-Olson-Cohen model referred to above. Excellent agreement was obtained when compared with the experimental work by Leal [1]. Stringfellow was able to model the triaxiality in a necking tensile specimen and observed that transformation plasticity decreases the triaxiality. At the
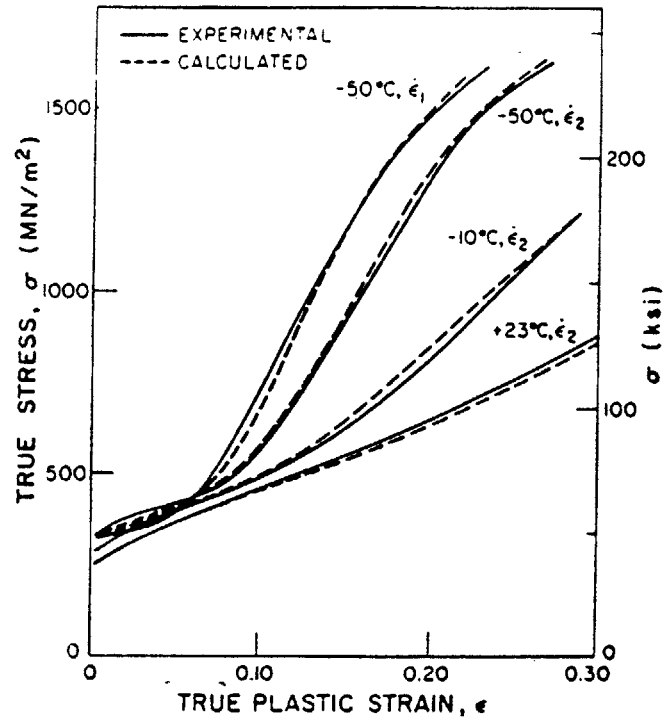
Figure 2.7 Comparison of $\sigma_{exp}(\varepsilon)$ curves of Figure 2.6 with calculated curves from Equation 2.16. $\varepsilon_1 = 2.2*10^{-4}\text{s}^{-1}$; $\varepsilon_2 = 5.6*10^{-3}\text{s}^{-1}$ [22].

34

present time, he is incorporating pressure-sensitivity into the constitutive model to further refine the calculations [24].

2.2 PLASTIC INSTABILITY AND TRANSFORMATION TOUGHENING

The σ-ε curves of metastable austenitic steels display, at certain temperatures, an initial positive curvature. Because of this, the necking (plastic instability) condition:

$$h = \frac{d\sigma}{d\varepsilon} \leq \sigma \tag{2.17}$$

where h is the strain-hardening rate, is met immediately. Figure 2.8 [2] shows the normalized hardening rate, h/σ, versus plastic strain, ε, for a metastable austenitic steel at two different temperatures corresponding to $\theta=0.6$ and $\theta=1$, where

$$\theta = \frac{T - M_s^\sigma}{M_d - M_s^\sigma} \tag{2.18}$$

is a normalized temperature parameter; thus $\theta=0$ at $T=M_s^\sigma$ and $\theta=1$ at $T=M_d$. For stable austenite, $\theta \geq 1$, h/σ decreases monotonically as represented by the dashed line. Final fracture occurs at b, where h/σ intersects the critical h/σ calculated from the Needleman-Rice criterion for shear localization controlled by void growth [25]. For $\theta=0.6$, initial flow localizes in a Lüders band at point d. As the strain-hardening, h, increases, flow delocalizes at point c and becomes homogeneous. Thereafter, the entire test specimen deforms uniformly. The strain hardening decreases in magnitude and final necking occurs when $h/\sigma<1$ at a'. The final ductile fracture takes place by shear localization at b'. From these results, it is clear that the martensitic transformation is beneficial by delaying the onset of necking from point a to point a', as well as increasing the total fracture strain from point b to point b'. Leal [1] measured a four-fold enhancement of uniform strain as well as a

35
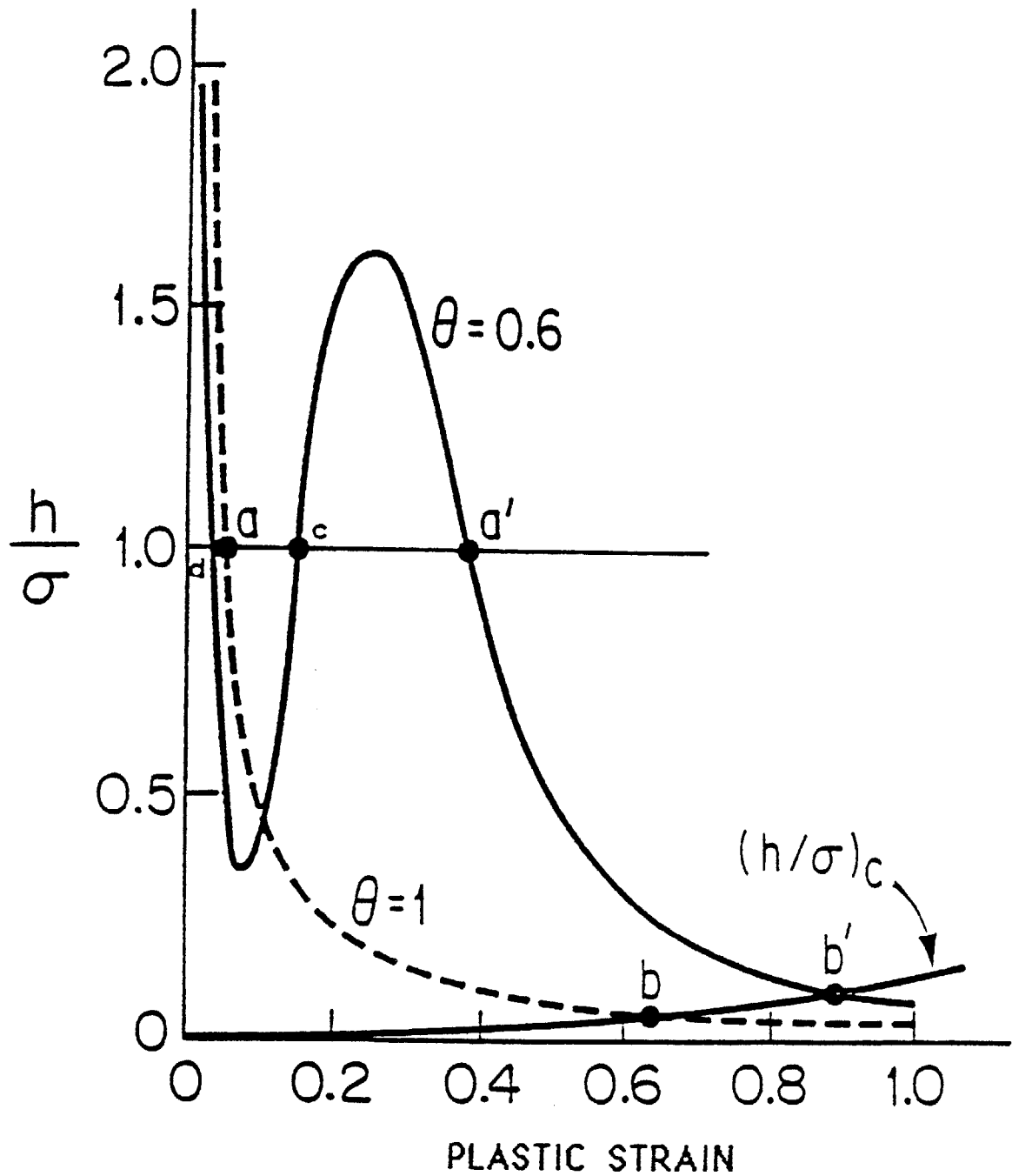
Figure 2.8 Normalized strain-hardening rate h/σ vs. plastic strain for a γ'-strengthened metastable austenite at $\theta=1$ ($T=M_d$) and $\theta=0.6$ $\left(M_s^\sigma<T<M_d\right)$. Horizontal line, $h/\sigma=1$, corresponds to tensile necking condition, while $(h/\sigma)_c$ is condition for shear-instability-controlled fracture in tensile neck [2].

60% enhancement of fracture strain in his metastable austenitic steels. These results are shown in Figure 2.9.

Transformation plasticity also enhances the fracture toughness in high-strength TRIP steels where fracture is controlled by shear instability. Leal [1] found K_{IC} values as high as 250 MPa$\sqrt{m}$ (228 ksi$\sqrt{in}$) at a yield strength of 1300 MPa (190 ksi). Figure 2.10 summarizes the measured relative J_{IC} enhancement versus the normalized temperature θ. For $\theta > 0$, i.e., strain-induced transformation, failure occurred by shear localization while for $\theta < 0$, i.e., stress-assisted transformation, a flat fracture mode was observed. Metallographic observations revealed the formation of fine strain-induced martensite for the shear fracture, while plate martensite dominated in the flat fracture mode. The alloys with larger volume change accompanying the transformation, denoted HV, are seen to give a higher toughness enhancement compared to alloys with the lower volume change, denoted LV, thus indicating that a larger volume change is clearly beneficial for fracture toughness enhancement. This is because the positive dilatational strain accompanying the transformation decreases the local triaxiality.

In comparing the the three curves for uniaxial strain, fracture strain, and fracture toughness in Figure 2.9 and Figure 2.10, it is interesting to note their similarities when plotted against the normalized temperature θ. The maximum uniaxial strain enhancement, maximum fracture-strain enhancement, and maximum fracture-toughness enhancement are observed to exist slightly above $\theta = 0$, or the respective M_s^σ temperatures, indicating that the fine strain-induced martensite is desirable for the improvement of these properties and that the strain-induced martensite formed at the lowest possible temperature before the stress-assisted transformation starts is the most beneficial. Another interesting feature is the apparent drop in uniaxial strain and fracture toughness just below the M_d temperature. This phenomenon is related to the transformation softening accompanying the initial transformation which, just as seen in the σ-ε curves earlier, destabilizes the flow. This

37
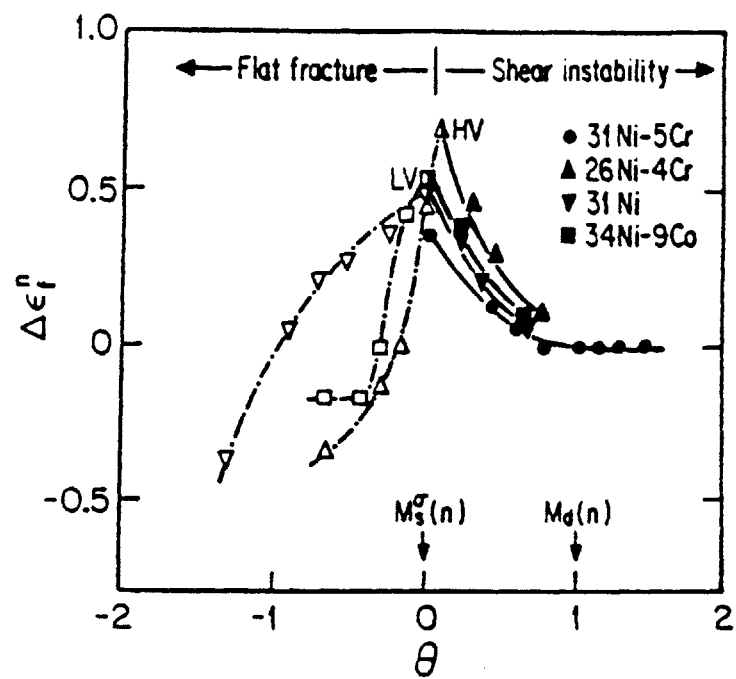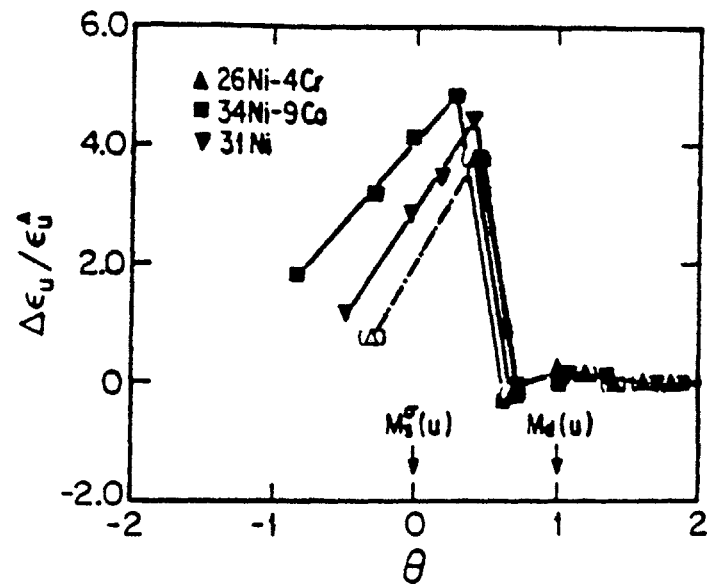
Figure 2.9 a) Relative enhancement in uniform elongation, and b) strain-to fracture vs. normalized temperature for γ'-strengthened TRIP steels [1].
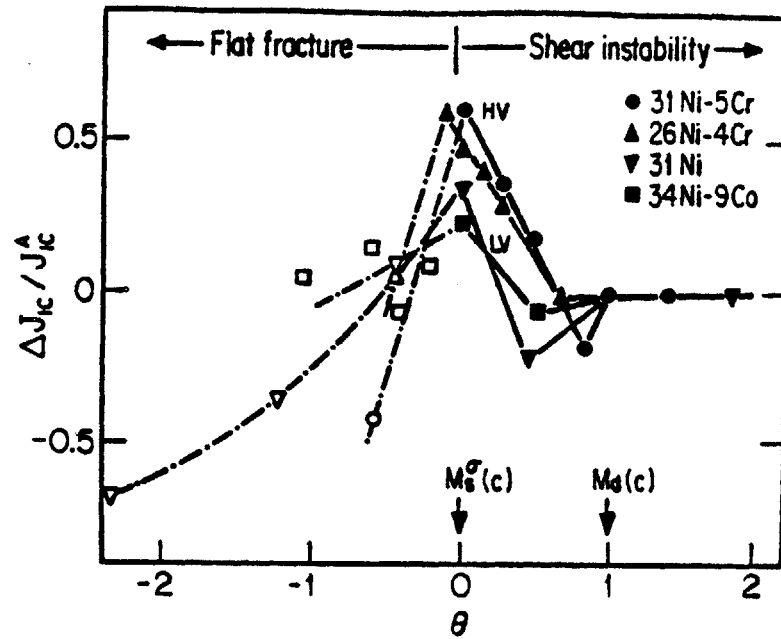
Figure 2.10 Relative enhancement of J-integral toughness vs. normalized temperature for γ'-strengthened TRIP steels [1].

feature is probably also present in the fracture strain curve but it is too small and too close to the M_d temperature to be detected.

2.3 ELASTIC-PLASTIC FRACTURE MECHANICS

Linear-elastic fracture mechanics (LEFM) can only be used as long as the plastic zone is small compared to the crack size. This is usually the case in brittle solids, i.e. ,high-strength, low-toughness materials, where fracture takes place below the yield stress and under plane-strain conditions. The fracture can then be characterized by the plane-strain fracture toughness value, K_{IC}, or the critical energy release rate for crack advance, G_{IC}. The relationship between K and G is

$$G = \frac{K^2}{E} \qquad \text{Plane Stress} \qquad (2.19a)$$

$$G = \left(1 - v^2\right)\frac{K^2}{E} \qquad \text{Plane Strain} \qquad (2.19b)$$

where E is the modulus of elasticity and v is Poisson's ratio. If the plastic zone is large compared to the crack size, i.e. in low-strength, high-toughness materials, LEFM becomes invalid and the J-integral concept [26] has to be introduced.

We define the strain-energy density, W, by:

$$W = W(x,y) = W\!\left(\overline{\varepsilon}\right) = \int_0^\varepsilon \sigma_{ij}\, d\varepsilon_{ij} \qquad (2.20)$$

where $\overline{\varepsilon} = [\varepsilon_{ij}]$ is the infinitesimal strain tensor. Now consider the integral J defined by:

40

$$J = \int_{\Gamma} \left(W\,dy - T \cdot \frac{\partial u}{\partial x}\,ds \right) \qquad (2.21)$$

where Γ represents a closed contour followed counter-clockwise from the lower flat-crack surface and continued along the path Γ to the upper flat-crack surface. T is the traction vector perpendicular to Γ in the outward normal direction along Γ, $T_i = \sigma_{ij} n_j$, u is the displacement vector, and ds is an element of arc length along Γ as illustrated in Figure 2.11. Rice also showed that the J-integral is a path-independent integral when the contour, Γ, is taken around the crack tip, and that the change in potential energy, dU, for a crack extension, da, is:

$$J = -\frac{\partial U}{\partial a}. \qquad (2.22)$$

In LEFM

$$G = -\frac{\partial U}{\partial a} \qquad (2.23)$$

and hence in the limiting case of LEFM, or small-scale yielding (s.s.y.), J=G. This is also equivalent to choosing the contour, Γ, within the K-field or s.s.y. region.

By assuming a power-law relationship between stress and strain in nonlinear elastic materials and combining this with the J-integral concept, Hutchinson [27] and Rice and Rosengren [28] were able to derive unique stress-strain fields:

$$\sigma_{ij} = \sigma_0 \left(\frac{J}{\alpha \sigma_0 \varepsilon_0 I_n r} \right)^{1/n+1} f_{ij}(\theta) \qquad (2.24a)$$

41
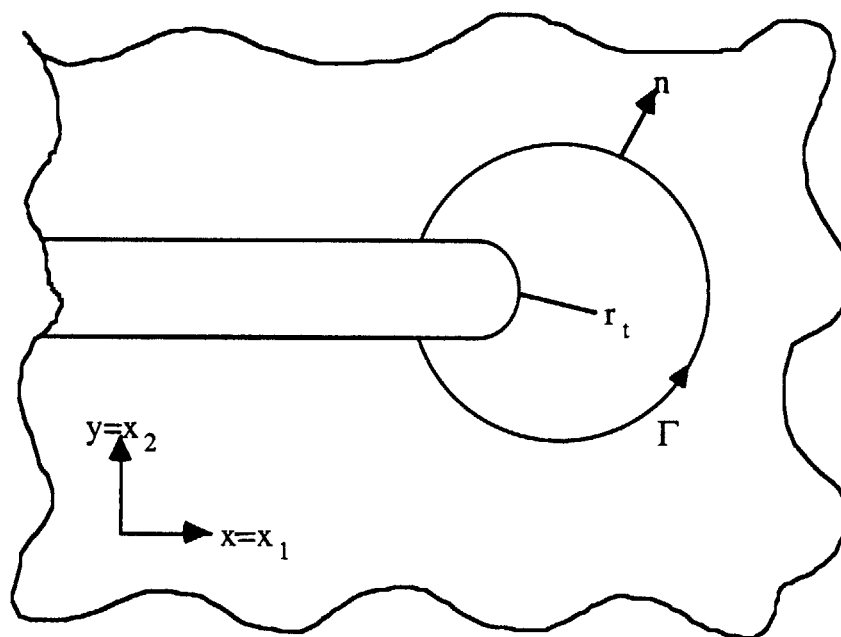
Figure 2.11 Definition of parameters for the J-integral.

$$\sigma_{ij} = \alpha \sigma_0 \left(\frac{J}{\alpha \sigma_0 \varepsilon_0 I_n r} \right)^{n/n+1} g_{ij}(\theta) \tag{2.24b}$$

where n is the strain-hardening exponent, σ_0 and ε_0 are the initial yield stress and strain, α is the constant in the stress-strain law, I_n is a numerical constant depending upon the stress-strain relation, r is the radial distance from the crack tip, and $f_{ij}(\theta)$ and $g_{ij}(\theta)$ are functions measured around the crack tip. The stress-strain fields exhibited only a dependence on the material flow properties. This demonstrated that the J-integral is a stress-field parameter in elastic-plastic fracture mechanics similar to the K parameter in LEFM, and J can therefore be used as a fracture-toughness parameter.

Having adopted the J-integral as a failure criterion for elastic-plastic materials, Rice et al. [29] arrived at the following expression for J valid for a stationary crack in a deeply notched three-point bend specimen:

$$J = \frac{2A}{Bb} \tag{2.25}$$

where A is the area under the load-displacement curve, B is the thickness of the specimen, and b is the remaining uncracked ligament.

To ensure plane-strain conditions, Hutchinson [30] has recommended that for three-point bend specimens:

$$B, b \geq 25 \frac{J}{\sigma_0} \tag{2.26}$$

where σ_0 is the yield stress. This is a more stringent condition than the ASTM 813 specifications [31] which recommend a factor of 15.

2.4 STAINLESS STEELS

Stainless steels can be divided into four major groups [32]:

1)   Austenitic Stainless Steels
2)   Ferritic Stainless Steels
3)   Martensitic Stainless Steels
4)   Precipitation-Hardening Stainless Steels

The selection of a specific stainless steel for a specific application is based upon a multitude of variables such as corrosion resistance, combination of strength and ductility, toughness, magnetic properties, etc. In this thesis a new stainless γ'-precipitation hardened steel has been designed for present purposes, and therefore only precipitation-hardened stainless steels will be discussed here.

The most important properties of precipitation-hardened stainless steels are ease of fabrication, high strength, relatively good ductility, and excellent corrosion resistance [33]. Precipitation-hardened stainless steels can be divided into three general classes: martensitic alloys, semi-austenitic alloys, and austenitic alloys [33,34,35]. Table 2.3 gives the chemical composition of some common precipitation-hardened stainless steels [33]. The first four alloys in Table 2.3 are martensitic alloys, the next three alloys are semi-austenitic alloys, and A286 is an austenitic alloy. Copper is the principal hardener in the first three alloys, the next four use aluminum for precipitation forming, while A286 relies mainly on titanium.

2.4.1 MARTENSITIC ALLOYS

Martensitic precipitation-hardened stainless steels are characterized by relatively low carbon, low nickel, and stabilizing additions which further lower carbon in solution. Hence, the austenite has low stability and transforms to low-carbon martensite on cooling

ALLOY	Cr	Ni	Mo	Ti	Mn	Si	Cb	V	B	N	C	Al	Cu
PH 17-4	16.0	4.2			0.3	0.6	0.25				0.04		3.4
Custom 450	15.0	6.0	0.8		0.25	0.25	0.3				0.03		1.5
Custom 455	11.75	8.4		1.2	0.25	0.25	0.3				0.03		2.5
PH 13-8Mo	12.7	8.2	2.2		0.03	0.03					0.04	1.1	
PH 17-7	17.0	7.1			0.5	0.3				0.04	0.07	1.2	
PH 15-7Mo	15.2	7.1	2.2		0.5	0.3				0.04	0.07	1.2	
PH 14-8Mo	15.1	8.2	2.2		0.02	0.02				0.005	0.04	1.2	
A286	15.0	26.0	1.25	2.0	1.3	0.5		0.3	0.015		0.04	0.2	

Table 2.3 Composition in weight percent of some precipitation-hardenable stainless steels [33].

to room temperature [34]. Martensitic alloys are typically solution treated at approximately 1040°C to dissolve the hardening elements, and are then cooled to room temperature to produce a martensitic structure. Thereafter a single tempering treatment in the temperature range of 480°C-620°C is introduced to precipitate a secondary phase for strengthening of the alloy [35].

Rack and Kalish [36] investigated PH 17-4 and found highly dispersed coherent copper-rich spherical clusters that have the same BCC crystal structure as the matrix at peak hardening. Overaging causes loss of coherency and transformation into FCC ε-precipitates.

2.4.2 SEMI-AUSTENITIC ALLOYS

The semi-austenitic precipitation-hardened stainless steels are alloyed to have low austenite stability which can be further modified by solution treatment and conditioning. The higher the solution temperature, the lower the M_s-temperature, because more elements are in solution [34]. Semi-austenitic alloys are also solution treated at approximately 1040°C but are thereafter water quenched to retain the hardening agent in solution. The structure after the water quench is austenitic. A conditioning step at 760°C precipitates out chromium carbide, $Cr_{23}C_6$, which makes the austenite unstable. The removal of carbon and chromium from the austenite raises the M_s-temperature, and upon subsequent cooling to below 15°C the austenite transforms to martensite. A tempering in the temperature range of 480°C-620°C then precipitates the secondary phase to strengthen the alloy [35].

Using an IAP atom-probe, Paetke and Waugh [37] investigated the precipitation behavior in PH 17-7. They reported a uniform dispersion of NiAl precipitates 1-3 nm in diameter at peak hardening. Overaging caused a slight growth of the NiAl precipitates to 2-4 nm but also produced additional new, square NiAl precipitates, approximately 5-10 nm

across, on the cell boundaries. Also at longer aging times, chromium-rich precipitates were found. Spherical Cr_2C precipitates 10-20 nm in diameter were observed at cell boundaries, and irregular-shaped carbides, 50-100 nm, of possible $M_{23}C_6$ type were also seen. In addition, chromium-rich precipitates containing no carbon and little nickel, aluminum, or iron were found in some areas. These precipitates occurred either as spheres, 5 nm in diameter, interspersed with the NiAl precipitates or as thin plates on the cell boundaries; They were tentatively identified to be a BCC chromium-rich phase associated with 475°C embrittlement.

2.4.3 AUSTENITIC ALLOYS

The austenitic precipitation-hardened stainless steels are heavily alloyed to further stabilize the austenite [34]. Solution treatment is typically in the temperature range of 900°C-1150°C, followed by rapid cooling to room temperature to suppress the precipitation of a second phase. Subsequent aging in the temperature range of 650°C-760°C produces strengthening [35].

The precipitation behavior of A286 has been studied by a variety of investigators [38,39]. A286 is strengthened by the ordered FCC γ'-precipitate, $Ni_3(Ti,Al)$, but variations in the minor alloying additives can significantly influence the precipitation sequence. It is important to note that titanium is the major γ'-forming element in iron-nickel-base alloys while aluminum-rich γ' is predominant in most nickel-base superalloys. Molybdenum, a solid-solution strengthener, expands the austenitic iron-nickel matrix and also enters carbides and γ'. It can therefore alter the austenite-γ' misfit. It has also been reported that molybdenum suppresses cellular η-formation* and therefore improves the notch ductility. γ' is coherent with the austenitic matrix but coherency strains are not a major strengthening factor. The lattice misfit is typically less than approximately 0.5

---

* Hexagonal close-packed Ni_3Ti

percent. The major strengthening contribution comes from paired dislocations, cutting precipitate particles, alternately creating and annihilating antiphase boundaries in the γ'. In the overaged condition, dislocations will bypass the γ'-particles by looping around, which gives lower strength. Maximum strengthening occurs in iron-nickel alloys at a γ'-diameter of approximately 100-500 Å, and the optimum volume fraction of γ' is 0.2-0.3.

2.4.4 MECHANICAL PROPERTIES

Fracture-toughness data are not available for many standard types of stainless steels. Most testing has been concentrated on the high-strength precipitation-hardening stainless steels because these materials have been used in critical applications where fracture-toughness testing has been found most useful for evaluating materials. Steel manufacturers normally report Charpy impact data as their toughness criterion because of its simple procedure and low cost. Figure 2.12 summarizes K_{IC} fracture-toughness data versus yield strength for some common precipitation-hardening stainless steels available today [32,40,41,42]. The highest yield strengths shown correspond to optimum peak hardness values. A gradual increase in fracture toughness takes place in the overaged condition for each case with an accompanying decrease in strength.
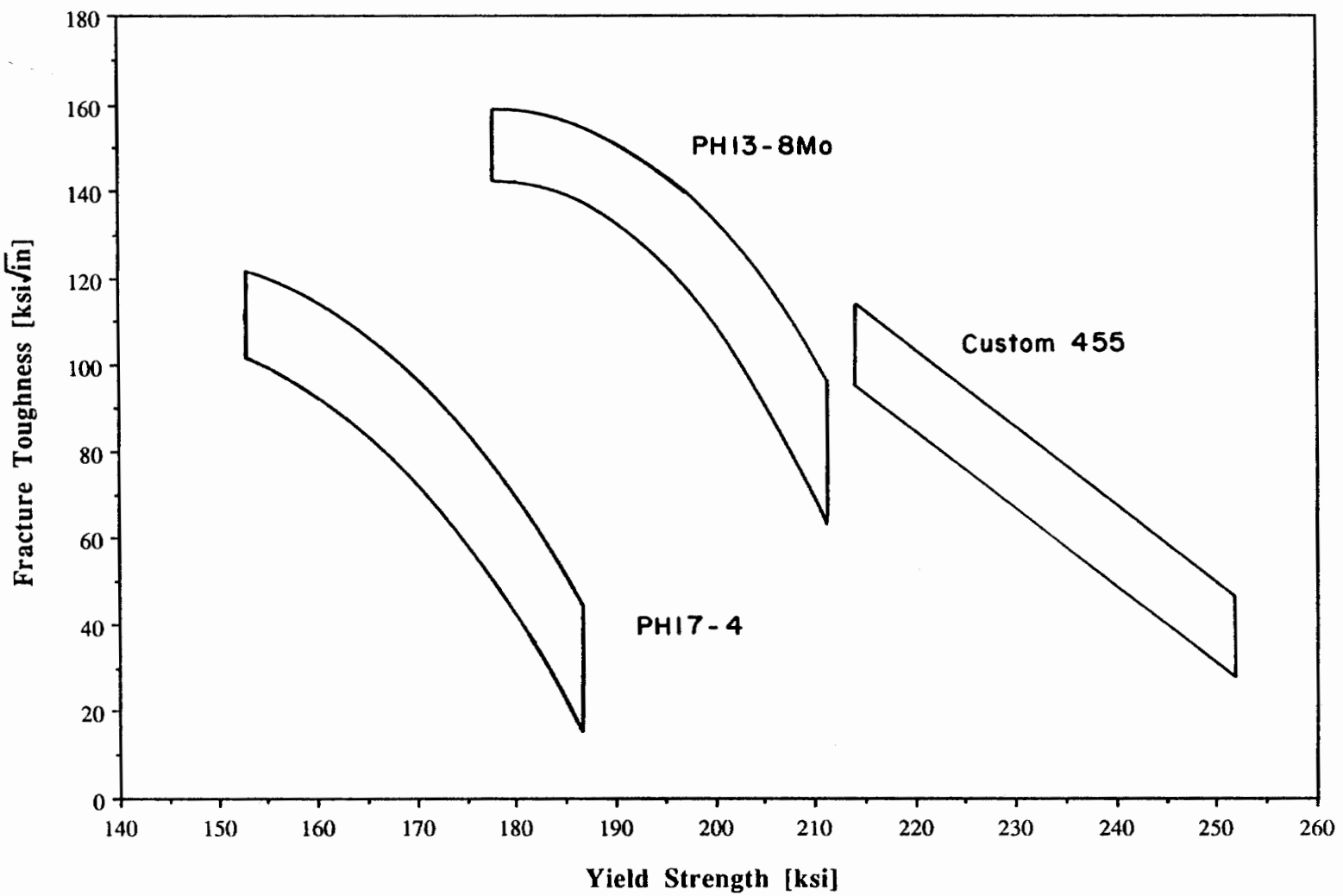
Figure 2.12 Fracture toughness versus yield strength for some commercial precipitation-hardened stainless steels.

49

CHAPTER 3

EXPERIMENTAL PROCEDURES

3.1 MATERIALS DESIGN

To accomplish the research objectives, as stated in Chapter 1, a set of new alloys was designed. Thermodynamic calculations were performed to develop metastable austenitic steels, with steel A286 as the starting point. A286 is a γ'-strengthened steel and a yield strength of approximately 1300 MPa (190 ksi) can be expected after warm working. γ'-particles, $Ni_3(Ti,Al)$, are expected to be in the range of 50-100 Å [43].

To decrease the temperature sensitivity around M_s^σ, chromium can be added as previously described in chapter 2 [12]. This lowers both the stacking-fault energy and the FCC-BCC entropy difference; both factors decrease the temperature sensitivity, as schematically depicted in Figure 3.1. Thus, optimum mechanical properties can be obtained over a wider temperature range. On the other hand, the addition of chromium makes the alloy more stable because the driving force for martensitic transformation decreases. To maintain the same stability, nickel has to be reduced. The amount of nickel which has to be reduced when chromium is added can be calculated from thermodynamics. Assuming that the critical driving force for transformation will be the same when chromium is added, and considering only iron, nickel, and chromium as compositional variables, the
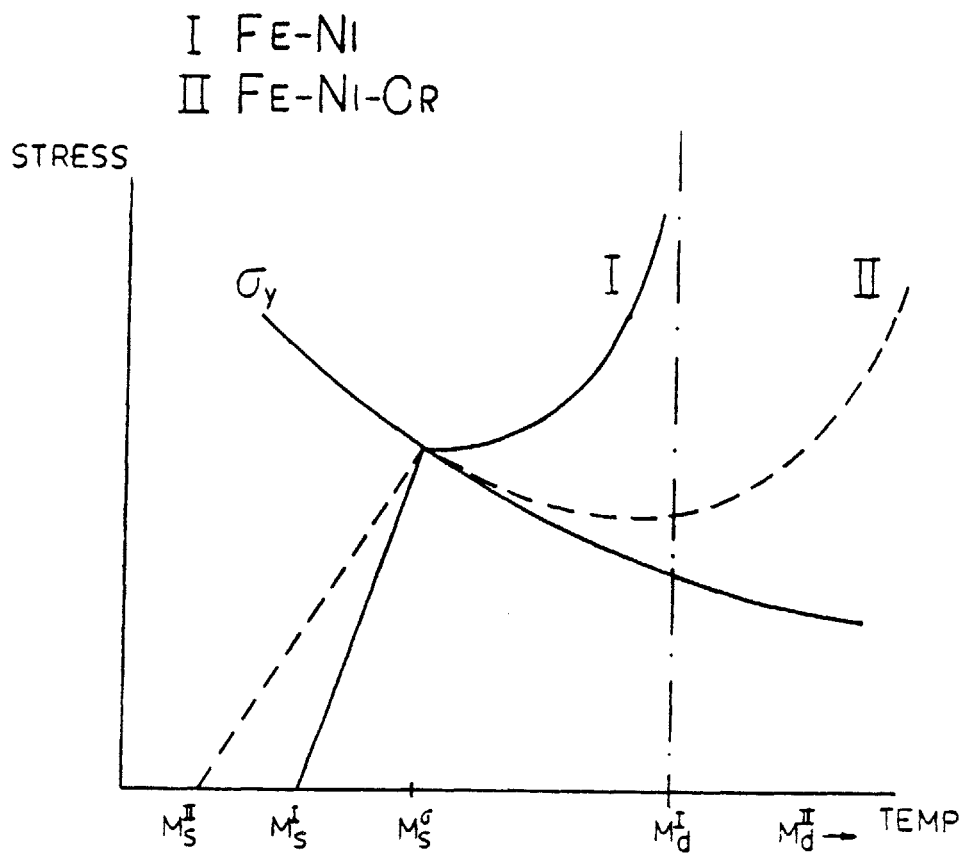
Figure 3.1 Schematic representation of the temperature sensitivity change due to chromium addition.

driving force for the martensitic transformation can be calculated using a regular solution model:

$$\Delta G^{\gamma \rightarrow \alpha} = x_{Fe} \Delta G_{Fe}^{\gamma \rightarrow \alpha} + x_{Cr} \Delta G_{Cr}^{\gamma \rightarrow \alpha} + x_{Ni} \Delta G_{Ni}^{\gamma \rightarrow \alpha} + x_{Fe} x_{Cr} \Delta \Omega_{FeCr}^{\gamma \rightarrow \alpha} + x_{Fe} x_{Ni} \Delta \Omega_{FeNi}^{\gamma \rightarrow \alpha} \quad (3.1)$$

where $\Delta G^{\gamma \rightarrow \alpha}$ is the free-energy change for the transformation; $\Delta G_{Fe}^{\gamma \rightarrow \alpha}$, $\Delta G_{Cr}^{\gamma \rightarrow \alpha}$, and $\Delta G_{Ni}^{\gamma \rightarrow \alpha}$ are the free-energy change contributions of iron, chromium, and nickel for the transformation; x is the mole fraction; and $\Delta \Omega_{FeCr}^{\gamma \rightarrow \alpha}$ and $\Delta \Omega_{FeNi}^{\gamma \rightarrow \alpha}$ are the interaction coefficients between iron-chromium and iron-nickel respectively. At room temperature, $\Delta G_{Fe}^{\gamma \rightarrow \alpha}$=-1085 cal/mole, $\Delta G_{Cr}^{\gamma \rightarrow \alpha}$=-2545 cal/mole, $\Delta G_{Ni}^{\gamma \rightarrow \alpha}$=1990 cal/mole, $\Delta \Omega_{FeCr}^{\gamma \rightarrow \alpha}$=4350 cal/mole, and $\Delta \Omega_{FeNi}^{\gamma \rightarrow \alpha}$=650 cal/mole. These data were obtained from the Kaufman database [44].

The entropy change accompanying the martensitic transformation is similarly:

$$\Delta S^{\gamma \rightarrow \alpha} = x_{Fe} \Delta S_{Fe}^{\gamma \rightarrow \alpha} + x_{Cr} \Delta S_{Cr}^{\gamma \rightarrow \alpha} + x_{Ni} \Delta S_{Ni}^{\gamma \rightarrow \alpha} + x_{Fe} x_{Cr} \left[\frac{\partial \Omega}{\partial T} \right]_{FeCr}^{\gamma \rightarrow \alpha} + x_{Fe} x_{Ni} \left[\frac{\partial \Omega}{\partial T} \right]_{FeNi}^{\gamma \rightarrow \alpha} \quad (3.2)$$

At room temperature, $\Delta S_{Fe}^{\gamma \rightarrow \alpha}$=-1.67 cal/mole/K, $\Delta S_{Cr}^{\gamma \rightarrow \alpha}$=0.15 cal/mole/K, $\Delta S_{Ni}^{\gamma \rightarrow \alpha}$=-0.80 cal/mole/K, $\left[\frac{\partial \Omega}{\partial T} \right]_{FeCr}^{\gamma \rightarrow \alpha}$=-1.6 cal/mole/K, and $\left[\frac{\partial \Omega}{\partial T} \right]_{FeNi}^{\gamma \rightarrow \alpha}$=-2.0 cal/mole/K.

Calculations were performed with the above formulas for different nickel-chromium ratios. In order to adjust for any uncertainties in the calculations and to assure that M_s^σ(crack tip) will be obtained at room temperature, two series of alloys, each with different nickel contents were designed. One series represents a refinement of the 4% chromium alloy studied by Leal [1], and the second series is based on a new 12% chromium stainless alloy. The alloys were kindly provided by Carpenter Technology Corporation, and the chemical compositions are listed in Table 3.1. The alloy symbols used throughout this thesis are as follows: 424, 425, and 428 for the 4% chromium alloys,

ALLOY	Cr	Ni	Mo	Ti	V	Al	C	N	Mn	Mg	Si	B	S	P	Fe
424	4.03	24.00	1.25	3.02	.30	.21	.002	.001	.088	.0007	.005	.0067	.003	<.005	Balance
425	3.93	25.04	1.25	2.97	.32	.16	.005	.001	.09	.001	<.01	.0093	.002	<.005	Balance
428	4.03	27.81	1.25	3.03	.29	.16	.002	.001	.08	.001	<.01	.0095	.002	<.005	Balance
1217	11.82	17.08	1.31	3.01	.34	.21	.004	.001	.10	.001	<.01	.0084	.003	<.005	Balance
1219	12.16	19.10	1.29	3.03	.33	.20	.003	.001	.10	<.001	<.01	.0095	.002	<.005	Balance
1221	11.90	20.64	1.27	2.97	.32	.19	.003	.001	.08	<.001	<.01	.0093	.003	<.005	Balance
1223	11.93	22.65	1.28	3.01	.32	.20	.001	.001	.08	.001	<.01	.0097	.003	<.005	Balance

Table 3.1 Composition in weight percent of alloys investigated.

where 24, 25, and 28 designate the nickel contents, and similarly 1217, 1219, 1221, and 1223 for the 12% chromium series.

The stability of the new 12% chromium series is intended to be the same as for the 4% chromium alloys. This is depicted in the Schaeffler diagram of Figure 3.2. The two alloy series have the same relation to the martensite line, corresponding to the same predicted metastability.

3.2   MATERIALS PROCESSING

All seven alloys were VIM produced at Carpenter Technology Corporation into 100 pound, 4.5-inch square ingots. The ingots were subsequently homogenized at 2175°F (1190°C) for 24 hours, cooled to 2100°F (1149°C), and forged into 3-inch square bars. After reheating to 1900°F (1038°C),further forging was delayed until the surface temperature dropped to approximately 1700°F (927°C) before the alloys were reduced to their final size of 2.875 x 1.5 inch billets. This processing resulted in a heavily hot-cold worked structure since most of the final forging took place in the temperature region of approximately 1500°F (816°C).

To determine the optimum solution-treatment temperature, all seven alloys were subjected to grain-growth experiments in the temperature range of 950°C to 1050°C for one hour. The results of these initial experiments are plotted in Figure 3.3. Excessive grain growth occurred in all seven alloys at temperatures above 950°C, so it was decided to adopt 950°C as the solution temperature. Since 950°C was the lower limit of this experimental range, 900°C and 925°C were also checked for one alloy in both the 4% and 12% chromium series to assure that 950°C was the optimum solution temperature. Both 900°C and 925°C treatments showed a heavily duplex grain size with times of one and two hours, indicating too low a temperature for full recrystallization. From the standpoint of

54

$$\text{Ni eq} = (\text{Ni}) + (\text{Co}) + 0.5\,(\text{Mn}) + 0.3\,(\text{Cu}) + 25\,(\text{N}) + 30\,(\text{C})$$

$$\text{Cr eq} = (\text{Cr}) + 2\,(\text{Si}) + 1.5\,(\text{Mo}) + 5\,(\text{V}) + 5.5\,(\text{Al}) + 1.75\,(\text{Nb}) + 1.5\,(\text{Ti}) + 0.75\,(\text{W})$$
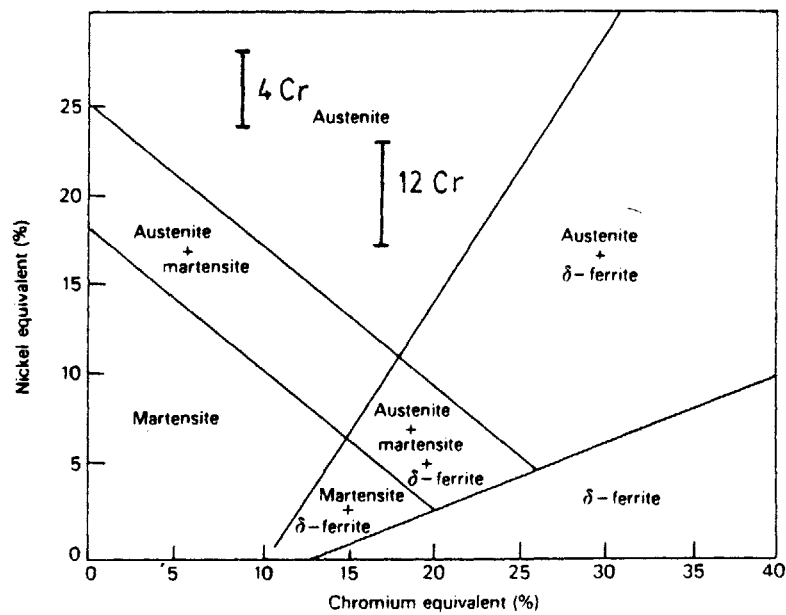
Figure 3.2   4% chromium and 12% chromium series in relation to martensite formation.
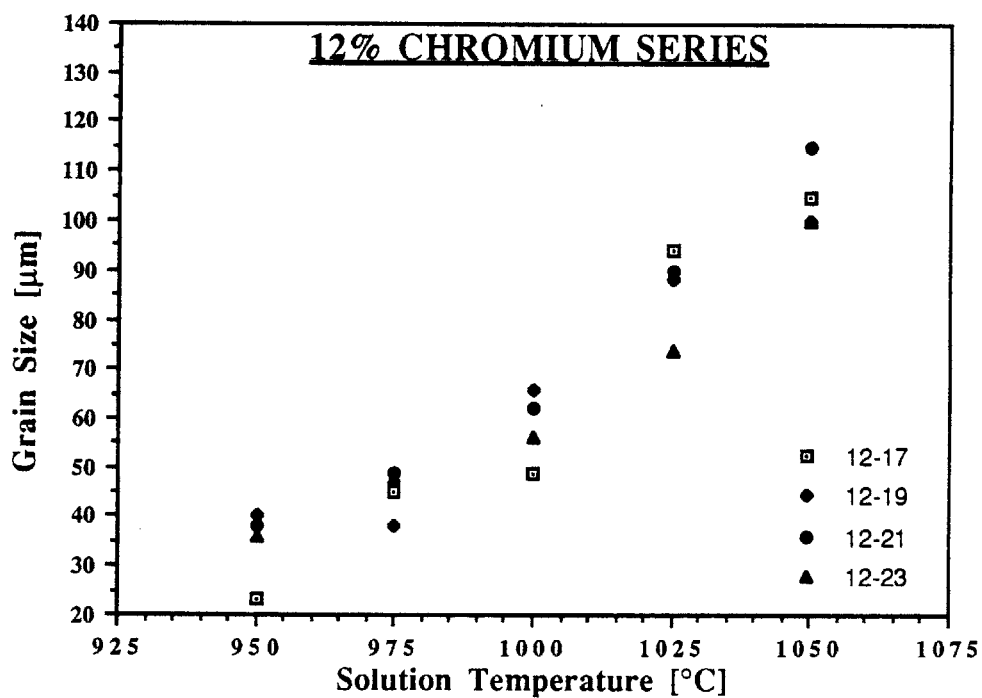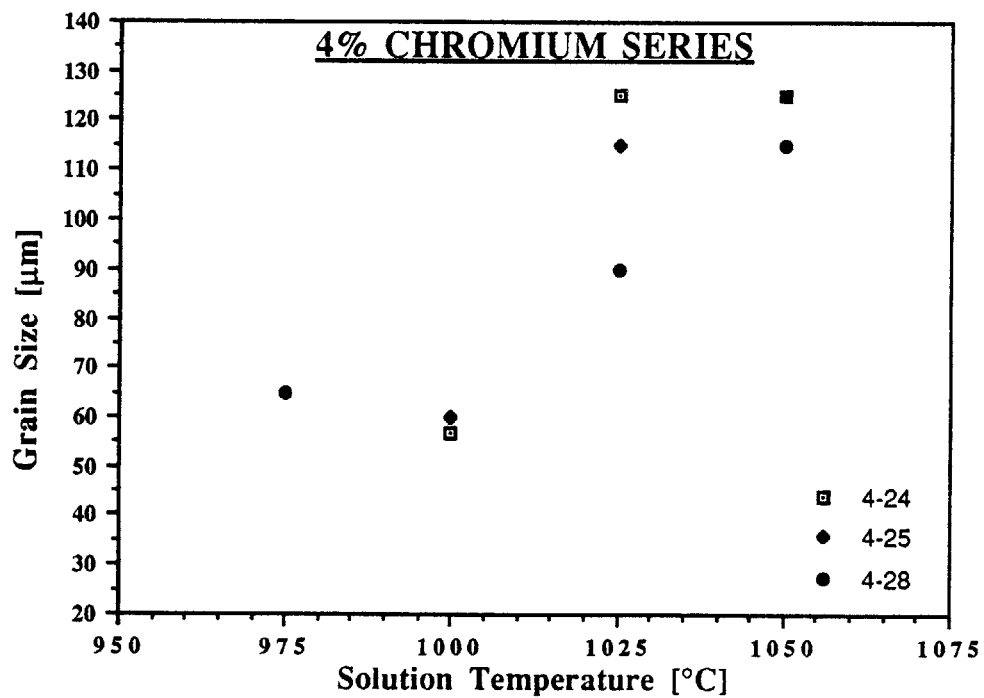
Figure 3.3 Grain size as a function of solution treatment temperature before warm working.

reproducible mechanical properties , this was unacceptable, so 950°C was chosen as the solution temperature.

Simultaneously with the grain-size experiments, the aging behavior of alloys 1219 and 425 at 700°C was examined as a function of solution temperature. These results are plotted in Figure 3.4. These preliminary findings indicated a maximum achievable hardness of approximately 36 Rockwell C for alloy 1219 and 38 Rockwell C for 425. This hardness level was found to be independent of solution temperature at 950°C, 975°C, and 1000°C, while the 1050°C solution temperature always resulted in a final hardness of one to two Rockwell C points lower for both alloys 1219 and 425. The initial response of the aging curves for both 1219 and 425 demonstrated that a lower solution temperature gives a higher hardness for the same aging time. This higher hardness can be attributed to the final grain size achieved at the different solution temperatures. Smaller grain size gives, as one would expect, a higher hardness.

The time to maximum hardness at an aging temperature of 700°C is approximately 60 hours for alloy 425 and more than 100 hours for 1219, indicating that the chromium addition slows down the precipitation behavior. This was found to be disadvantageous in that such long holding times would be very costly in commercial treatments. Accordingly, a higher temperature of 750°C was chosen to accelerate the precipitation process. This reduced the time for maximum hardness to approximately 10 hours for both alloys 1219 and 425, but it also decreased the maximum hardness to 32 Rockwell C for 1219 and 34 Rockwell C for 425.

The strength levels after aging at both 700°C and 750°C were below the research objective (45 Rockwell C), and so multiple treatments were performed. Multiple heat treatments of superalloys have been reported to increase the strength due to precipitation of secondary smaller γ'-particles at a lower aging temperature [39,45]. The results of these
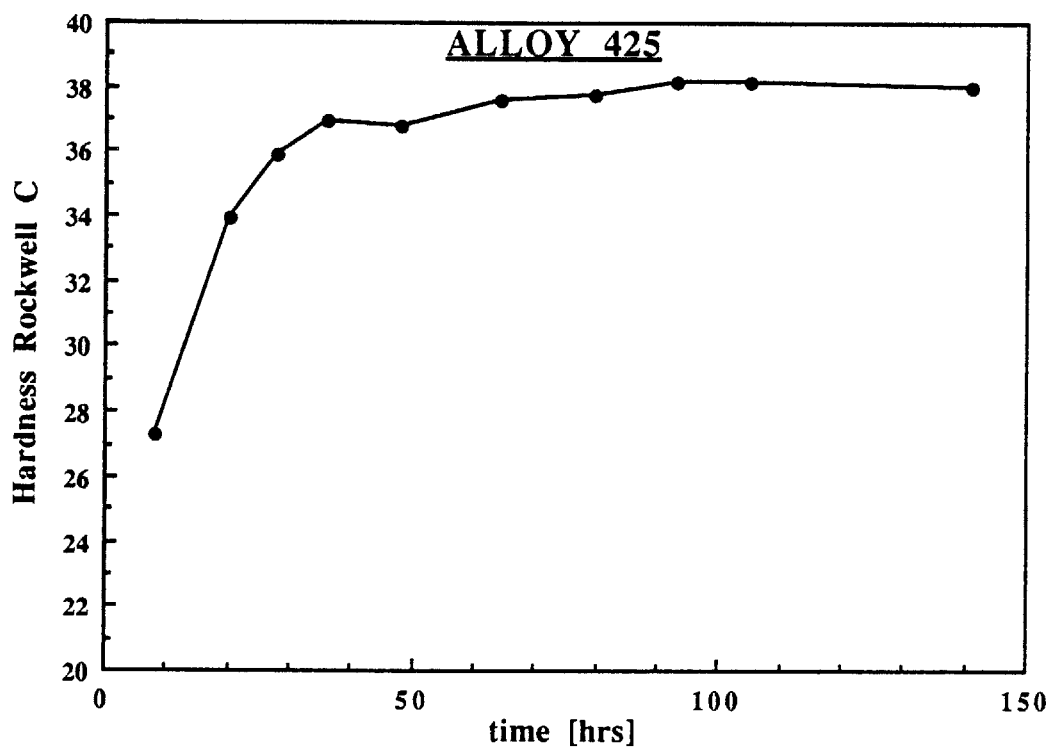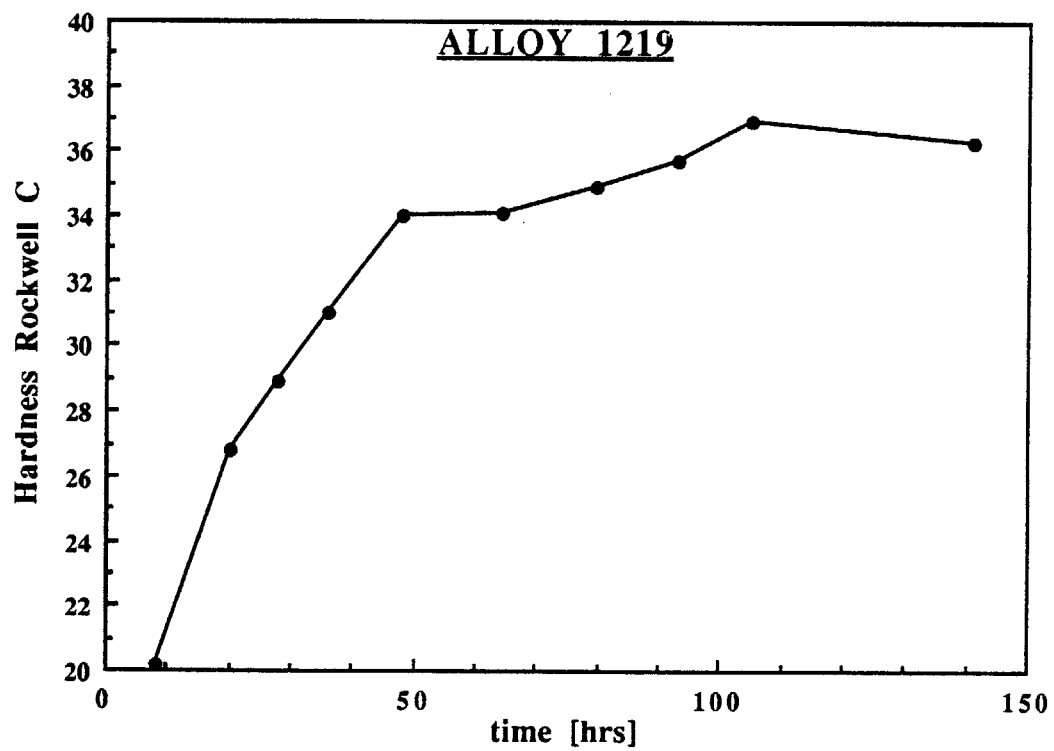
Figure 3.4 Aging curves at 700°C after solution treatment at 950°C for 1 hr.

multiple heat treatments are given in Table 3.2. It shows that a higher initial aging temperature yields higher hardness. However, even though these multiple aging treatments did raise the obtainable hardness of both 1219 and 425, the hardness levels were still below the research objectives.

In order to raise the strength values to the level stated in the research objectives, >1300 MPa (190 ksi), the seven alloys were warm worked at 450°C to a 40% area reduction following a solution treatment of 950°C for one hour. This corresponds to the warm working conditions utilized by Leal [1] on similar metastable austenitic steels. The working operation was conducted by the U.S. Army Materials Technology Laboratory in Watertown, MA.

The warm working operation raised the strength level and enhanced the kinetics of the γ' precipitation. A typical aging curve is illustrated in Figure 3.5, indicating a final hardness of 46 Rockwell C. To favor uniformity in the microstructure, a time of eight hours at 700°C was chosen for the aging treatment.

The selected solution temperature of 950°C for one hour, followed by a warm working operation of 40% area reduction and subsequent aging treatment at 700°C for eight hours resulted in a final grain size of 40-50 μm for all seven alloys as shown in Table 3.3, with only a minor difference between the 4% and 12% chromium series.

3.3 MICROSTRUCTURAL CHARACTERIZATION

3.3.1 METALLOGRAPHY

Optical microscopy was used to measure the austenite grain size. The specimen was mounted in bakelite and then ground on 180, 240, 320, 400, and 600 grit silicon carbide paper, polished with 6 μm diamond paste on a felt cloth, and finally polished with

ALLOY 1219 SOLUTION TEMPERATURE	AGING TEMPERATURE			
	750°C(5hrs) 700°C(10hrs)	750°C(5hrs) 700°C(10hrs) 650°C(20hrs)	750°C(10hrs) 700°C(20hrs)	700°C(10hrs) 750°C(5hrs)
900°C(2hours)	37.6	39.2	37.1	33.2
950°C(1hour)	36.6	38.2	36.8	29.9
1000°C(1hour)	34.8	36.5	36.0	27.9
1050°C(1hour)	35.3	36.4	35.1	26.5

ALLOY 425 SOLUTION TEMPERATURE	AGING TEMPERATURE			
	750°C(5hrs) 700°C(10hrs)	750°C(5hrs) 700°C(10hrs) 650°C(20hrs)	750°C(10hrs) 700°C(20hrs)	700°C(10hrs) 750°C(5hrs)
900°C(2hours)	38.1	38.9	37.9	34.7
950°C(1hour)	37.5	38.2	37.4	34.3
1000°C(1hour)	37.6	38.3	36.8	33.8
1050°C(1hour)	36.9	37.5	36.6	33.5

Table 3.2   Rockwell C hardness after multiple aging treatments for
a) alloy 1219, and b) alloy 425.

ALLOY 428
Solution treatment at 950°C for 1hr
and 40% area reduction at 450°C

Aging at 700°C

Hardness Rockwell C

time [hrs]
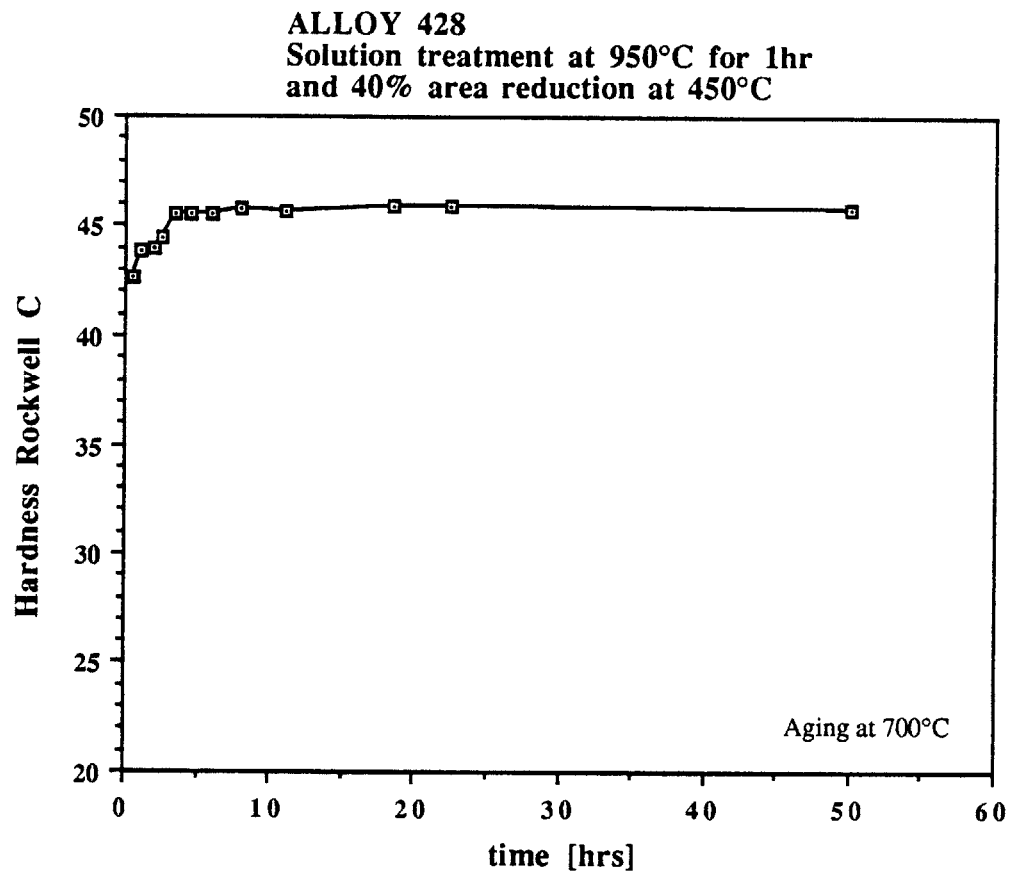
Figure 3.5 Aging curve after warm working for alloy 428.

61

ALLOY	Grain Size (μm)
424	49±2
425	48±3
428	45±2
1217	39±2
1219	41±3
1221	40±3
1223	40±2

Table 3.3   Grain size after solution treatment at 950°C (1hr),
40% RA at 450°C, and aging treatment at 700°C (8hrs).

0.5 µm diamond paste on a fine felt cloth. The polished samples were then swabbed with a cotton ball saturated with aqua regia (30 ml HNO_3 - 50 ml HCl) to reveal the grain size.

Subsequent microscopic observations were conducted using darkfield images in a Nikon optical light microscope. Five micrographs were taken at different locations of each sample at magnifications such that approximately 80-100 intercepts could be counted with a circular line array as specified by ASTM E112-85 [46]. The mean intercept distance, $\bar{l}$, was obtained and the austenite grain size, d, was calculated from [47]:

$$d = 1.68 \, \bar{l} \qquad (3.3)$$

3.3.2. X-RAY DIFFRACTION

The effective atomic-volume change accompanying the martensitic transformation directly affects the fracture-toughness enhancement and is therefore an important parameter to quantify. A fully computerized X-ray Diffractometer with a rotating anode chromium X-ray source operating at 45 kV and 160 mA was used to measure lattice parameters of the austenite and martensite. To filter out the background noise, a diffracted-beam monochrometer was attached, and therefore only austenite and martensite reflections from the CrK_α (λ=2.291 Å) radiation were obtained.

A tensile specimen was cut length-wise on a Struers Accutom-2 cut-off saw, mounted in bakelite, and thereafter ground on 600 grit silicon carbide paper. The X-ray reflections were obtained with an incident beam of approximately 3x1 millimeters and a two-degree vertical slit. Because of plastic deformation in the tensile specimen, X-ray peak broadening was quite apparent. To obtain as sharp an X-ray reflection peak as possible, a small receiving slit of 0.02 inches was employed. The scan rate was one degree per hour.

The lattice parameters were calculated using the Nelson-Riley-Taylor-Sinclair (N-R-T-S) function [48,49] and extrapolating to $\theta=90°$. In accordance with the N-R-T-S recommendations, only the austenite (220) and (200) reflections as well as the martensite (211) and (200) were measured. The effective atomic-volume change was calculated from the lattice parameters thus determined.

3.4 MECHANICAL TESTING

3.4.1 UNIAXIAL TENSION TESTING

Uniaxial tension tests were performed on all seven alloys. The tests were conducted on an INSTRON Model 1125 screwdriven mechanical testing machine at room temperature and at a cross-head rate of 0.005 in/min. The specimen dimensions are given in Figure 3.6. The tensile specimens were cut so that the loading axis was parallel to the rolling direction.

From the load-displacement curve obtained from the INSTRON chart recorder, the true yield strength, σ_y, true uniform elongation, ε_u, true ultimate tensile strength, σ_{UTS}, and true strain to failure, ε_f, were calculated.

After fracture, half the specimen was used for fractographic analysis in the SEM while the other half was used for X-ray analysis and metallographic examination.

3.4.2 J_{IC} FRACTURE TOUGHNESS TESTING

J-integral fracture toughness testing using three-point bend specimens was performed on all seven alloys at room temperature. In addition, alloy 12Cr-23Ni was tested at an elevated temperature (225°C). The three-point bend specimen configuration is

ALL DIMENSIONS IN INCHES
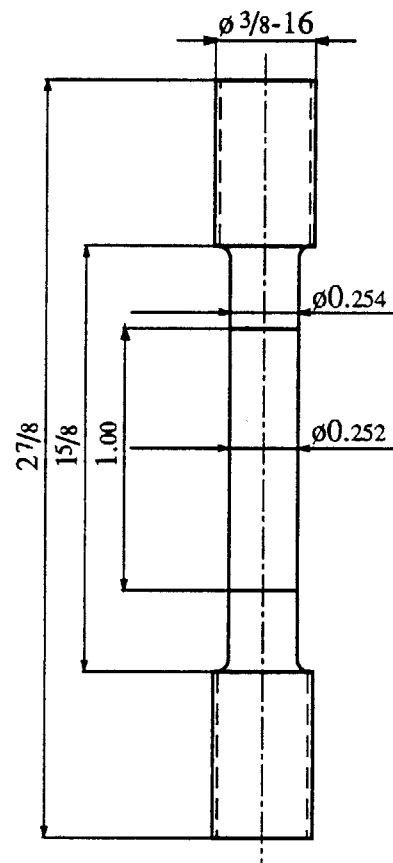
Figure 3.6 Tensile specimen.

shown in Figure 3.7. All fracture toughness specimens were cut in the L-W direction with their length parallel to the rolling direction and the crack propagating in the width direction.

Pre-cracking was conducted according to ASTM Standard E399-83 [50] on an MTS servo-hydraulic loading machine, employing constant ΔK pre-cracking procedures with an S/W value of 4, where S is the span, i.e. the distance between rollers, and W is the specimen width. The starting load was 4000 N, and P_{min} was 10 percent of P_{max} throughout the pre-cracking procedure. The final a/W, where a is the crack length, was approximately 0.55 for all specimens, and the final load was in the range of 2700-3000 N. To calculate the final plane strain plastic zone, r_y, the following expression was used [51]:

$$r_y = \frac{1}{3\pi}\left(\frac{\Delta K}{\sigma_y}\right)^2 \tag{3.4}$$

where ΔK is the stress intensity factor calculated from [52]:

$$\Delta K = \frac{4\Delta P}{BW^{\frac{1}{2}}}\left[2.9\left(\frac{a}{W}\right)^{\frac{1}{2}} - 4.6\left(\frac{a}{W}\right)^{\frac{3}{2}} + 21.8\left(\frac{a}{W}\right)^{\frac{5}{2}} - 37.6\left(\frac{a}{W}\right)^{\frac{7}{2}} + 38.7\left(\frac{a}{W}\right)^{\frac{9}{2}}\right] \tag{3.5}$$

where P is the load, and B is the thickness of the specimen. Thus, one obtains a maximum plastic zone size of 280 μm.

In order to minimize pre-crack interference with the crack extension during the actual fracture toughness test, certain precautions were taken during pre-cracking:

1)   Pre-cracking was carried out at an elevated temperature (250°C) to avoid martensitic transformation.

2)   Pre-cracking was also conducted in vacuum to ensure a flat pre-crack. It was found that pre-cracking in air gave immense crack branching.

ALL DIMENSIONS IN INCHES
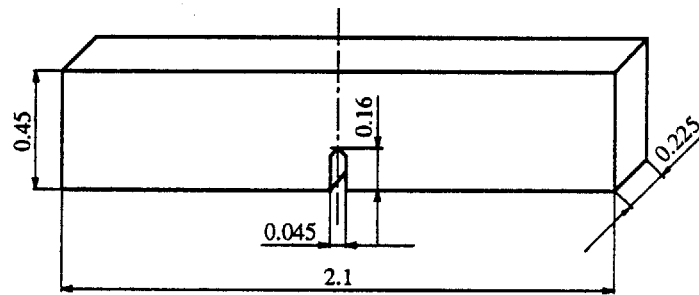
Figure 3.7 Three-point bend fracture-toughness specimen.

The actual fracture toughness tests were conducted on an INSTRON Model 1125 screwdriven machine at a cross-head rate of 0.1 mm/min. The roller diameter used was 10 mm. To measure the crack advance, a single specimen technique was adopted following ASTM Standard E813-81 [31]. During the test, partial unloadings of approximately 10 percent were performed at suitable intervals. Load/displacement data were obtained during the test. The displacement measured was the true load point displacement. The experimental setup is illustrated in Figure 3.8.

3.4.3 DATA ACQUISITION AND CRACK-LENGTH MEASUREMENT

An IBM PC Compatible Computer with an IBM Data Acquisition Board (DACA) was used for data acquisition during the fracture toughness test. The UnkelScope Data Acquisition Program [53] collected load/displacement data pairs at a frequency of 0.5 Hz during the monotonic loading sequence of the test. During the partial unloading sequence, data pairs were collected at a frequency of 8 Hz to ensure high accuracy for the subsequent crack-length calculations.

By determining the compliance during the unloading sequence, the actual crack length, a, can be obtained if the specimen geometry has been analyzed. This analysis is outlined in Appendix A and the following expression for the three-point bend specimen is obtained:

$$\frac{a}{W} = C_0 + C_1 U + C_2 U^2 + C_3 U^3 + C_4 U^4 + C_5 U^5 \qquad (3.6)$$

where $C_0 = 0.9878$, $C_1 = -3.0106$, $C_2 = -15.4301$, $C_3 = 59.9455$, $C_4 = 296.505$, $C_5 = -2171.2354$, and

$$U = \frac{1}{1 + \sqrt{E'C\,B}} \qquad (3.7)$$
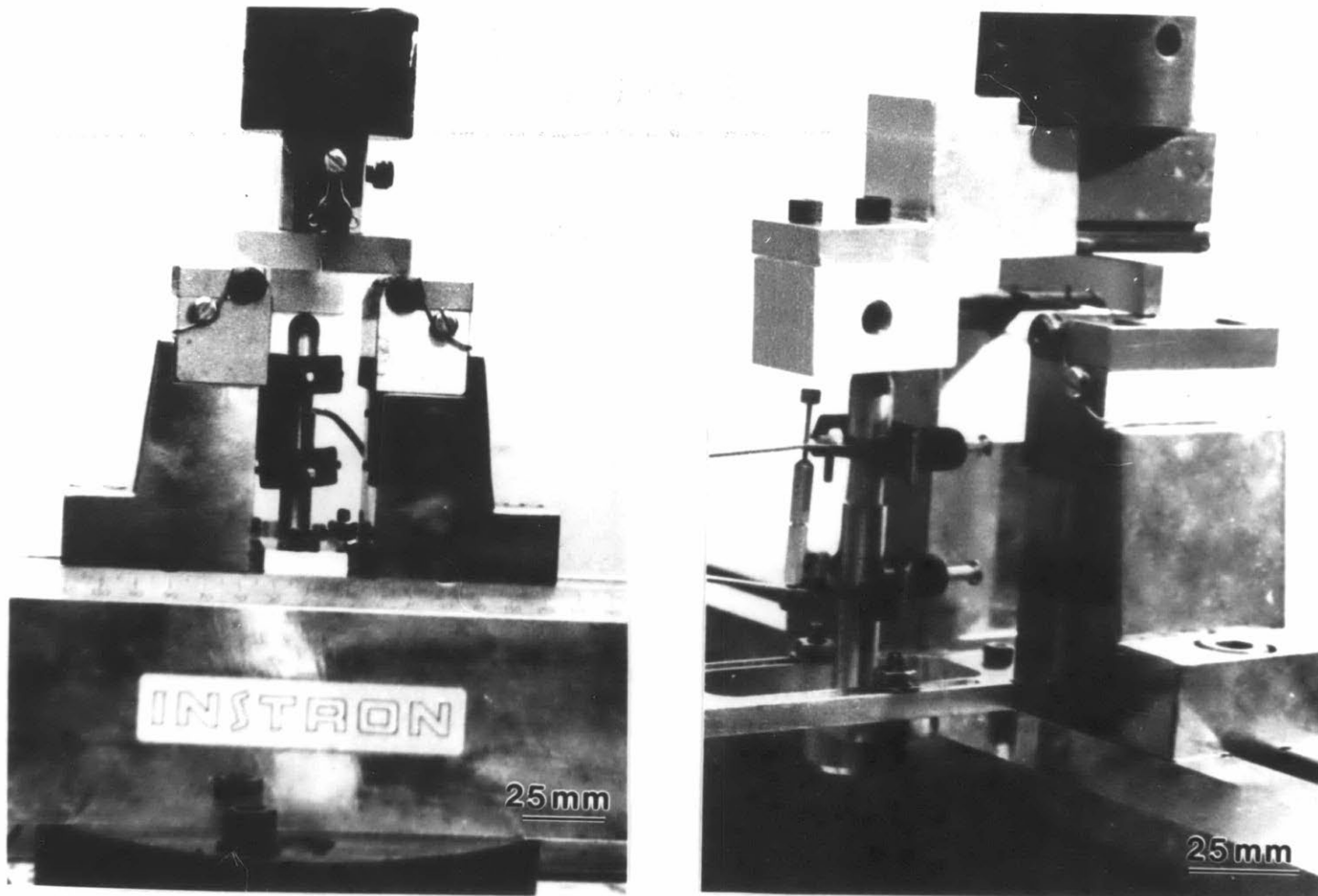
Figure 3.8 Experimental setup for three-point bend fracture-toughness testing.

$E'=E/(1-v^2)$ for plane strain, C is the compliance, and B is the thickness of the specimen. Figure 3.9 illustrates the relationship between a/W and the normalized compliance.

To simplify calculations for the fracture toughness and crack-length values, computer software was developed. By using the previously collected data pairs and performing a series of calculations in the developed computer program, the fracture toughness, J, versus crack extension, Δa, was obtained.

3.5   CRACK-TIP METALLOGRAPHY

Optical microscopy was used to examine the interaction between strain-induced martensite and crack-tip processes. Following a fracture toughness test, the specimen was cut transversely with the Struers Accutom-2 cut-off wheel until only the notch and crack-tip zone remained. The specimen was then cut in half, and one half served for fractographic examination in a scanning electron microscope, while the second half was prepared for crack-tip metallography.

It was found that mounting the specimen in bakelite was not suitable inasmuch as the bakelite did not entirely fill the crack. This caused numerous problems in both the subsequent grinding/polishing operation as well as in the final optical examination. To circumvent this difficulty, a cold mount applied under vacuum was tried. The specimen was kept under vacuum, and Struers Epofix resin, preheated to 70°C to lower its viscosity, was slowly poured onto the specimen. The vacuum had to be carefully controlled since a too low vacuum could induce boiling of the resin. This vacuum impregnation technique assured that the preheated resin fully filled the crack all the way to its tip.

The specimen was then ground on 600 grit silicon carbide paper, polished with 9 μm diamond paste on a felt cloth for 90 seconds, followed by 3 μm diamond paste for 60
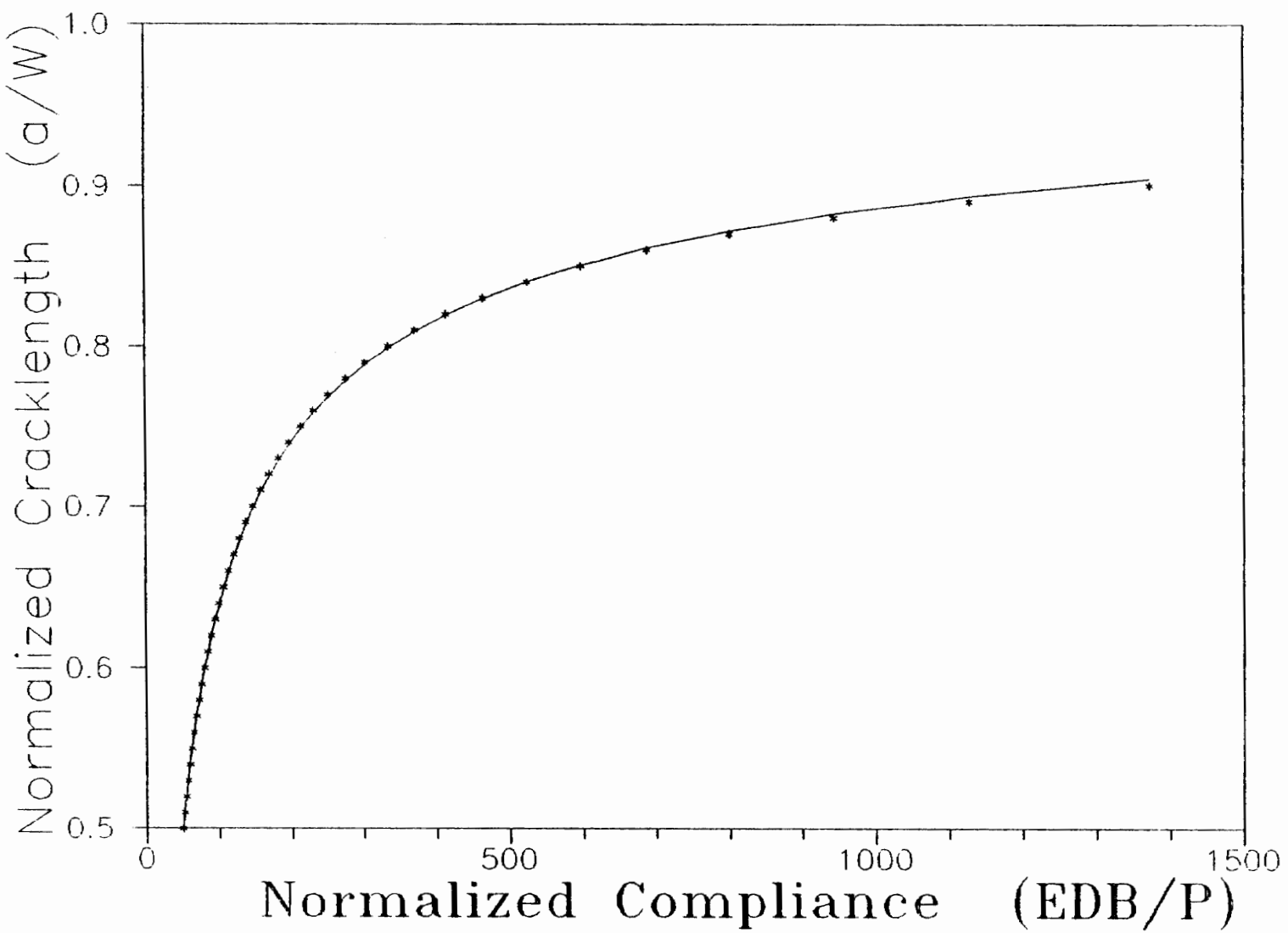
Figure 3.9 Normalized crack length as a function of derived normalized compliance for three-point bend specimen.

seconds, 0.25 μm diamond paste for 45 seconds, and finally with 0.05 μm diamond paste for 30 seconds. The polished samples were immersed in a mixture of 100 ml H_2O - 20 ml HCl - 0.12 g $Na_2S_2O_5$ to reveal the martensite. The 4% chromium series was immersed for 10-20 seconds, while the 12% chromium series was immersed for 30-40 seconds in view of its higher corrosion resistance.

Subsequent microscopic observations were conducted with a Nikon optical light microscope.

3.6   SCANNING ELECTRON MICROSCOPY

Fracture toughness specimens were cooled in liquid nitrogen after the toughness testing and immediately broken open to reveal the fracture surface. Fracture surfaces of both tensile specimens and fracture toughness specimens were examined on either an AMR-1000 scanning electron microscope operating at 20 kV, or on an Hitachi scanning electron microscope operating at 20 kV. The specimens were sometimes coated with gold.

CHAPTER 4

RESULTS AND DISCUSSION

4.1 FLOW BEHAVIOR IN UNIAXIAL TENSION

Figure 4.1 presents the true stress-strain curves for the 4% chromium series. The arrows indicate where final necking occurs. The significant difference in flow behavior for the three different nickel compositions reflects the difference in austenite stability and the influence of mechanically-induced martensite. The austenite stability increases as the nickel content increases. Alloy 428 exhibits the customary negative curvature while alloys 424 and 425 show at low strains, positive curvature followed by, at larger strains, negative curvature.

The initial positive curvature of alloys 424 and 425 can be explained with the help of Figure 4.2 which again includes the tensile curves of alloys 424 and 425 with the hardening rate, $d\sigma/d\varepsilon$, superimposed. When $d\sigma/d\varepsilon > \sigma$, flow is stable; but when $d\sigma/d\varepsilon$ becomes less than σ, flow localizes and tensile instability occurs. As illustrated in Figure 4.2, initial tensile instability occurs at very low strains, <0.01 for 424 and ~0.02 for 425. This initial localization of the flow behavior is due to a Lüders front propagating through the specimen. When the Lüders front has propagated through the entire specimen, flow stabilizes, i.e., $d\sigma/d\varepsilon > \sigma$, and homogeneous straining of the entire specimen continues with the deformation until final localization/necking occurs.
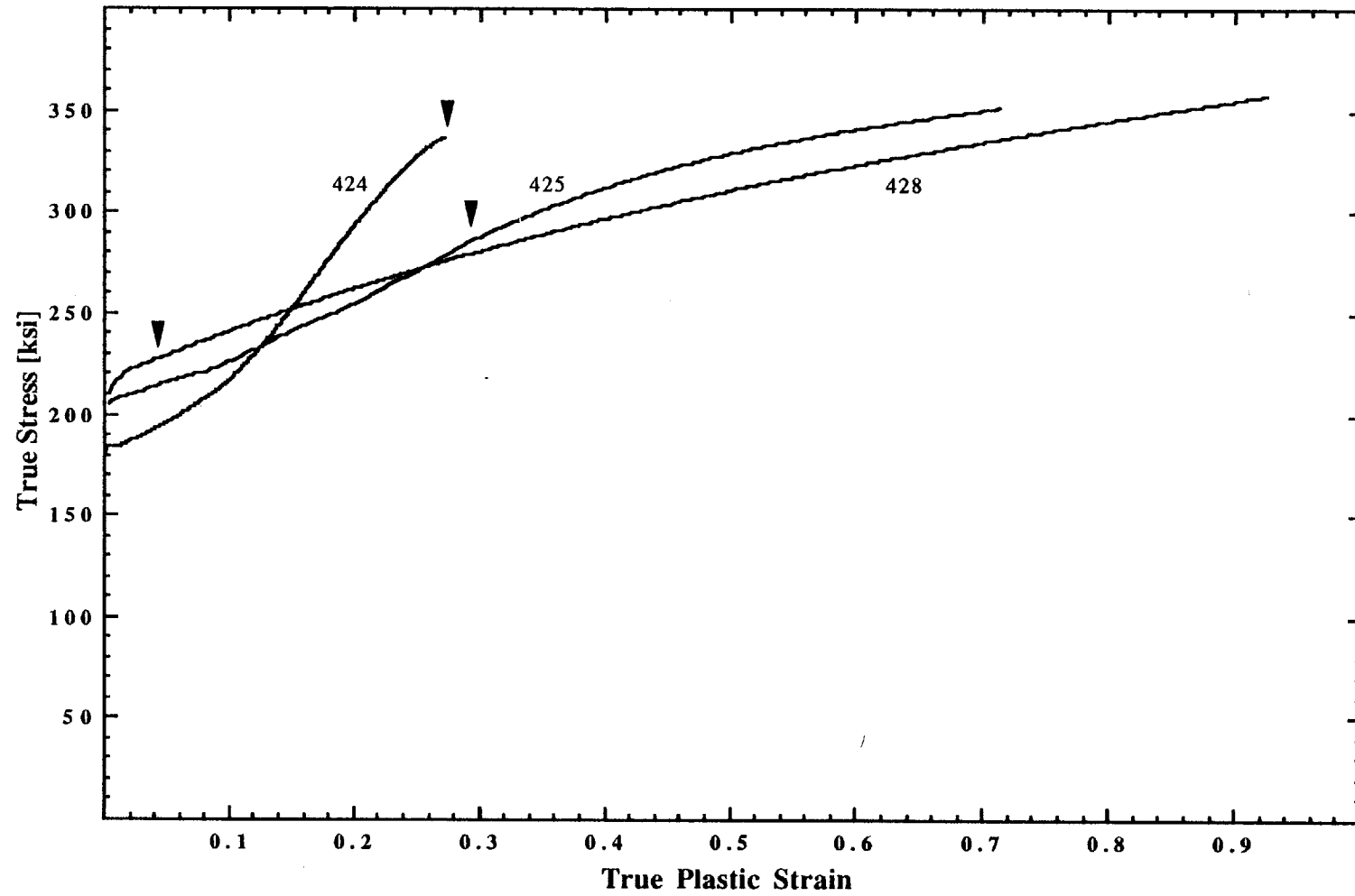
Figure 4.1 Tensile curves for 4% chromium series. Arrows correspond to points of necking.
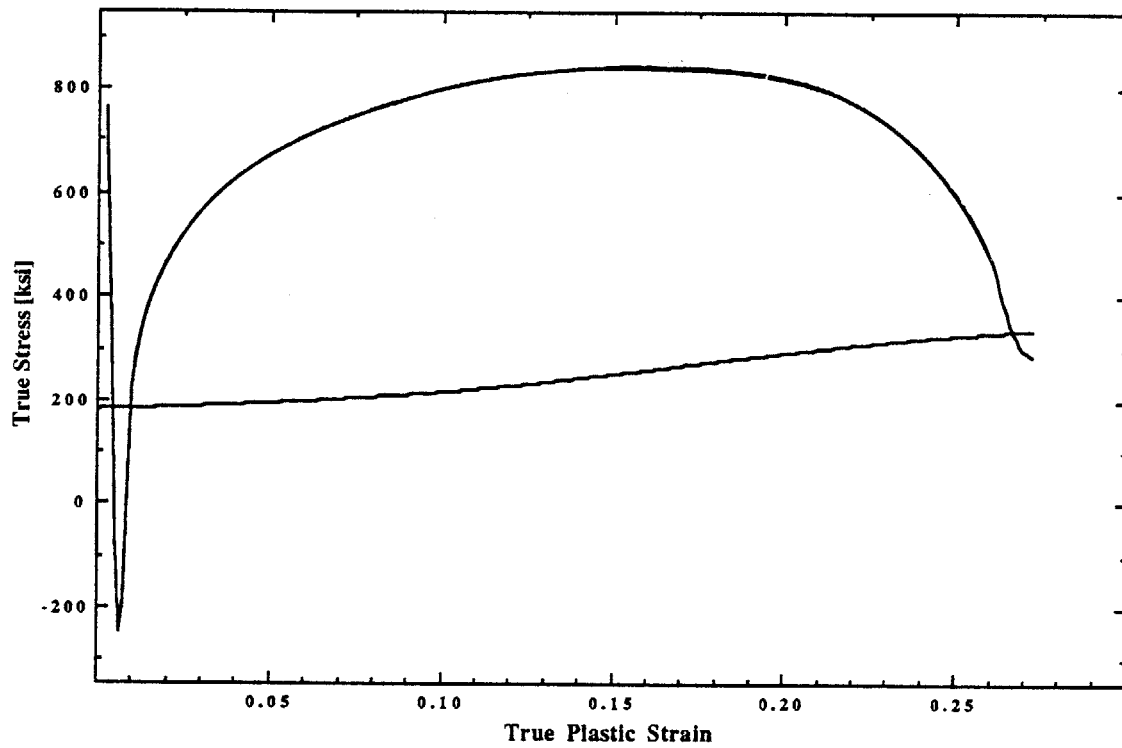
Figure 4.2a Tensile curve and hardening rate for alloy 424.
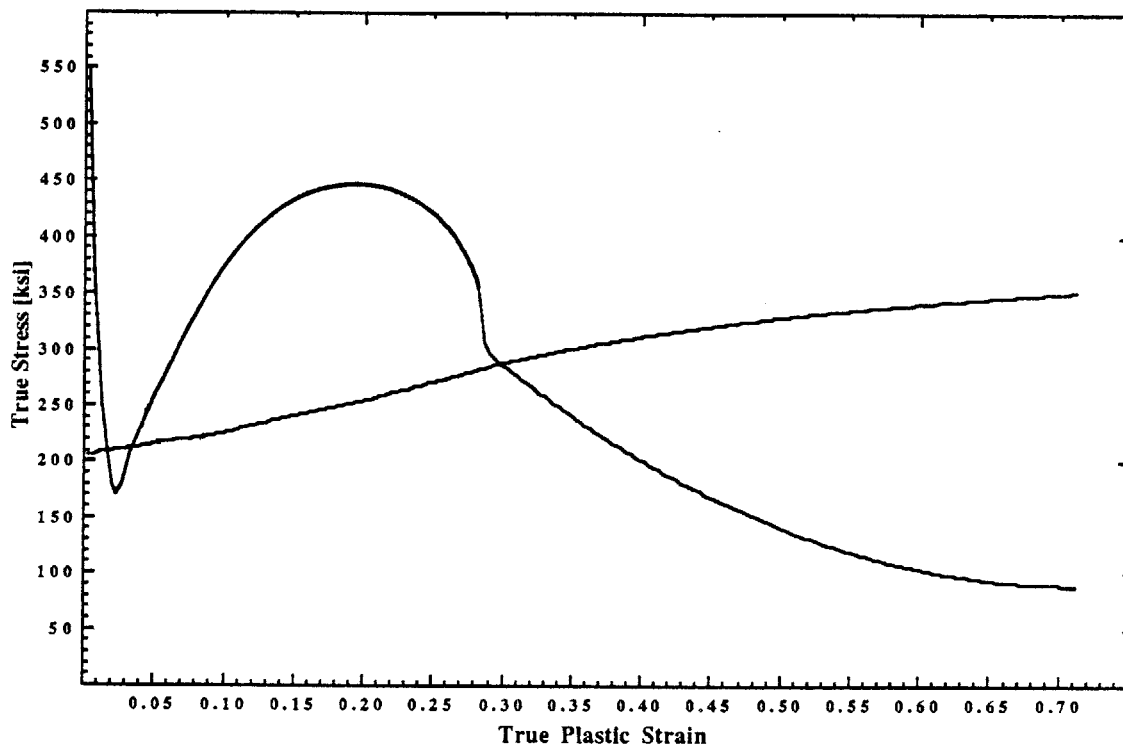
Figure 4.2b Tensile curve and hardening rate for alloy 425.

In comparing the two hardening rates in Figures 4.2a and b, it can be seen that the hardening rate of alloy 425 varies over a smaller range. A smaller variation of the hardening rate leads to a closer matching of the stress-strain curve to ideal exponential hardening behavior:

$$\sigma = \sigma_y \exp(\varepsilon) \qquad (4.1)$$

where σ_y is the yield stress. Equation (4.1) always results in a positive curvature and hence final necking will "never" occur. A close relationship to equation 4.1 will therefore delay final necking until larger strains.

The initial drop in hardening rate is steeper for alloy 424, signifying that the dynamic softening is greater. Dynamic softening is dominant at lower strains and is proportional to $d^2 f_\alpha / d\varepsilon_p^2$ [22]. At increasing strains, the dynamic softening effect becomes weaker as the static hardening rate, proportional to $df_\alpha / d\varepsilon_p$, becomes stronger. This causes the drop in hardening rate to diminish and the observed hardening rate starts to increase. At even higher strains, the transformation becomes exhausted and the static hardening effect now diminishes. This causes the hardening rate to reach a maximum and start dropping again. Final necking sets in when the hardening rate becomes equal to the stress.

Figure 4.3 presents the true stress-strain curves for the 12% chromium series. The arrows indicate where final necking occurs. All four alloys illustrate the customary negative curvature. Final necking for all four alloys occurs at very low strains, but the fracture strains for some of these alloys are larger than for alloy 428.

4.1.1 TRANSFORMATION STABILITY VERSUS COMPOSITION

Figure 4.4 shows the true yield stress and the true ultimate tensile stress versus nickel content for both the 4% chromium series and the 12% chromium series. A
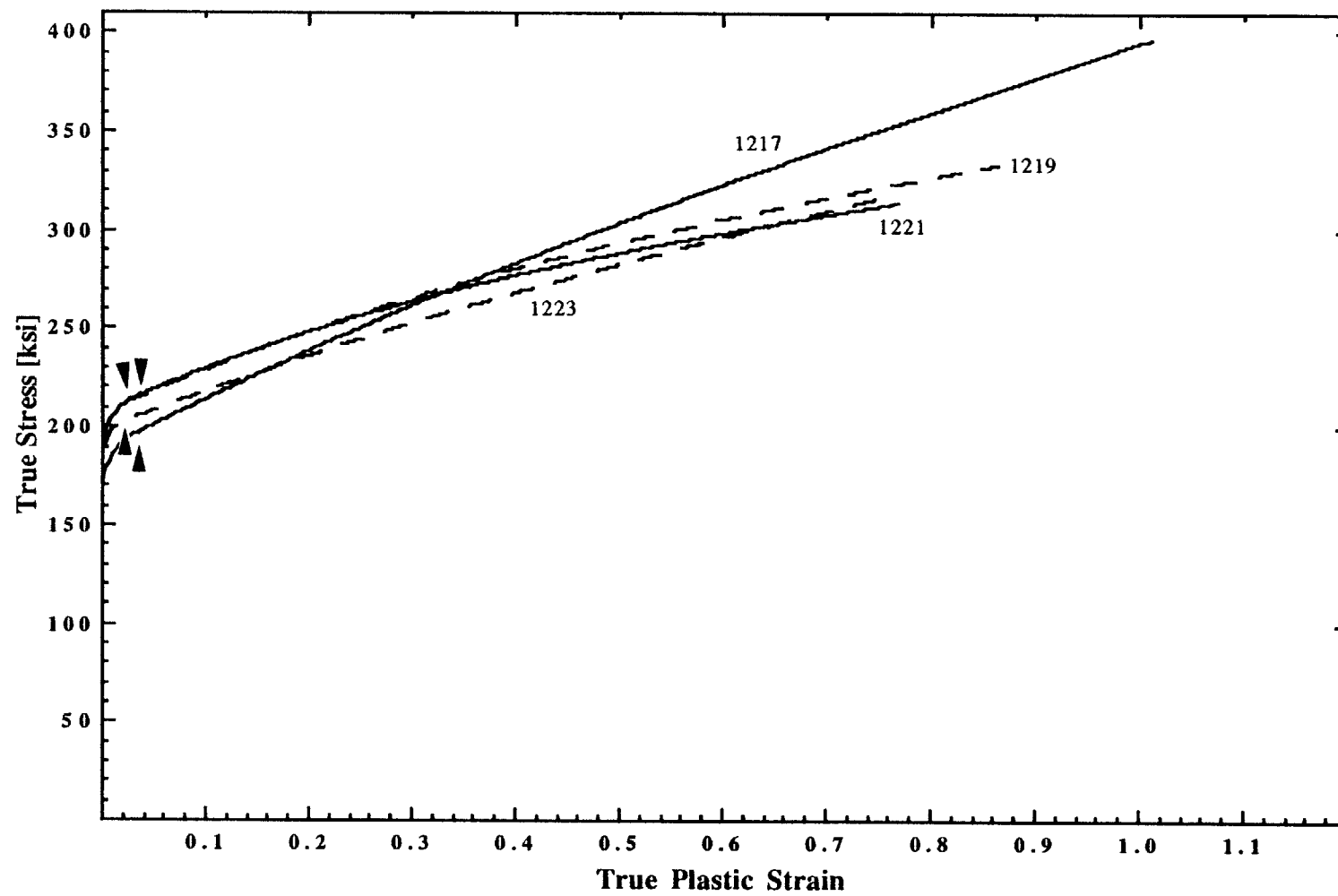
Figure 4.3 Tensile curves for 12% chromium series. Arrows correspond to points of necking.
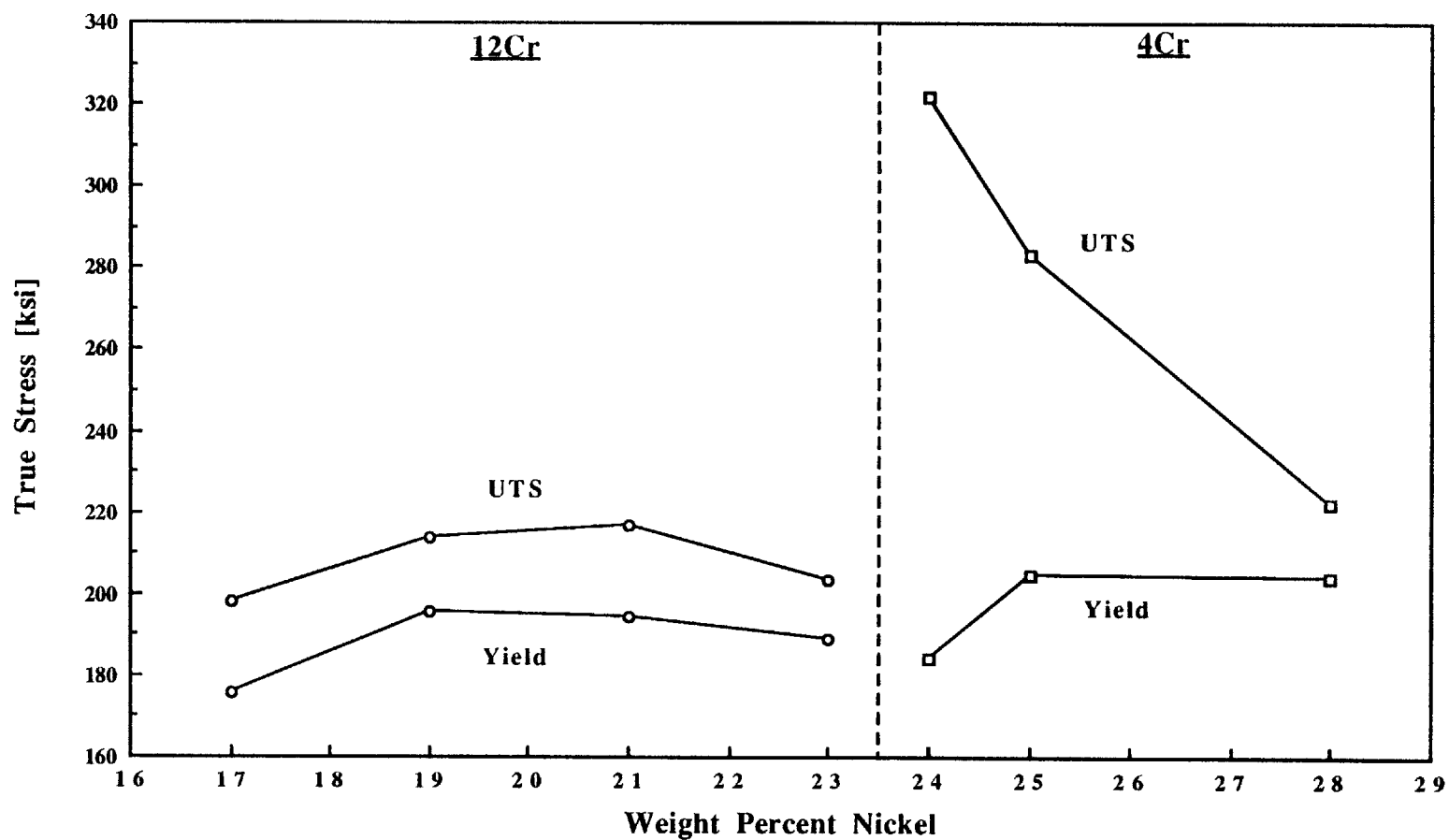
Figure 4.4 True yield stress and true ultimate tensile stress for 4% chromium series and 12% chromium series.

maximum in yield strength is indicative of the M_s^σ-temperature for uniaxial tension as illustrated in Figure 2.1. Figure 2.1 plots stress versus temperature while Figure 4.4 plots stress versus percent nickel. Keeping the test temperature constant and varying the nickel content changes the chemical driving force in a manner similar to keeping the composition constant and varying the test temperature. Therefore, keeping the temperature constant and varying nickel content is equivalent to keeping the composition constant and varying the temperature. A graph showing stress versus percent nickel for these alloys should therefore resemble a graph showing stress versus temperature.

The ultimate tensile stress reaches a maximum in the stress-assisted region, and the maximum in yield stress corresponds to M_s^σ in uniaxial tension [54]. Optical metallography confirmed this for alloy 424 which revealed plate martensite in the broken tensile specimen. Alloy 425 contained less plate martensite in the uniformly elongated region; whereas alloy 428 disclosed no martensite in the uniformly elongated region. Based on these metallographic observations and Figure 4.4, alloy 425 is likely to have M_s^σ for uniaxial tension at room temperature.

In the 12 % chromium series, the true ultimate stress is 15-20 ksi higher than the yield stress. Optical metallography of the 12% chromium series revealed no martensite in the uniformly elongated part of the tensile specimen. Based on these metallographic observations and Figure 4.4, the M_s^σ for uniaxial tension cannot be obtained at room temperature in the 12% chromium series. An alloy with 12% chromium has very low temperature sensitivity and the nickel content would have to be much less than 17 percent in order to place the M_s^σ for uniaxial tension at room temperature.

4.1.2 UNIFORM DUCTILITY

Figure 4.5 shows the uniform ductility for both the 4% and the 12% chromium series. The reason for the very large uniform strains of alloys 424 and 425 is because of mechanically-induced martensite. As the initial localization, or Lüders band formation, occurs, mechanically-induced martensite starts to form. This happens because the stability of the austenite is such that the mechanical driving-force contribution due to the uniaxial stress state, triggers the martensitic transformation. Accompanying the martensitic transformation is a positive volume change and a transformation strain. The additional straining of the specimen is entirely due to this transformation strain. Compared to stable austenite, there is initially a dynamic softening followed by static hardening when mechanically-induced martensite is formed. Both contributions are important factors in delaying final necking [22]. In alloy 424 the static hardening contribution is large and the martensitic transformation is prematurely exhausted, and so final fracture occurs before necking. Alloy 424 is therefore too unstable for optimum uniaxial tensile deformation. In alloy 425, the static hardening is smaller than in alloy 424. This indicates that the austenite stability is more balanced for uniaxial tension. The martensitic transformation does not advance to early exhaustion before necking and final fracture occurs after a period of negative curvature. Alloy 428 has a necking strain of only 0.0205. This suggests that the austenite stability is such that no, or negligible, martensite is formed prior to necking.

Maximum uniform elongation is observed slightly above M_s^σ for uniaxial tension [1]. Both maximum uniform strain, and maximum yield stress for the 4% chromium series is found in alloy 425 at room temperature. Maximum yield stress corresponds to M_s^σ for uniaxial tension so therefore, alloy 425 at room temperature is at M_s^σ for uniaxial tension. Still higher uniform elongation for the 4% chromium series is probably found in an alloy with approximately 26% nickel.
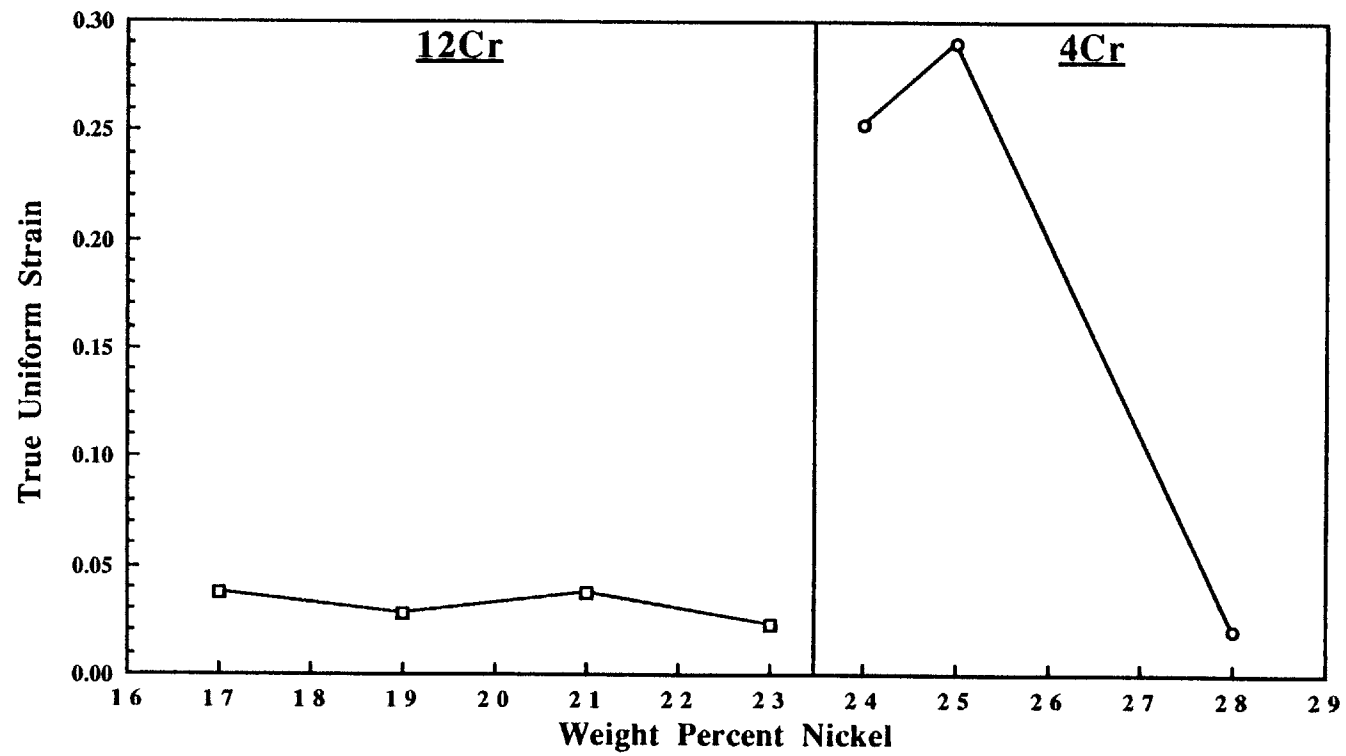
Figure 4.5 Uniform strain for 4% chromium series and 12% chromium series.

The 12% chromium series exhibits low uniform strains similar to that of alloy 428. No martensite was found in the uniformly elongated region of the tensile specimen in either case. This indicates a relatively high stability of the parent austenite.

Table 4.1 summarizes the tensile properties of both the 4% chromium series and the 12% chromium series. Discussions regarding the fracture strain, ε_f, and necking strain, ε_n, will be postponed until section 4.2.2.

The stability of the austenite can drastically change the flow behavior of the material. Low stability of the austenite produces mechanically-induced martensite which alters the stress-strain curve from negative to positive curvature, delaying the onset of necking. The 4% chromium series has the lower austenite stability, and alloy 425 displays a fifteenfold improvement in uniform elongation due to mechanically-induced martensite over the more stable alloy 428. Furthermore, the most unstable alloy 424, shows a fifty percent increase in ultimate tensile strength over alloy 428 because of the mechanically-induced martensite.

4.2 FRACTURE BEHAVIOR

The 12% chromium series was pre-cracked for approximately 25000 cycles, while the 4% chromium series only took around 17500 cycles. This qualitative observation of a difference in fatigue crack growth rate (FCGR) of the two series can possibly be related to the difference in stacking-fault energy. This has previously been observed in copper-base alloys, where it was found that when the stacking-fault energy decreases, so does the FCGR [55,56,57,58]. Thus, if cross slip is made more difficult the fatigue crack growth is expected to decrease.

82

ALLOY	σ_y [ksi]	σ_y [MPa]	σ_u [ksi]	σ_u [MPa]	ε_u	ε_f	ε_n
424	184.1	1269	321.9	2220	0.2534	0.2534	0
425	204.9	1413	283.2	1953	0.2909	0.7122	0.4213
428	204.1	1407	222.2	1532	0.0205	0.9250	0.9045
1217	175.8	1212	197.8	1364	0.0377	1.0111	0.9734
1219	195.4	1347	213.6	1473	0.0283	0.8634	0.8352
1221	194.2	1339	216.8	1495	0.0379	0.7678	0.7299
1223	188.8	1302	203.2	1401	0.0233	0.7523	0.7289

Table 4.1 Tensile properties of 4% and 12% chromium series.

4.2.1 J_{IC} FRACTURE TOUGHNESS VERSUS COMPOSITION

Figure 4.6 shows the J_{IC} fracture toughness at room temperature for the 4% chromium series and the 12% chromium series. The dashed line indicates the J_{IC} fracture toughness for a stable austenitic alloy. This baseline value was obtained by conducting a fracture toughness test of the most stable alloy 1223 at an elevated temperature of 225°C to prevent formation of martensite. In comparing the J_{IC} fracture toughness for all the tested alloys to the baseline value, it is clear that the presence of mechanically-induced martensite can greatly enhance the fracture toughness properties.

The most unstable alloy 424 shows that in the presence of stress-assisted martensite there is only a small improvement in fracture toughness. An even more unstable 4% chromium alloy is likely to exhibit a fracture toughness value below the baseline value of stable austenite. Leal [1] showed that the flat fracture mode associated with plate martensite can lead to large reductions in fracture toughness in comparison to the fracture toughness of stable austenite.

Alloy 425 is at room temperature slightly above the M_s^σ for uniaxial tension. Because of the large temperature-sensitivity of the 4% chromium series, alloy 425 is expected to be too unstable in the crack-tip mode. Optical metallography confirmed this by revealing only plate martensite around the crack tip. The higher austenite stability in alloy 425 compared to alloy 424, gives a higher fracture toughness value. This is to be expected since in the stress-assisted region a higher stability has been shown to give a higher fracture toughness value [1].

Alloy 428 exhibits the highest fracture toughness in the 4% chromium series. Optical metallography revealed fine strain-induced lath martensite around the crack tip. The substantial enhancement in fracture toughness over alloys 424 and 425 is due to the change in morphology of the mechanically-induced martensite from plate martensite to fine lath

84
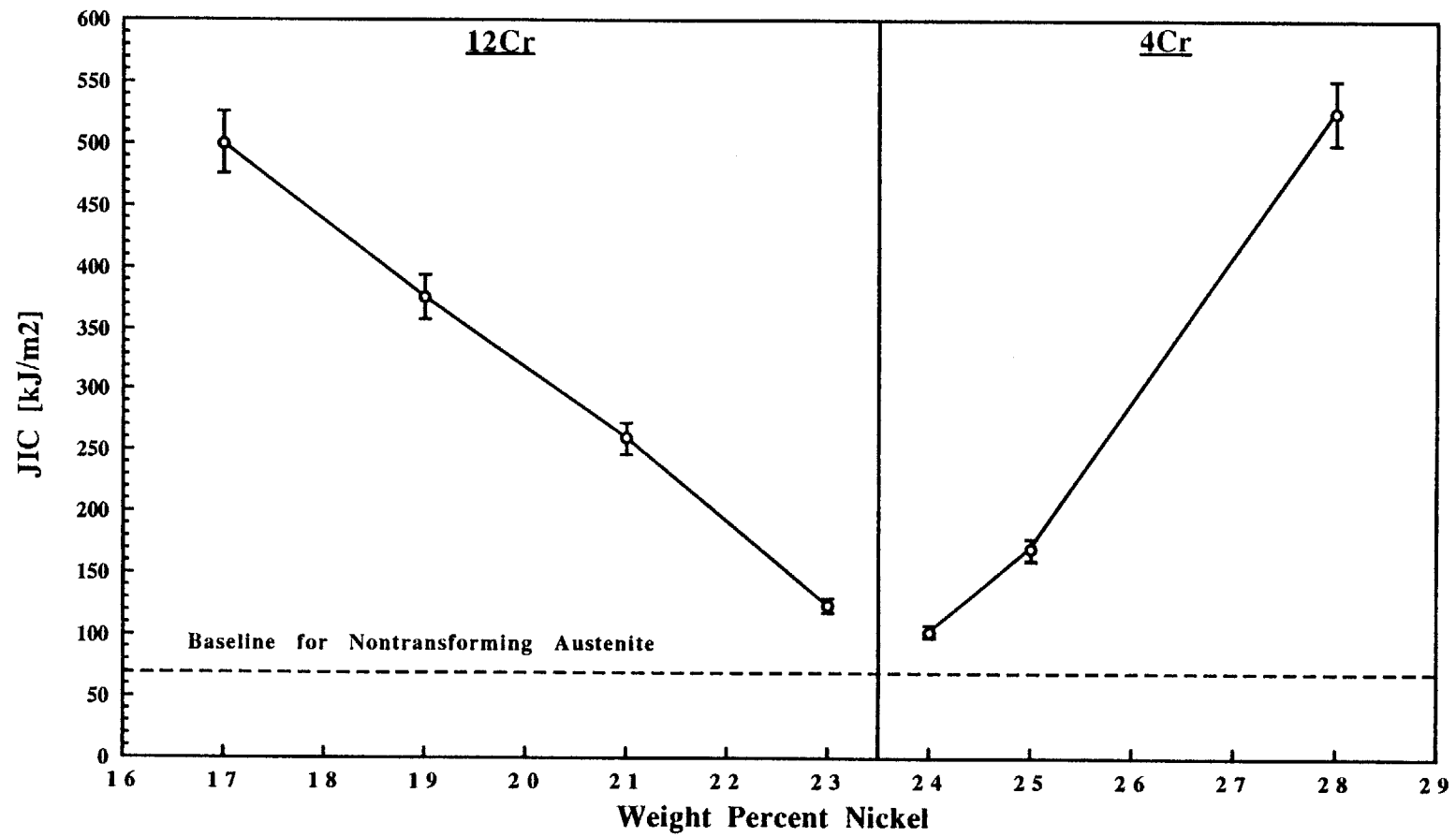
Figure 4.6 J_{IC} fracture toughness for 4% chromium series and 12% chromium series.

martensite. This changes the flat fracture mode to a shear-instability controlled fracture mode. Maximum fracture toughness is expected close to the transition between these two fracture modes [1]. Since there is no apparent maximum in the fracture toughness data for the 4% chromium series, it is hard to predict the nickel content for maximum fracture toughness. However, alloy 428 is probably very close to optimum nickel content because of the high temperature sensitivity of the 4% chromium series.

The 12% chromium series exhibits a range of fracture toughness values similar to the 4% chromium series. The 12% chromium series showed strain-induced lath martensite surrounding the crack. This indicates that the austenite stability of the 12% chromium series is on the high side as compared to the 4% chromium series, the latter lying mainly on the unstable side as previously discussed. The increase in fracture toughness with decreasing austenite stability in the region controlled by shear-instability fracture is in agreement with the findings of Leal [1].

As in the case of the 4% chromium series, there is no apparent maximum in the fracture toughness data for the 12% chromium series, but alloy 1217 is believed to be near the maximum fracture toughness. This supposition is based on crack-tip sectioning observations which occasionally disclosed a mixture of plate martensite and fine strain-induced lath martensite. This observation is indicative of the M_s^σ-temperature where, as discussed earlier, maximum fracture toughness is obtained.

The load-displacement curves in the fracture toughness testing of all seven alloys and the elevated temperature test for alloy 1223 exhibit very different behavior. The elevated temperature test for alloy 1223 shows very little deviation from a linear relationship between load and displacement. This is, therefore, a valid K_{IC} fracture toughness test. Alloy 424 deviates more than allowed in Standard E399 [50] from the linear relationship between load and displacement and the fracture test is therefore not a

valid K_{IC} fracture toughness test. Instead, a J_{IC} fracture toughness test is adopted. As the fracture toughness in Figure 4.6 increases, starting from alloy 424, the deviation from linearity between load and displacement becomes larger and larger, and the load-displacement curve for alloy 1219 is almost horizontal at maximum load. This represents the effect of the strain-induced martensite on displacement enhancement. The load-displacement curves for alloys 428 and 1217 undergo a remarkable change. The customary negative curvature changes partially to a positive curvature before maximum load is reached, as illustrated in Figure 4.7 for alloy 428. This is very similar to the behavior in tension of alloys 424 and 425 where the mechanically-induced martensite delays the onset of tensile instability. Figure 4.7 demonstrates that mechanically-induced martensite can also change the shape of the load-displacement curve from negative to positive curvature and delay the onset of fracture instability to a higher load and larger displacement. This phenomenon will therefore result in a higher fracture toughness since it is found that the maximum of the load-displacement curve relates closely to the J_{IC} fracture toughness value. This curve-shaping effect in a fracture toughness test has not previously been reported. Load-displacement curves for all alloys are found in Appendix C.

4.2.2 FRACTURE DUCTILITY

Figure 4.8 plots the strain to failure and uniform strain at room temperature for the 4% and 12% chromium series. The 4% series exhibits a quite different behavior from that of the 12% chromium series. Table 4.1 lists the tensile properties for both series.

Alloy 424 fractured during uniform elongation. As already discussed in section 4.1.2, this is because of the low stability of the austenite. The large static hardening component leads to early exhaustion of the martensitic transformation. Optical metallography revealed only plate martensite in alloy 424.
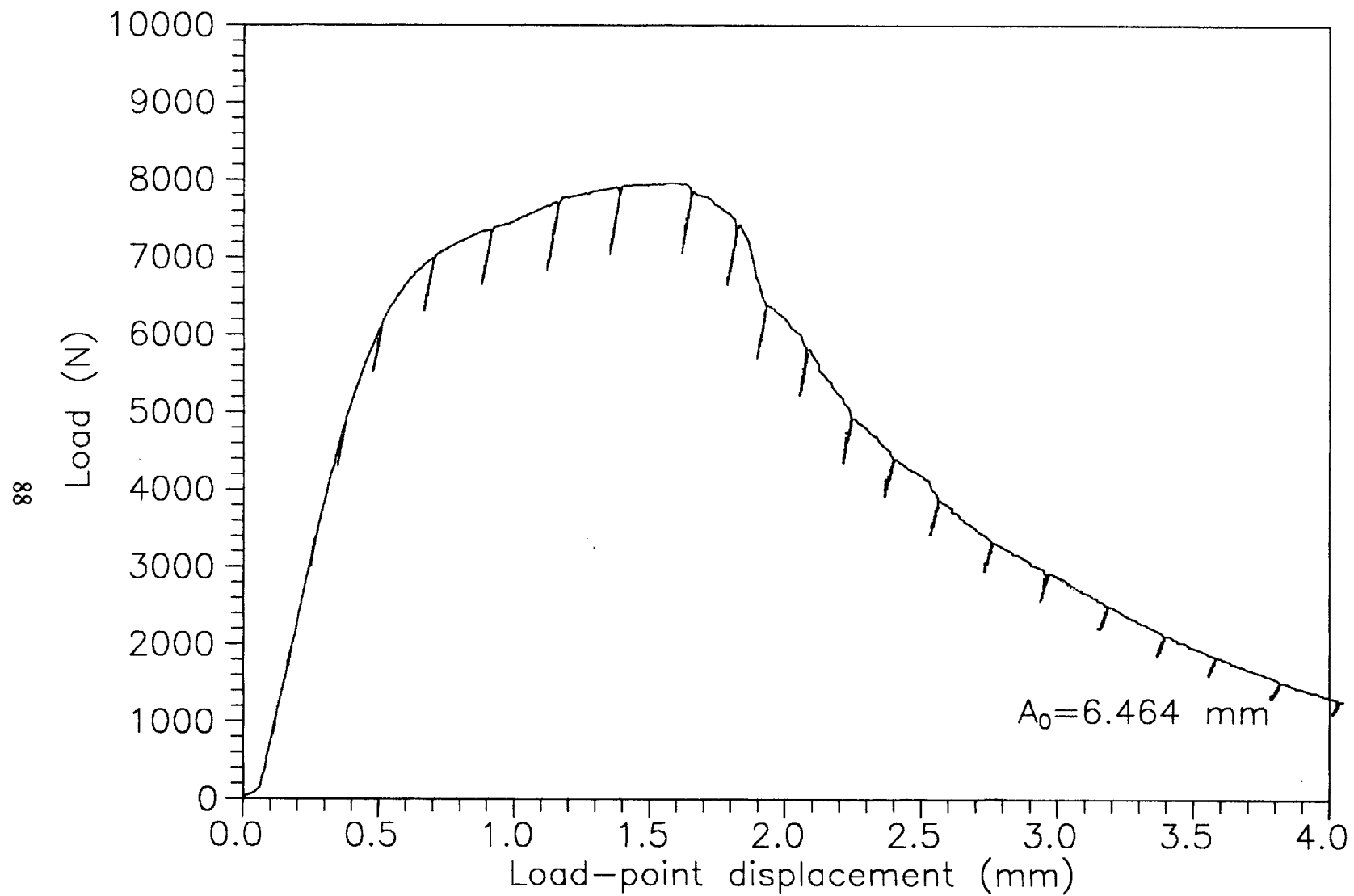
Figure 4.7 Load-displacement curve for alloy 428.
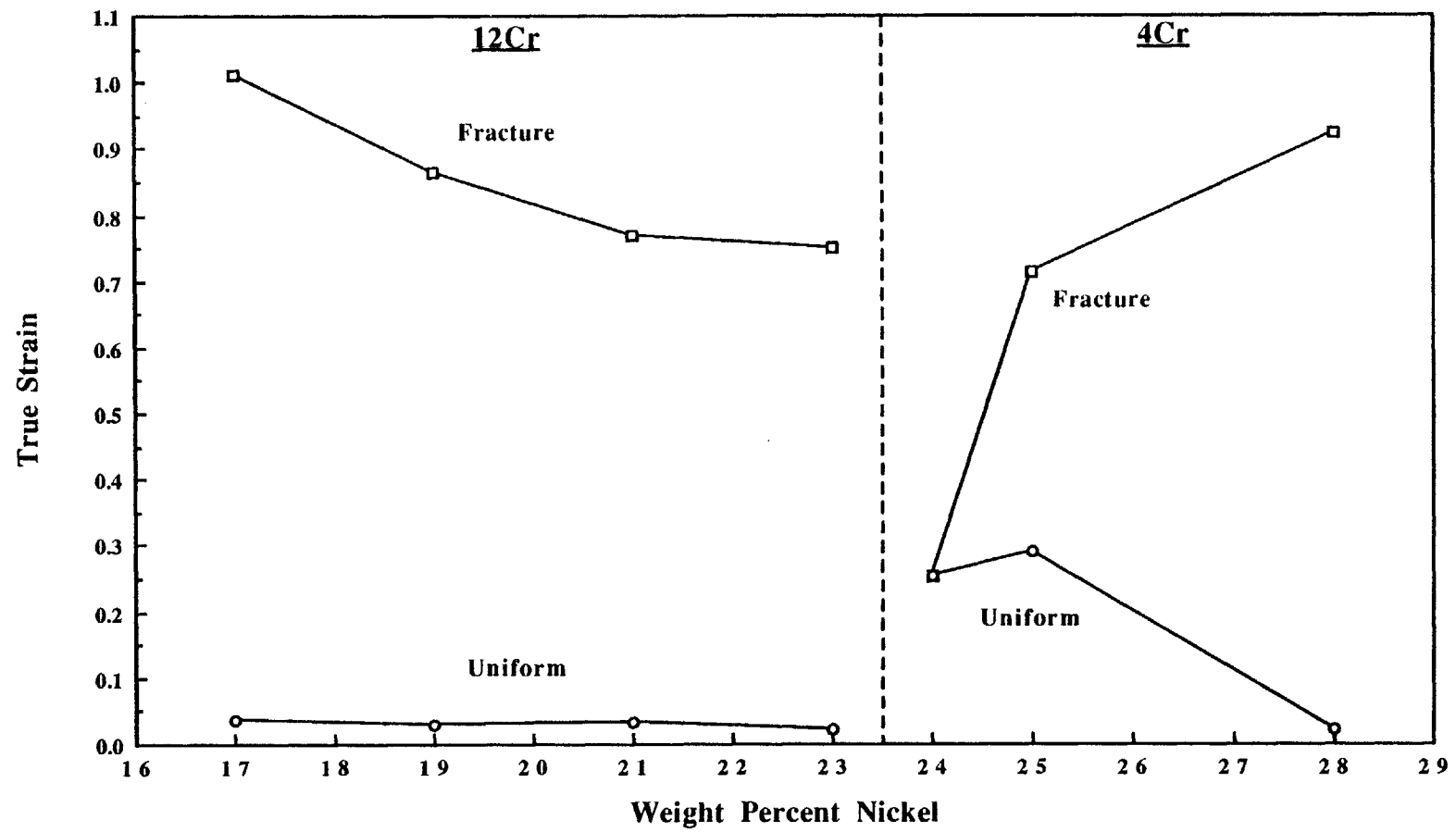
Figure 4.8 Uniform strain and strain to failure for 4% chromium series and 12% chromium series.

The higher stability alloy 425 exhibits an increase in fracture strain. Fine strain-induced lath martensite is formed in the necked region of the broken tensile specimen in addition to the plate martensite observed in the uniformly elongated section. The mixture of plate martensite and lath martensite is typical for an alloy with stability corresponding to the M_s^σ-temperature for uniaxial tension. It is believed that alloy 425 at room temperature is at M_s^σ in uniaxial tension.

Alloy 428 has the highest strain to failure in the 4% chromium series. Fine strain-induced lath martensite appears in the necked region of the broken tensile specimen while no martensite is observed in the uniformly elongated section.. Alloy 428 has the highest stability in the 4% chromium series and the mechanical driving-force contribution during uniform elongation is too low to induce the martensitic transformation; hence, the low uniform ductility. The triaxial stress state during necking provides a high enough mechanical driving force to induce the martensitic transformation. The transformation strain accompanying the mechanically induced martensite now provides the large strain to fracture, as was already discussed in section 4.1.2, for large uniform ductility. The higher stability of the austenite in alloy 428 therefore produces mechanically-induced martensite during the necking of the tensile specimen, giving rise to large necking strains and delaying final fracture. Alloy 428 is believed to have its M_s^σ close to room temperature for the triaxial stress state during necking.

For the 4% series, alloy 428 has the optimum stability at room temperature to provide large strain to failure, while alloy 425 has the optimum stability at room temperature for large uniform strain and alloy 424 has the optimum stability at room temperature for large ultimate tensile strength. To obtain these combinations in such a narrow range of compositions is remarkable. The large temperature sensitivity of the 4% chromium series makes this possible. It would possess some danger though, since a small variation of the temperature could drastically alter the mechanical properties of the alloy.

90

The 12% chromium series exhibits a strain to failure ranging from 0.75 for alloy 1223 to 1.01 for alloy 1217. As with alloy 428, fine strain-induced lath martensite is found in the necked region of the broken tensile specimens whereas no martensite is observed in the uniformly elongated sections. In addition, there is also an increase in the density of the strain-induced lath martensite from alloy 1223 to alloy 1217. These observations signify that the room-temperature stability of the 12% chromium series is such that the mechanical driving force contribution is too low to induce the martensitic transformation during uniform elongation. During necking though, new highly potent martensitic nucleation sites are created. This, in conjunction with the additional mechanical driving force provided by the triaxial stress-state, triggers the martensitic transformation and results in large strain to failure. This indicates that strain-induced martensite formed during the necking sequence will delay final fracture and thus will promote a larger strain to failure. Alloy 1217, which is the least stable, undergoes the highest strain to failure and also forms the largest density of strain-induced lath martensite. Thus, a larger fraction of strain-induced martensite during necking promotes a larger strain to failure.

Because of the lower temperature sensitivity in the 12% chromium series, the variation in strain to failure is not as large as in the 4% chromium series. This was one of the objectives of the present research, as discussed in Chapter 1, and the high chromium addition appears to have been successful. One might wonder if a 12% chromium alloy with less than 17 weight percent nickel would have even larger strain to failure. This seems possible, but based on the record high fracture toughness value obtained for alloy 1217, as discussed in the previous section, and the close relation between fracture toughness and strain to failure, it seems unlikely that even more strain to failure, and hence fracture toughness, could be obtained. Only future research will be able to answer this question and it is left as a suggestion in chapter 6.

The broken tensile specimens of the 4% and 12% chromium series were investigated in a scanning electron microscope. Figures 4.9 to 4.12 show the tensile fractures of the 12% chromium series. Alloys 1223 and 1221 exhibit a ductile cup-and cone-fracture behavior. There is a 100% fibrous zone in the middle of the fracture surfaces where microvoid nucleation, growth, and coalescence occur. This slow fracture process reduces the load-bearing capacity of the specimen and finally a fast shear fracture at a 45 degree angle to the loading axis takes place. Examination of the fracture surfaces indicated a pure dimple rupture mode of failure.

Alloy 1219 shows only a very small fibrous zone. Most of the fracture is a 45 degree shear fracture. The shear lips lying in different planes are connected by a vertical fracture plane. This final fast fracture extends past the surfaces of the shear lips. This crack extension is probably a dynamic fracture arrest zone. Examination of the fracture surface in the center of the specimen indicates a quasicleavage mode of failure.

Alloy 1217 exhibits only shear fracture with smaller zig-zag spacings than observed above. This is probably promoted by the greater amount of strain-induced martensite in alloy 1217. The vertical splitting noted in this case is not related to dynamic crack arrest. Bramfitt and Marder [59] have pointed to a whole array of mechanisms that may cause, or contribute to, splitting. The splitting must be related to the strain-induced martensite and the higher triaxial stress in the necked region compared to the other alloys. The most likely mechanism is a grain-boundary weakness disclosed by the large elongation during necking due to the strain-induced martensite, and the accompanying high triaxial stress.

Figures 4.13 to 4.15 show the broken tensile specimens of the 4% chromium series. Alloy 424 exhibits a brittle fracture mode due to the stress-assisted martensite. Some quasicleavage is present. Examination of the fracture surface revealed some grain boundary microcracking.

Figure 4.9 Tensile fracture surface of alloy 1223. Arrow indicates area of high magnification.

Figure 4.10 Tensile fracture surface of alloy 1221. Arrow indicates area of high magnification.

Figure 4.11 Tensile fracture surface of alloy 1219. Arrow indicates area of high magnification.

Figure 4.12 Tensile fracture surface of alloy 1217. Arrow indicates area of high magnification.
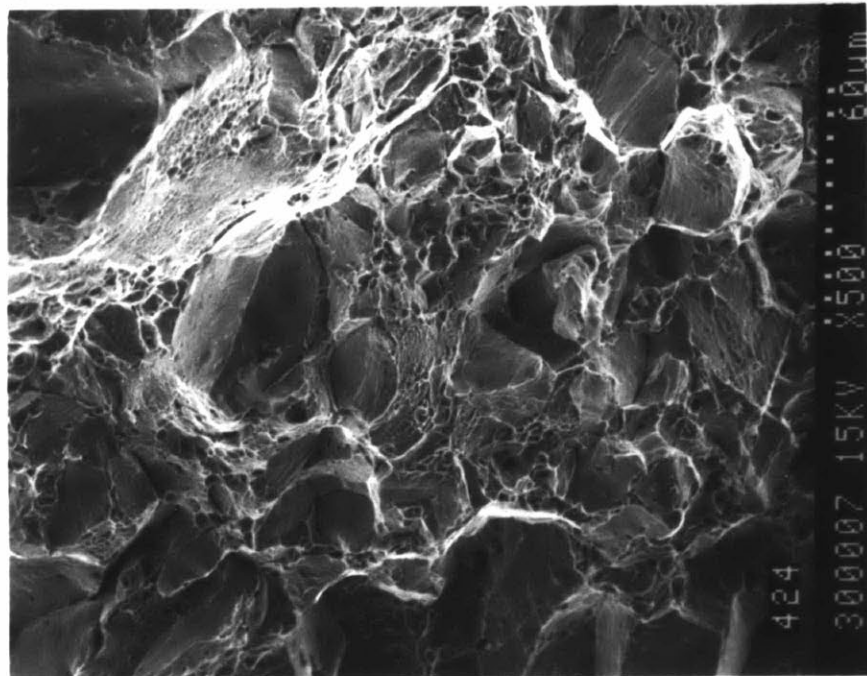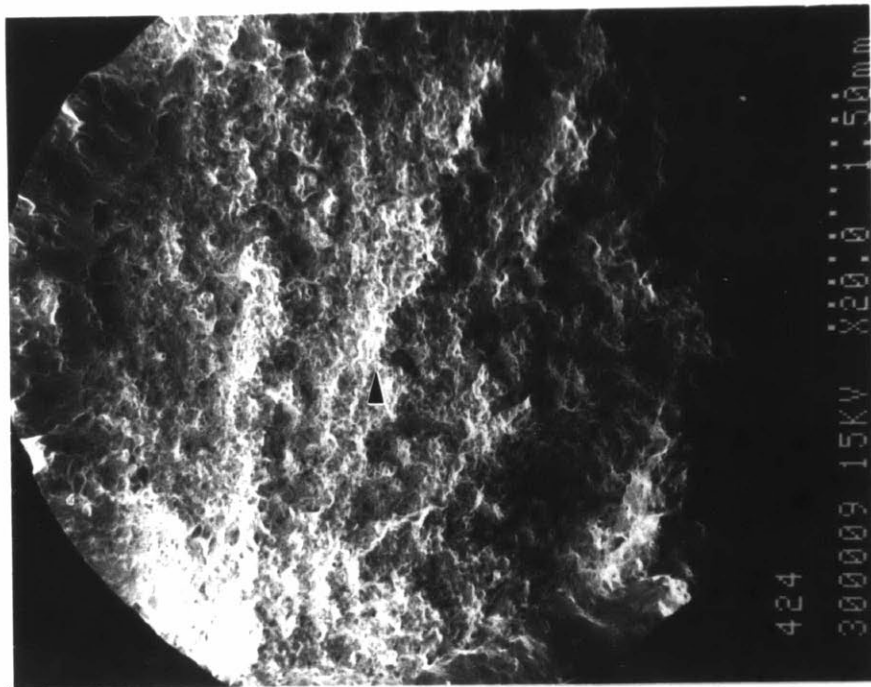
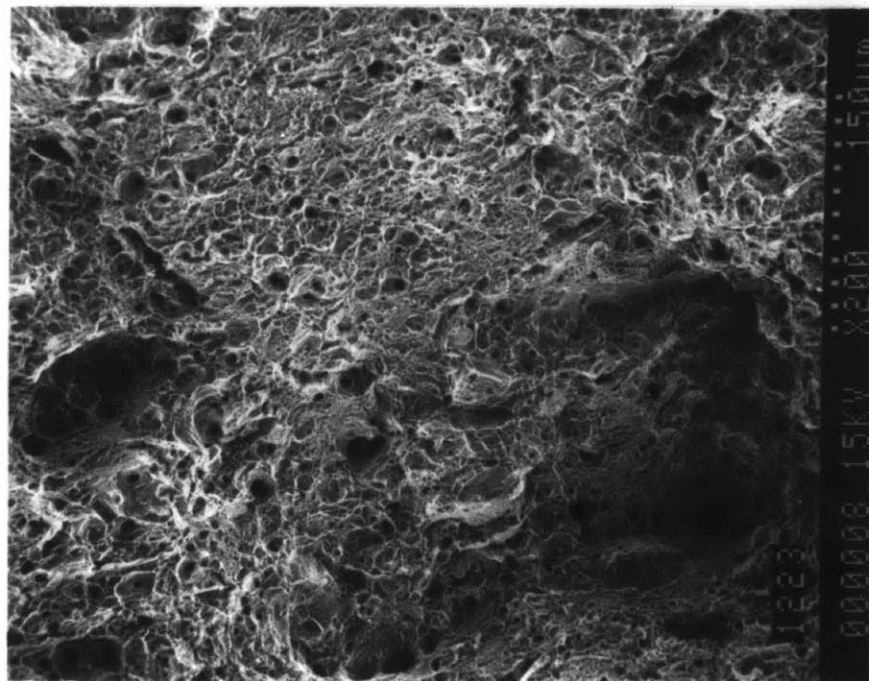**Figure 4.13** Tensile fracture surface of alloy 424. Arrow indicates area of high magnification.
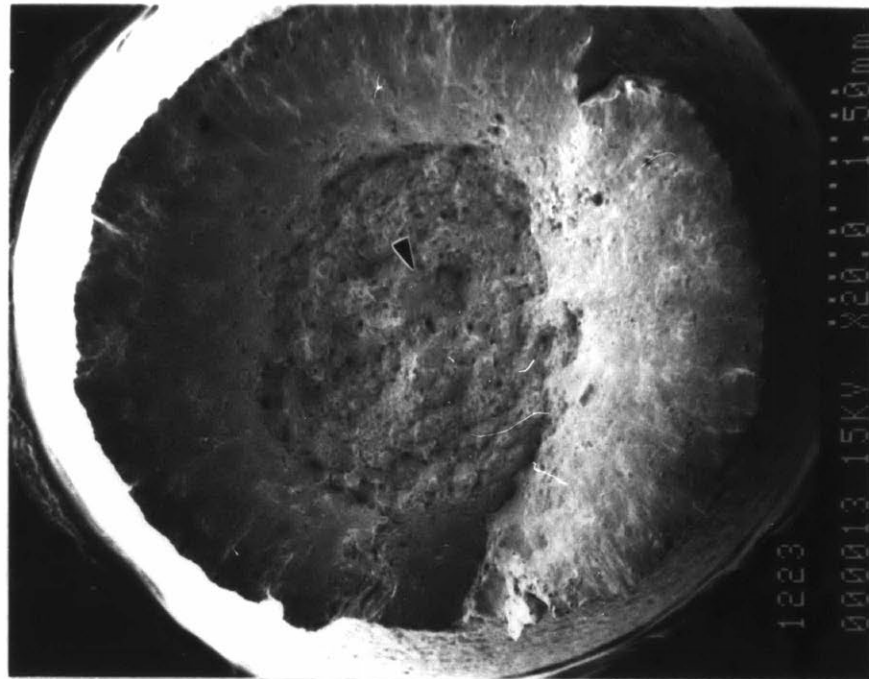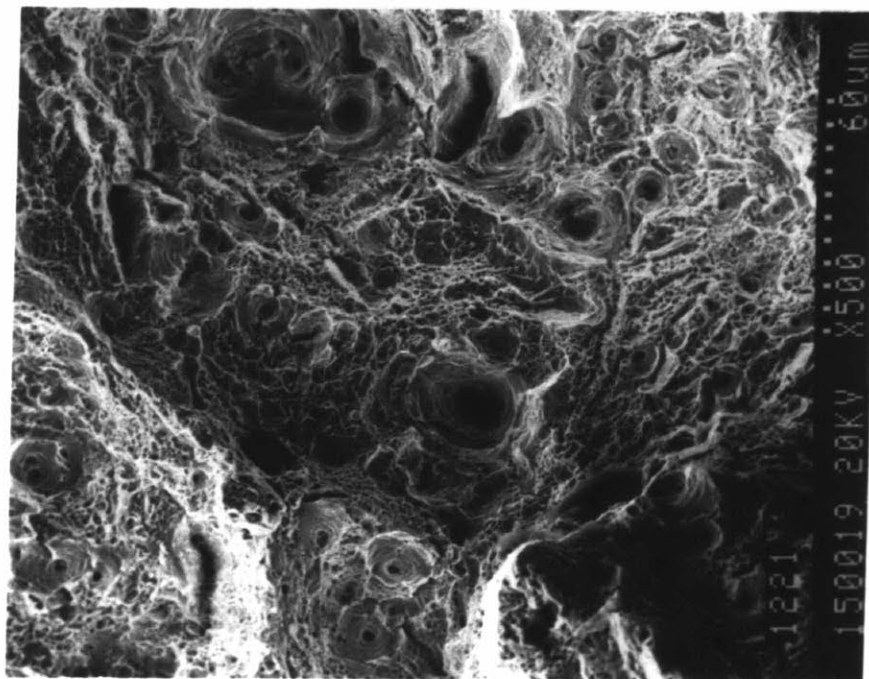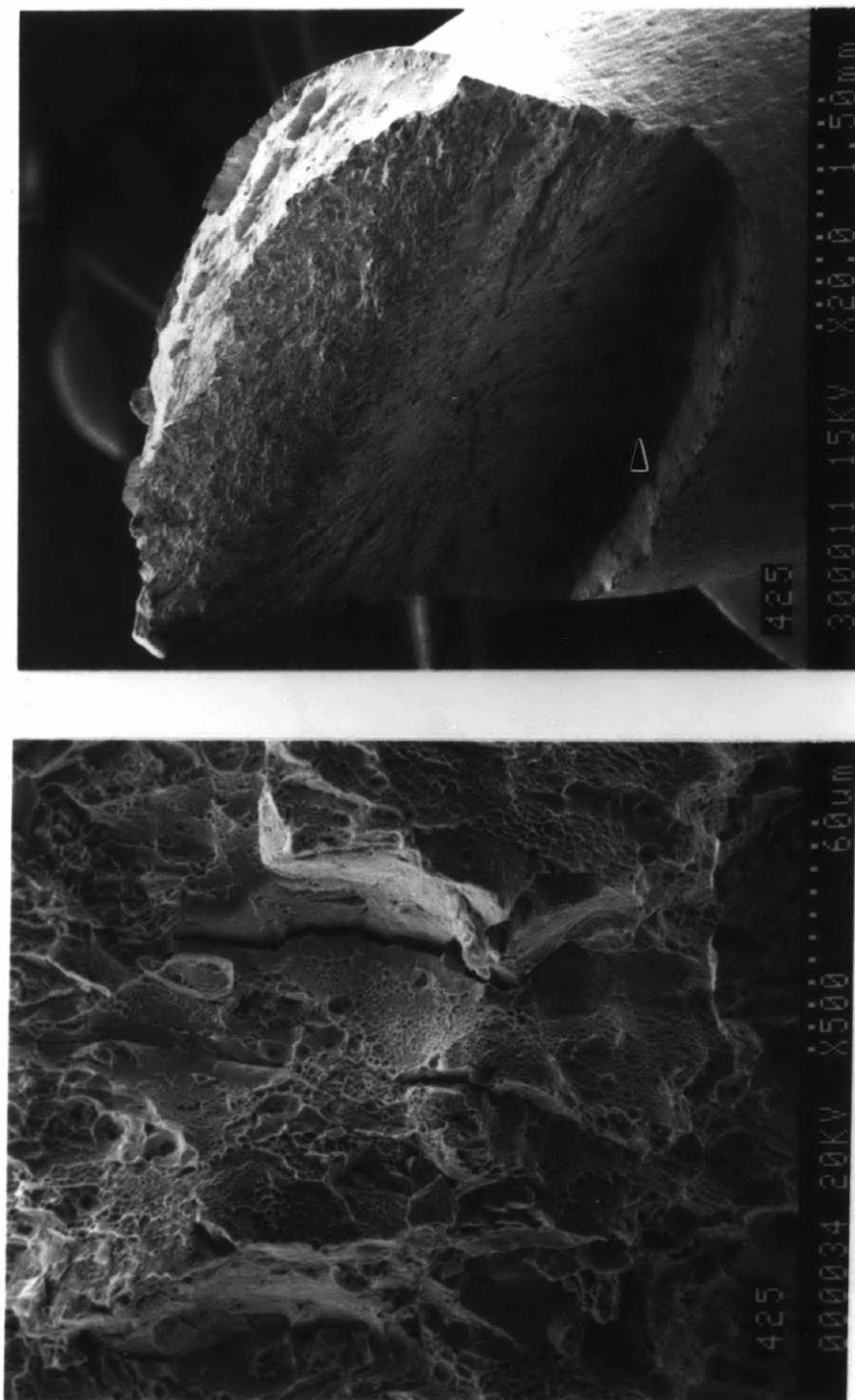
Figure 4.14 Tensile fracture surface of alloy 425. Arrow indicates area of high magnification.
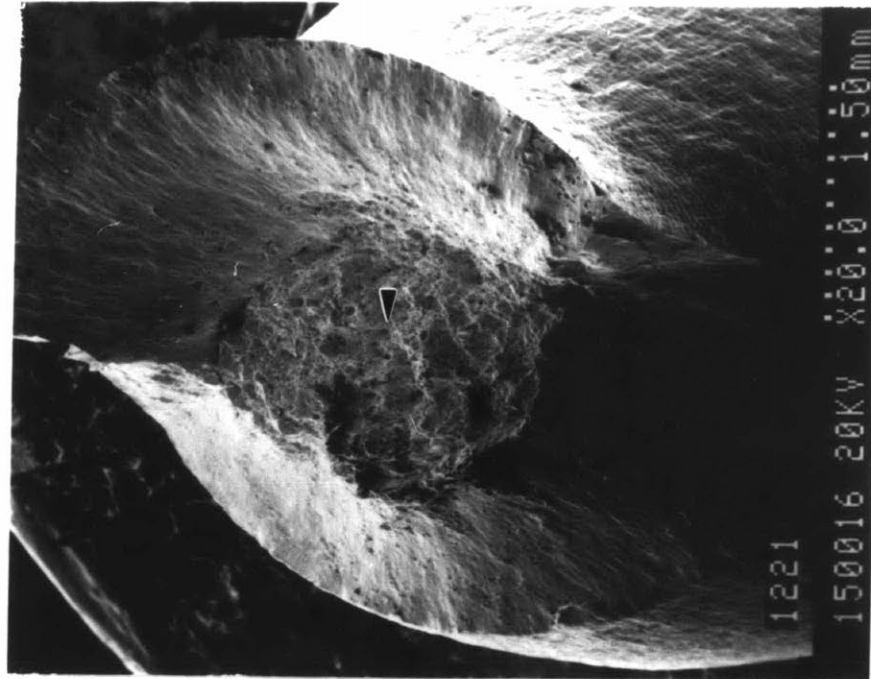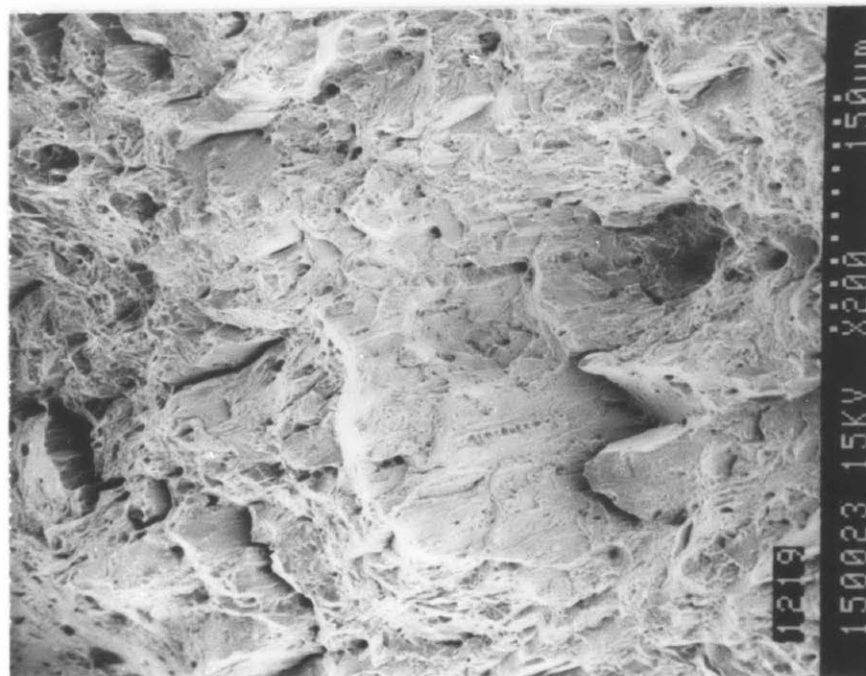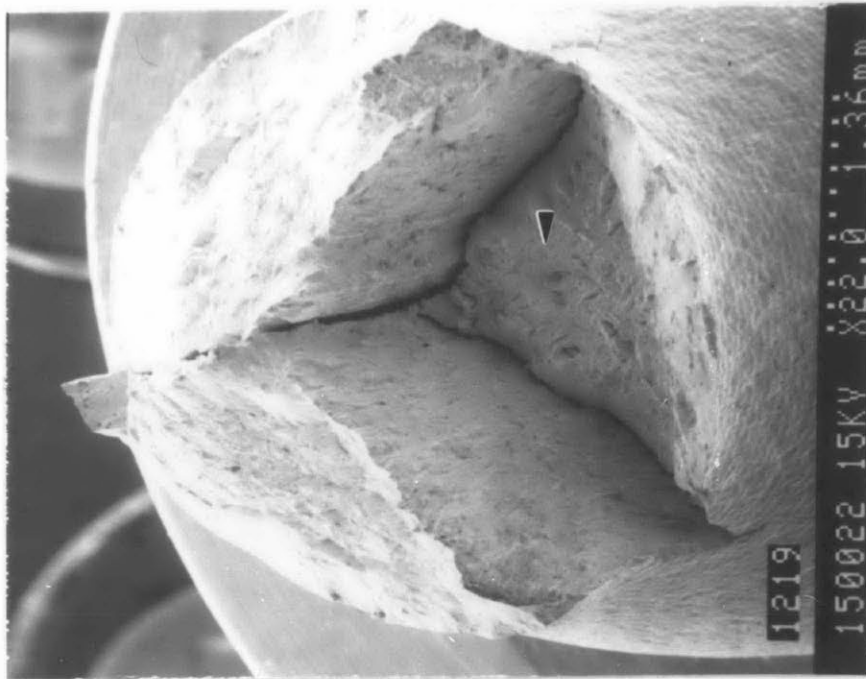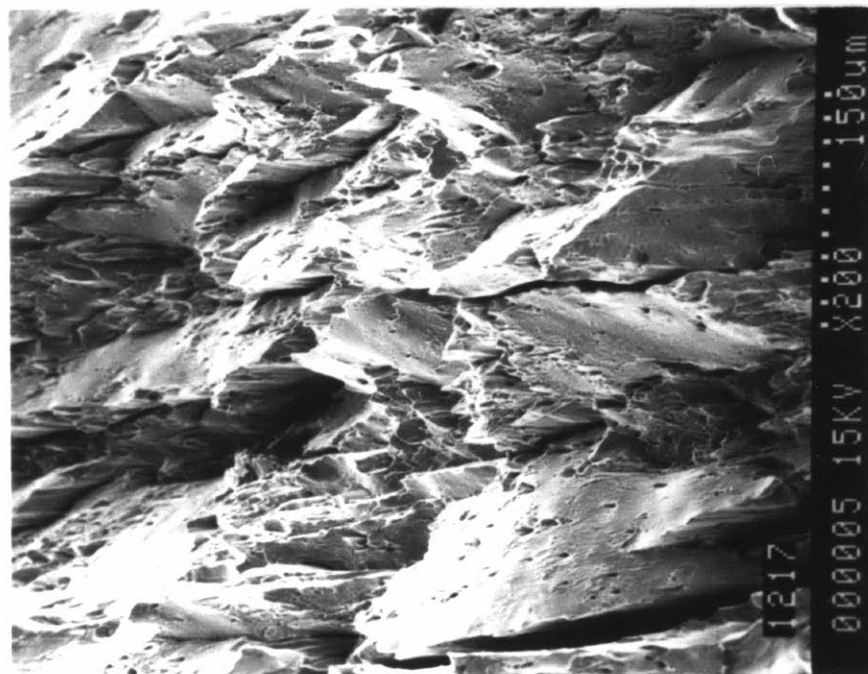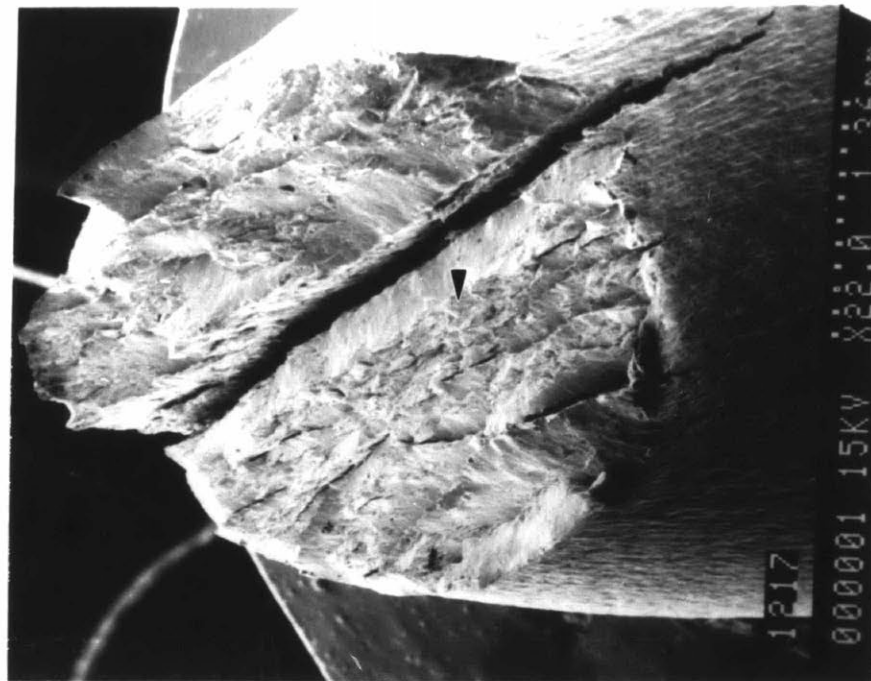
98

Figure 4.15 Tensile fracture surface of alloy 428.

Alloy 425 shows two shear lips in two different planes connected by a vertical fracture plane. There is a portion of quasicleavage failure at the bottom of the "V" as illustrated in Figure 4.14b.

The fracture appearance of alloy 428 is almost identical to that of alloy 425. Two shear lips in two different planes are connected by a vertical fracture plane. There is no region of fibrous fracture in alloy 428.

4.3 CORRELATION OF MECHANICAL BEHAVIOR WITH THERMODYNAMIC STABILITY

Calculations to determine the thermodynamic stability have to take into account precipitation processes since they alter the composition of the matrix. The main precipitation process to consider in the two series is the γ'-precipitation of $Ni_3(Ti,Al)$. Carbide and nitride formation also have to be considered, and it is expected that TiC and AlN will form. Since it is desired that titanium and aluminum contribute to γ'-precipitation, the carbon and nitrogen content was intentionally kept low to minimize the formation of TiC and AlN.

To calculate the matrix composition the following assumptions were made. All carbon forms TiC, all nitrogen forms AlN, and the remaining titanium is included in the γ'-precipitation. Atom Probe analysis confirmed that the γ'-precipitates were Ni_3Ti and no carbon or nitrogen were present in the austenite matrix. Figure 4.16 shows a field-ion micrograph of γ'-precipitates. The size of the γ'-precipitates are approximately 100Å in diameter. The matrix composition can thus be calculated, and the chemical driving force for the austenite to martensite transformation can be calculated using Eq. (3.1).

100
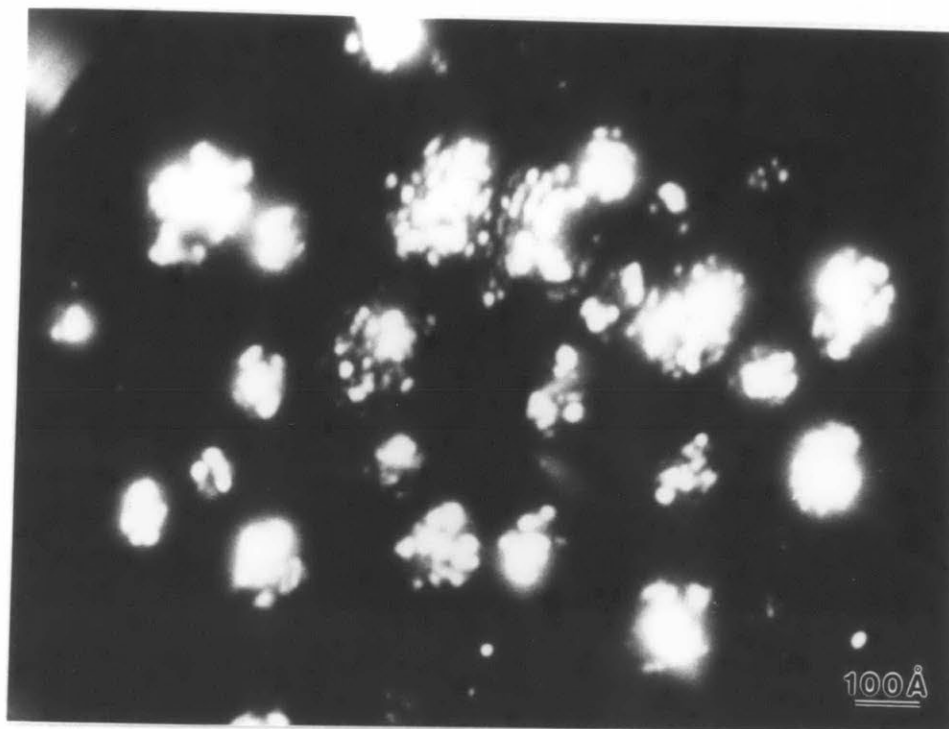
Figure 4.16 Field-ion micrograph of γ'-precipitates.

The J_{IC} data represented in Figure 4.6 shows maximum fracture toughness at 17% nickel for the 12% chromium series, and at 28% nickel for the 4% chromium series. The objective was to obtain maximum fracture toughness in the middle of each series, so the thermodynamical calculations outlined in chapter 3.1 are only accurate within ±3% nickel. In addition to uncertainty in matrix composition due to variations in degree of γ'-precipitation, the mechanical driving force calculation, ΔG^σ, could not previously be satisfactory accounted for. Based on model calculations of Olson et al.[21], Haezebrouck [60] has correlated the following expression for the mechanical driving force to data from Leal [1] and Young [2]:

$$\Delta G^\sigma = -0.718\overline{\sigma} - 6.85\frac{\Delta V}{V}\sigma_h + 185.4 \quad \text{(J/mole)} \tag{4.2}$$

where $\overline{\sigma}$ is the equivalent stress in MPa, σ_h is the hydrostatic stress in MPa, and $\Delta V/V$ is the volume change of the transformation. This expression is valid in the high yield stress limit (>1300 MPa), and takes into account the effect of stress triaxiality, thus accounting for the difference in stress state.

The critical driving force, ΔG^{crit}, for the austenite to martensite transformation can be calculated at the observed M_s^σ-temperatures if both the chemical and mechanical driving force contributions are known. Table 4.2 lists the critical driving force at M_s^σ(u.t) and M_s^σ(c.t) for some γ'-strengthened metastable austenitic steels. The first four alloys in Table 4.2 are from work by Leal [1], while the last two alloys are from the present work. As expected, the mechanical driving force is larger for the crack-tip case because of the higher triaxiality. The chemical driving force is lower for the crack-tip case since M_s^σ(c.t) is larger than M_s^σ(u.t). The critical driving force appears slightly larger for uniaxial tension*, which

---

* 31Ni-5Cr is not at M_s^σ(u.t).

ALLOY	M_s^σ(u.t) [°C]	$\frac{\Delta V}{V}$ [%]	σ_y [MPa]	G^σ(u.t) [J/mol]	ΔG^{ch}(u.t) [J/mol]	ΔG^{crit}(u.t) [J/mol]
31Ni-5Cr*	<-196	3.9	1497	-1289	<-2010	-3299
26Ni-4Cr*	<-120	4.5	1385	-1236	<-2966	-4202
31Ni*	-20<T<30	2.4	1200	-874	$-2248<\Delta G^{ch}<-1965$	$-3122<\Delta G^{crit}<-2839$
34Ni-9Co*	~30	2.52	1245	-924	-2135	-3059
4Cr Series	425(RT)	2.8	1413	-1101	-2271	-3372
12Cr Series						

ALLOY	M_s^σ(c.t) [°C]	$\frac{\Delta V}{V}$ [%]	σ_y [MPa]	G^σ(c.t) [J/mol]	ΔG^{ch}(c.t) [J/mol]	ΔG^{crit}(c.t) [J/mol]
31Ni-5Cr*	-196<T<-75	3.8	1370	-1569	$-2010<\Delta G^{ch}<-1758$	$-3579<\Delta G^{crit}<-3327$
26Ni-4Cr*	~55	4.1	1185	-1385	-2180	-3565
31Ni*	90<T<135	2.5	1145	-1061	$-1599<\Delta G^{ch}<-1316$	$-2660<\Delta G^{crit}<-2377$
34Ni-9Co*	~130	2.65	1236	-1187	-1432	-2619
4Cr Series	428(RT)	2.8	1407	-1408	-1894	-3302
12Cr Series	1217(RT)	2.3	1212	-1098	-2575	-3673

* Data from Leal [1]

Table 4.2 Critical driving force at M_s^σ(u.t), and M_s^σ(c.t) for some γ'-strengthened metastable austenitic steels.

may be associated with a weak temperature dependence of ΔG^{crit}. Within observed scatter, ΔG^{crit} was taken to be temperature independent.

The only variation in the two alloy series are the variations in iron, nickel, and chromium content. Therefore, one can visualize this as an iron-nickel austenite with chromium added as solid-solution strengthener. The main difference between the two series is therefore the contribution from solid-solution strengthening due to different chromium content. Based on models of martensitic transformation kinetics [61], analysis of ΔG^{crit} must incorporate the effect of chromium as a solid-solution strengthener.

Solid-solution strengthening has recently been reviewed by Nabarro.[62]. The solid solution strengthening is found to be proportional to $c^{1/2}$, the Fleischer model, or to $c^{2/3}$, the Labusch model, where c is the concentration of the solute. The Fleischer model is only appropriate for dilute solutions, typically c<2%, while the Labusch model can be used over a wider range of solute concentration. Labusch arrived at the following expression for solid solution strengthening [63]:

$$\tau_c b = \frac{c^{2/3} f_0^{4/3} w^{1/3}}{(4T)^{1/3}} C \qquad (4.3)$$

where τ_c is the critical shear stress, b is the Burgers vector, f_0 is the maximum interaction force of a single obstacle, w is the range of interaction between solute atoms and dislocations, T is the dislocation line tension, and C is a constant. Since the chromium content in this work is 4% and 12%, the solid-solution strengthening of chromium is expected to be proportional to $c^{2/3}$ in the two series.

The main difference between the two alloy series is the chromium content. In order to compare the two alloy series, the effect of the difference in chromium content has to be accounted for. A $c^{2/3}$ dependence on the solid-solution strengthening is expected and it is

proposed that a $c^{2/3}$ dependence also applies to the critical driving force. Figure 4.17 is in agreement with this proposition, illustrating a linear relationship between the critical driving force and $(X_{Cr})^{2/3}$ for the γ'-strengthened metastable austenitic steels displayed in Table 4.2. Only M_s^σ-temperatures ranging from -100°C to 100°C have been considered to limit the potential role of a temperature dependence of ΔG^{crit} through thermal activation.

The linear relationship between the critical driving force and $(X_{Cr})^{2/3}$ can be used to eliminate the effect of chromium on the chemical driving force. This is illustrated in Figures 4.18 to 4.20, where the tensile strength, true strain, and J_{IC} fracture toughness for both alloy series are plotted versus the difference between the total driving force and the critical driving force at M_s^σ. A free energy difference of zero corresponds to M_s^σ, and a positive difference corresponds to above M_s^σ. This way of representing the data becomes equivalent to plotting versus the normalized temperature parameter θ, as illustrated in Figures 2.9 and 2.10, or against temperature as illustrated in Figure 2.1.

The lower temperature-sensitivity expected with the addition of chromium is illustrated in Figure 4.21, where the the enhancement in fracture toughness ΔJ_{IC} is plotted versus the difference between the total driving force and the critical driving force at M_s^σ. The enhancement in fracture toughness, i.e. $\Delta J_{IC} > 0$, is spread over a wider free-energy range for the two alloy series investigated in this thesis. Furthermore, the entropy change at room temperature, calculated from equation 3.2, is smallest for the 12% chromium series. These two results indicate that the temperature sensitivity is lower with the addition of chromium.
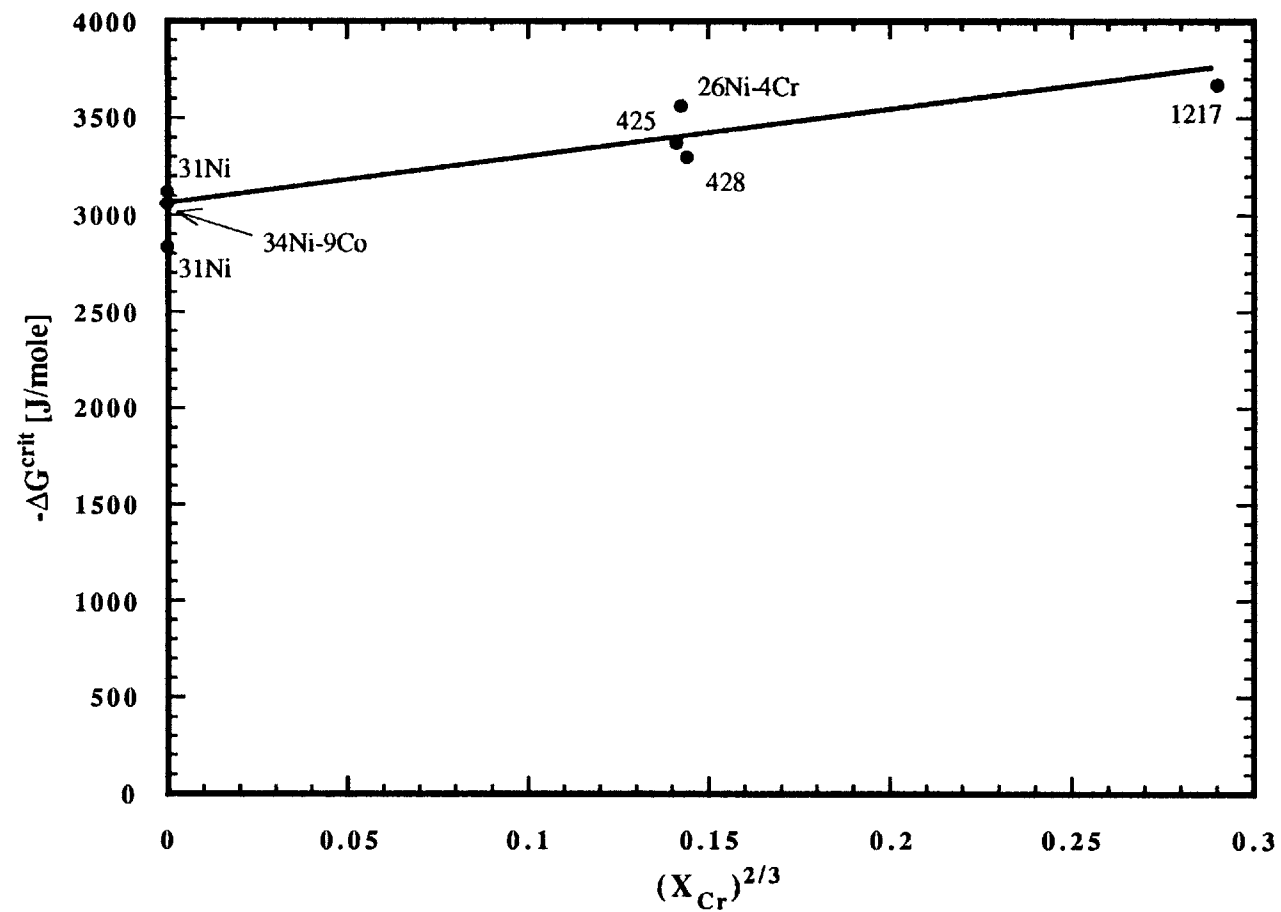
Figure 4.17 Critical driving force of the transformation in uniaxial tension, and for the crack-tip case, as a function of chromium content.
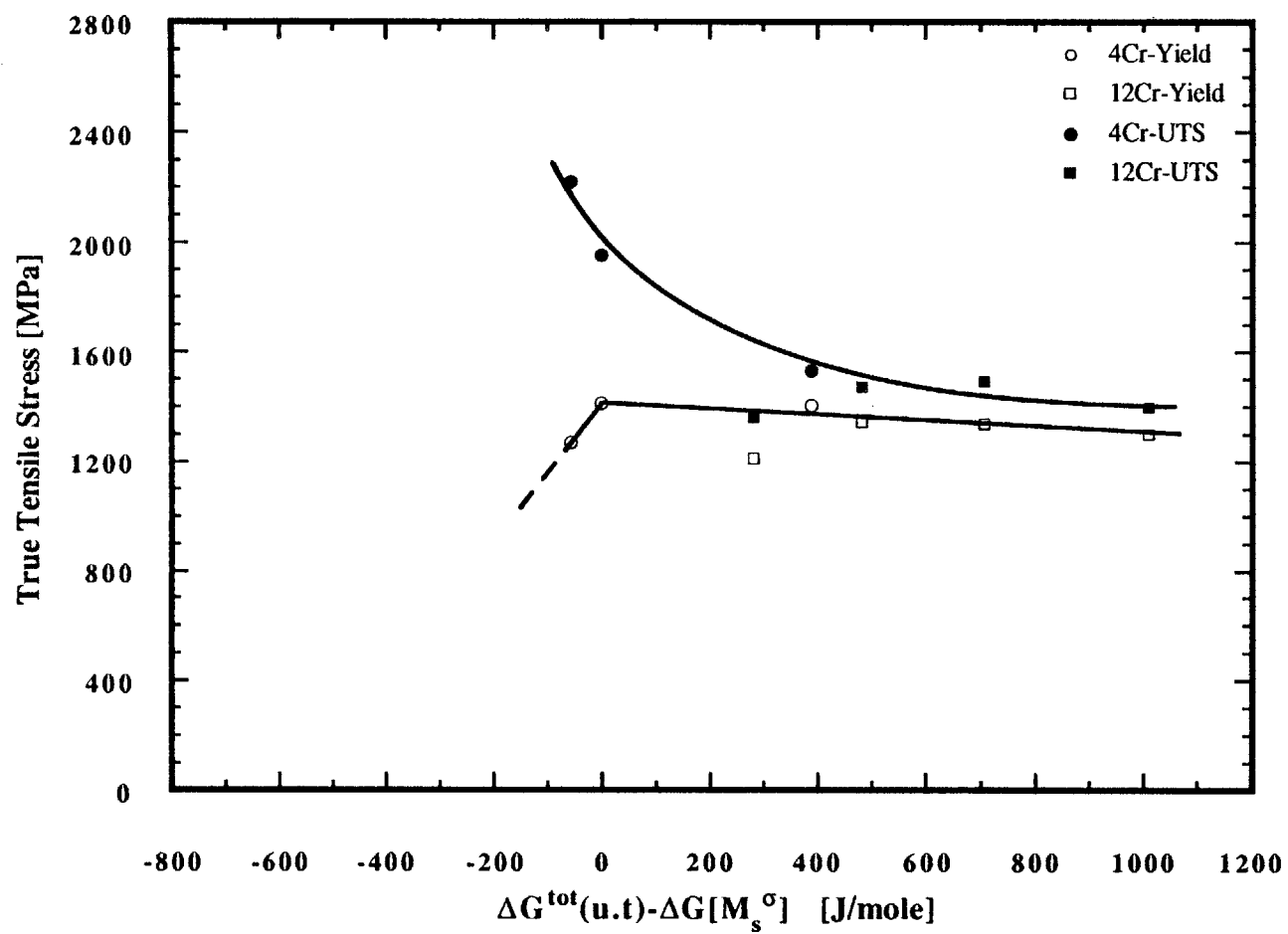
Figure 4.18 True yield stress and true ultimate tensile stress as a function of free energy.
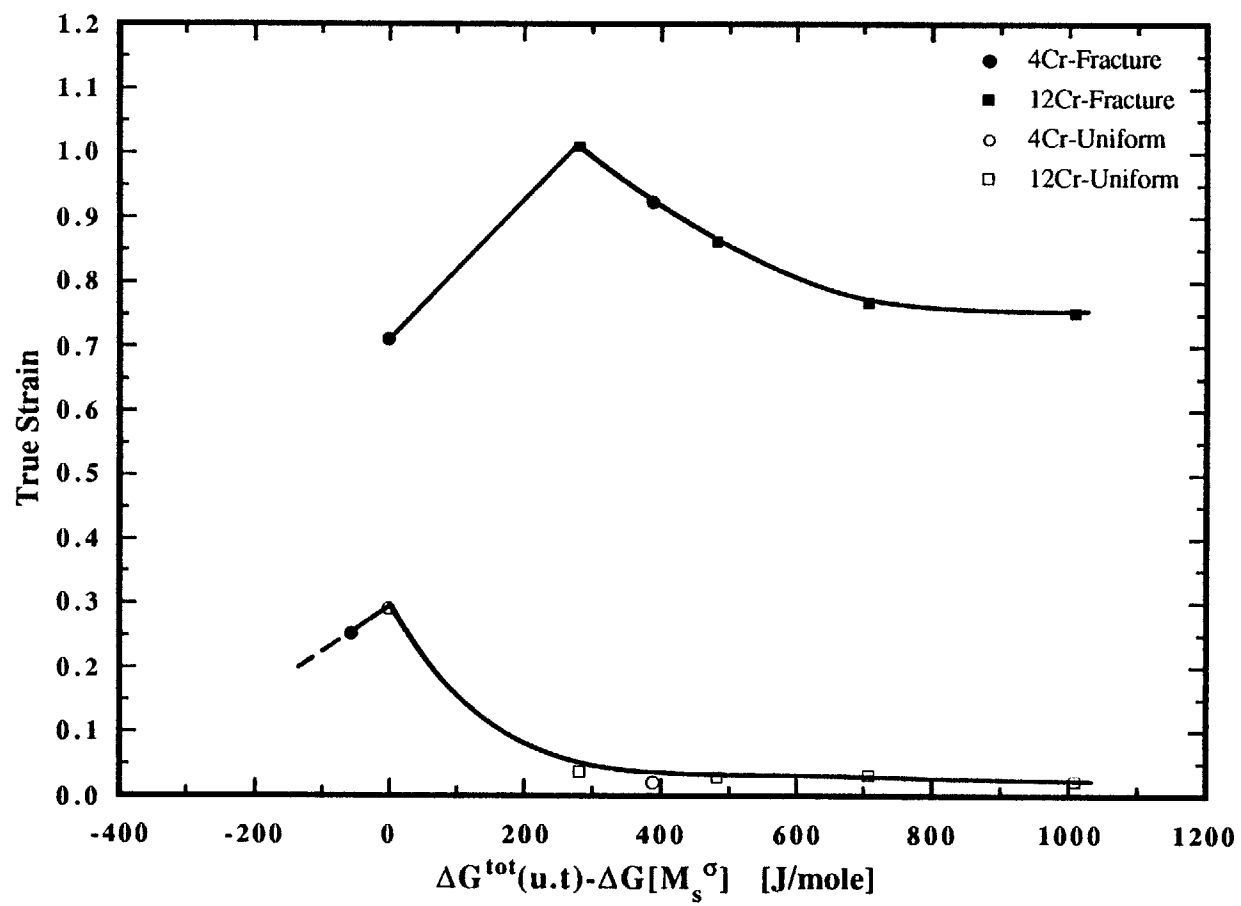
Figure 4.19 Uniform strain and strain to failure as a function of free energy.
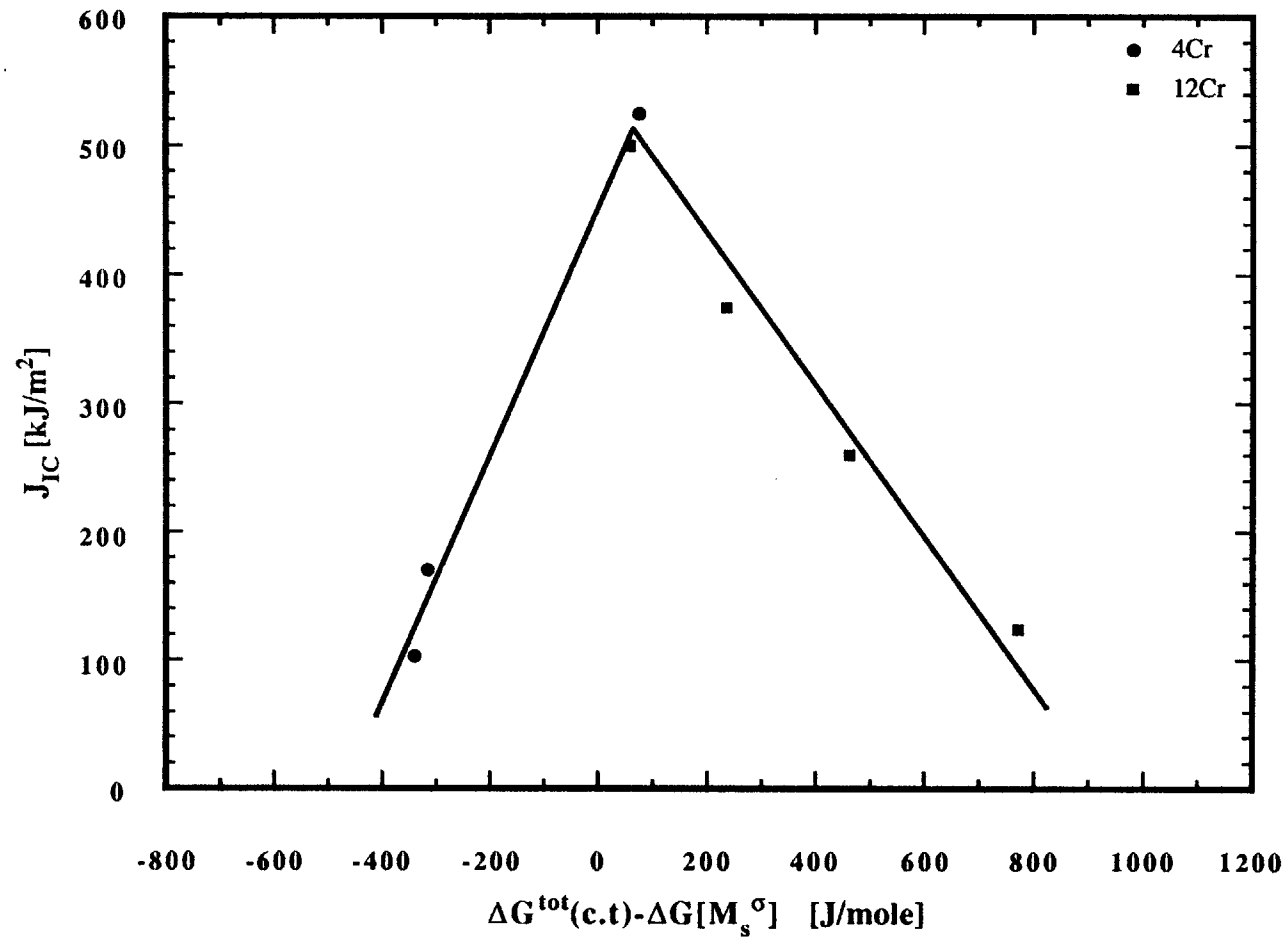
Figure 4.20 J_{IC} fracture toughness as a function of free energy.

Figure 4.21 ΔJ_{IC} fracture toughness enhancement as a function of free energy.

4.4 METALLOGRAPHIC OBSERVATIONS OF LOCALIZATION AND FRACTURE BEHAVIOR

In order to assess the mechanistic basis of the large fracture toughness enhancement during the mechanically-induced phase transformation, detailed metallographic observations of the crack tip were conducted. A natural starting point in this section is therefore the localization behavior of the stable austenite control material , i.e alloy 1223 tested at elevated temperature. The influence of the mechanically-induced p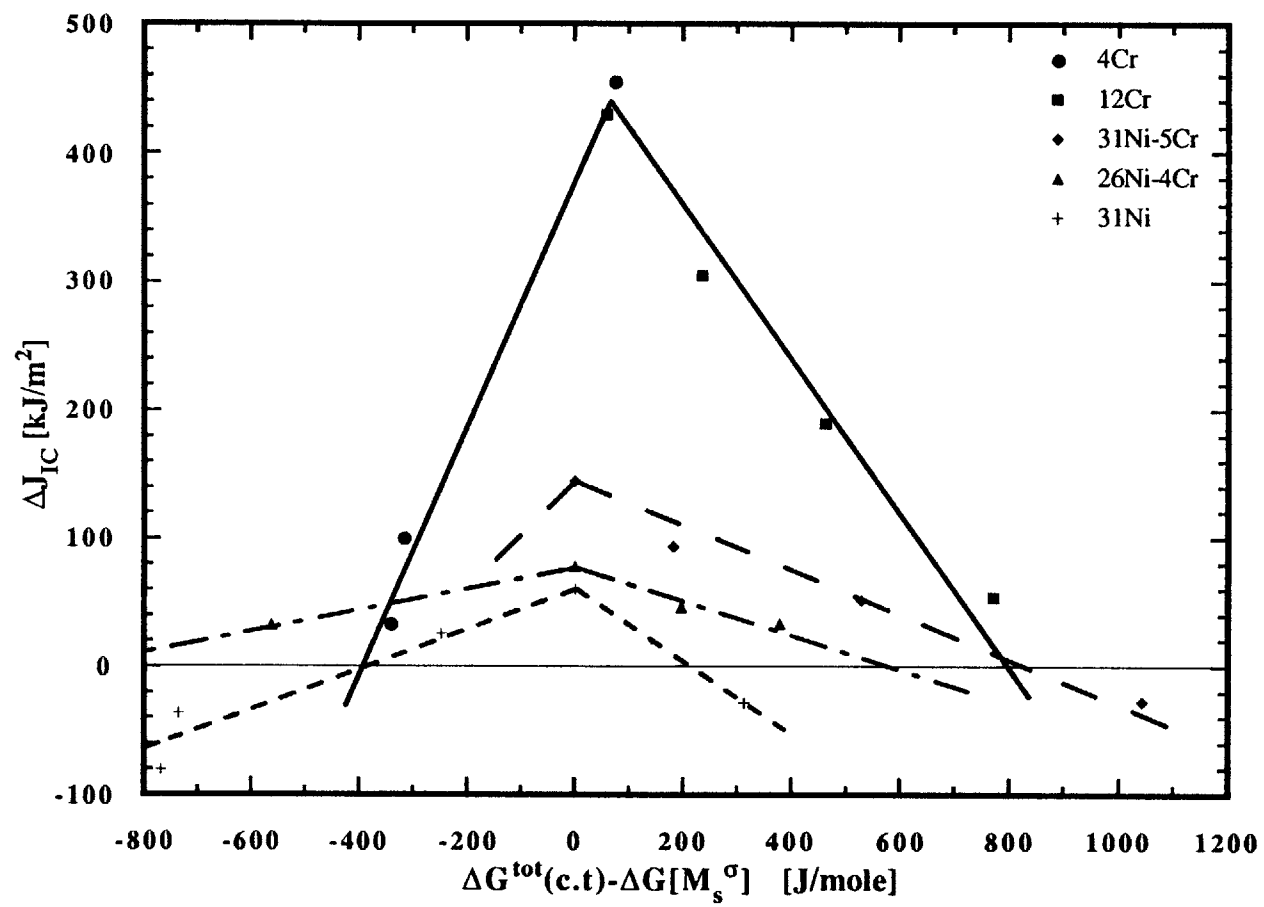hase transformation on the fracture process can then be addressed. This discussion will be divided into two parts, addressing the stress-assisted and strain-induced martensitic transformation separately.

Figure 4.22 shows the crack tip of alloy 1223 after completion of the fracture toughness test at elevated temperature. The arrows mark the end of fatigue pre-cracking. The pre-cracked region always exhibits an irregular zig-zag pattern in all tested alloys. The crack advance during monotonic loading in the fracture toughness test initiates with a curved mixed-mode path, but overall, a flat fracture mode is observed. Taking the crack tip opening displacement (CTOD) as [51]:

$$CTOD \approx \frac{1}{2}\frac{J}{\sigma_y}$$
(4.4)

we obtain CTOD=25μm. This is in good agreement with the observed degree of blunting in Figure 4.22.

4.4.1 T<M_s^σ(c.t)

Only alloys 424 and 425 were below M_s^σ(c.t) when tested at room temperature, and they both exhibit similar localization behavior. The fracture toughness difference is small: 102 kJ/m^2 for alloy 424, and 170 kJ/m^2 for alloy 425. Figures 4.23 and 4.24 show the
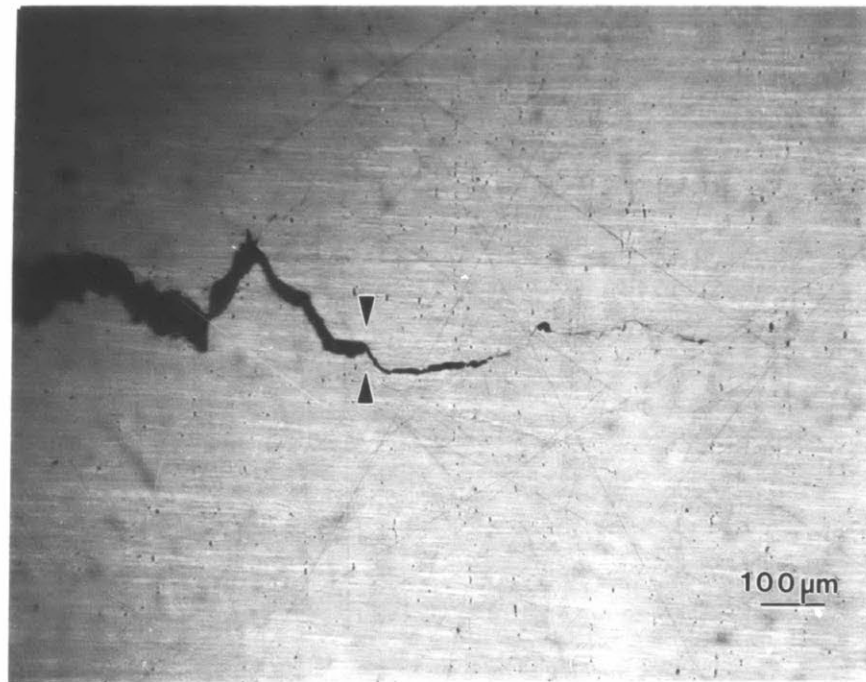
Figure 4.22 Crack tip micrograph of alloy 1223 tested at elevated temperature.

crack-tip metallography of the two alloys after completion of the single-specimen J-integral test. Since pre-cracking was conducted at elevated temperature, the onset of martensite formation corresponds to the actual crack length at the start of the fracture toughness test.

The martensite zone surrounding the crack can be divided into two regions: an inner zone consisting of 100% martensite, and an outer zone, which extends out to the last visible martensite plate. The height of the inner zone is approximately constant throughout the crack-propagation process, while the outer zone increases in size moving towards the crack tip. The latter is to be expected, since, as the crack is propagating, the stress intensity increases, and thus the mechanical driving force contribution, extending the distance within which martensite can nucleate outwards.

The crack opening displacement is larger in alloy 425 since this alloy has been subjected to a larger final stress intensity. It is interesting to note though, that the transformation zone height is larger in alloy 424 although subjected to a lower stress intensity. This is because of the difference in chemical stability between the two alloys; the total driving force for alloy 424 is larger than for alloy 425, thus martensite will form further away from the crack.

Another interesting feature to note is the forked or fan-like extension of martensite out in front of the crack tip. This is quite different from the smooth, nearly circular zone predicted by simple models of stress-assisted transformation. This feature is presumably related to the plastic zone of the specimen. This zone rotates forward as the test progresses. The localized deformation locally gives a high mechanical driving force which triggers the transformation.

The micrographs in Figures 4.23 and 4.24 do not reveal very clear information about the early onset of localization. An observation that can be made regarding the early stages is the apparent asymmetry in the inner transformation zone height. Alloy 424
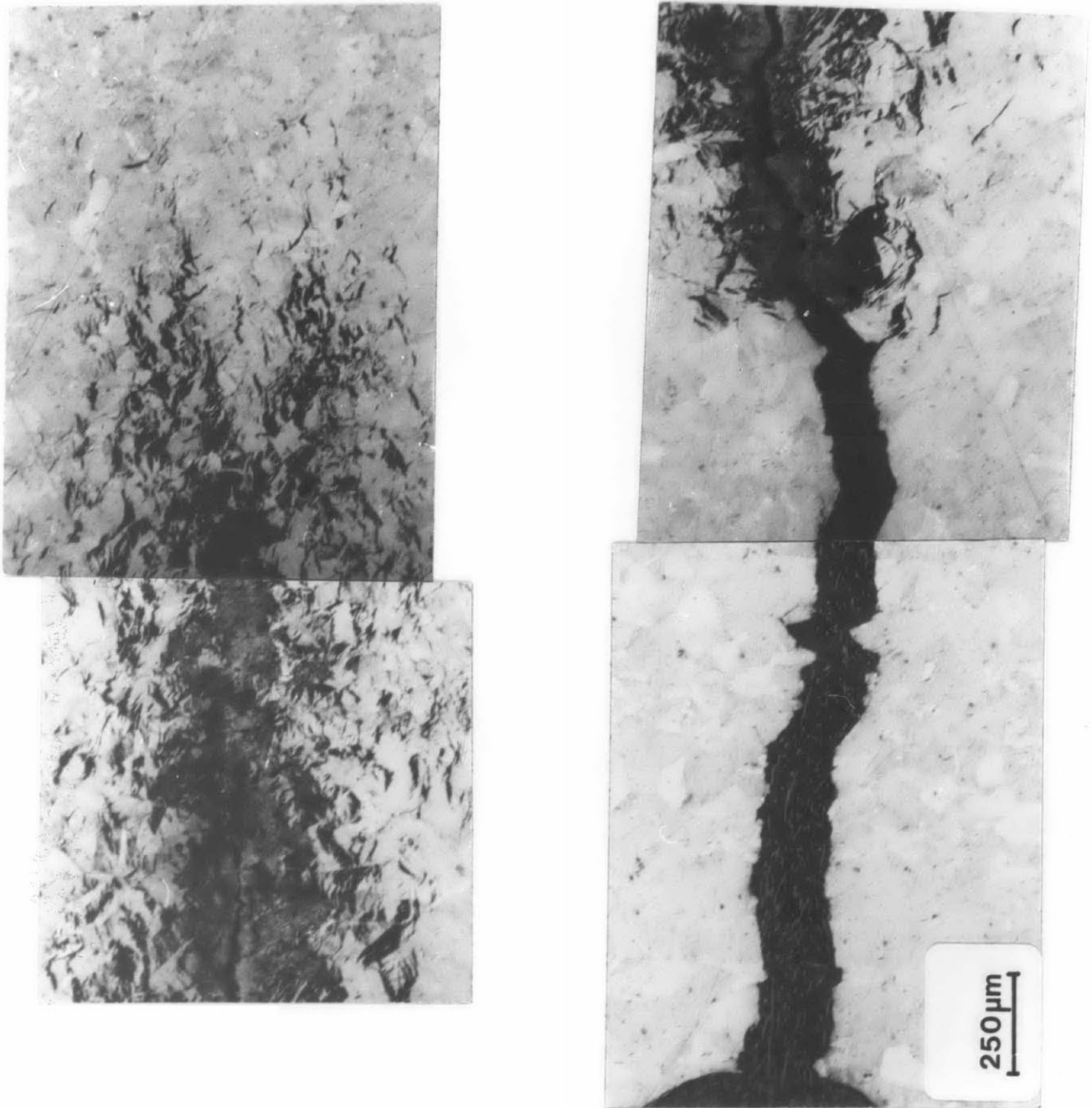
113

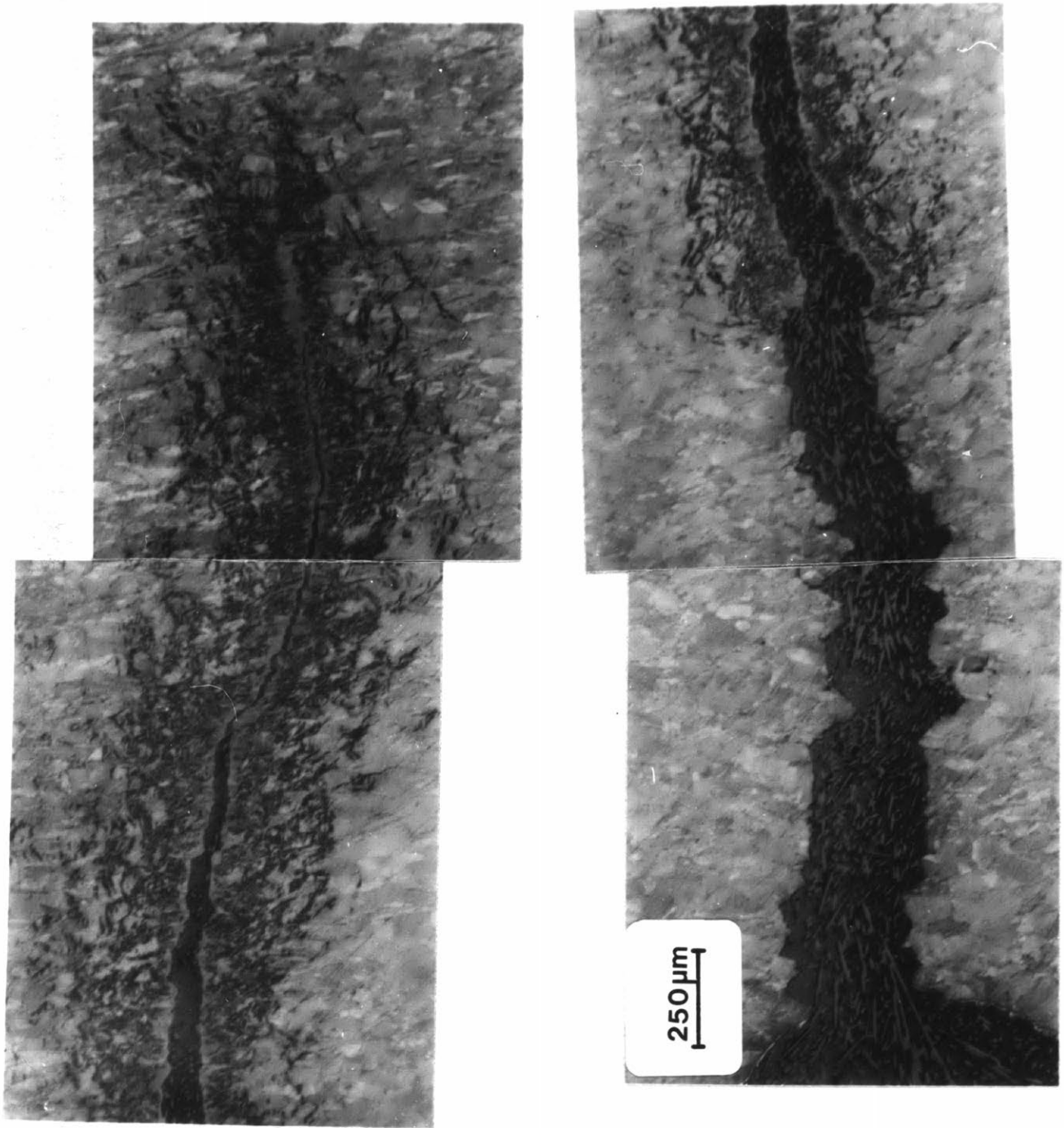**Figure 4.23** Crack tip micrograph of alloy 424.

114

Figure 4.24 Crack tip micrograph of alloy 425.

initially exhibits a "zig" upwards, and the transformation zone height is much larger on the lower side of the crack. Therefore, the overall transformation zone height is larger during the initial stages of localization. The exact mirror image is observed in alloy 425. This asymmetry can be explained with the help of Figures 4.25 and 4.26.

Figure 4.25 shows alloy 424 loaded to approximately 50% and 100% of J_{IC}. 50% of J_{IC} corresponds to the baseline value of alloy 1223 tested at elevated temperature. These load levels correspond to a CTOD of 20μm and 40μm, and this is in good agreement with observations in Figure 4.25. As can be seen in Figure 4.25a, the martensite is already present at 50% J_{IC}. The martensite is not very localized at this time, but rather spread out in a fan-like manner making approximately a 45 degree angle with the crack-propagation direction. At 100% J_{IC}, the inner complete transformation zone has developed, and the outer zone extends out to many times the crack opening displacement. Also, the formation of the inner zone seems to have moved transformation to a higher angle of approximately 60 degrees.

In Figure 4.26 the fracture surface of alloy 424 is presented. Crack propagation is in the direction of the large arrows. The small arrows indicate the end of the fatigue crack zone to the left, and the beginning of the monotonic loading zone to the right. The very surprising and important feature displayed here is the groove extending from top to bottom, dividing the fatigue crack zone and the monotonic loading zone. This groove, arising from crack tip branching, plays an important role in the localization behavior and the development of the asymmetry of the transformation zone.
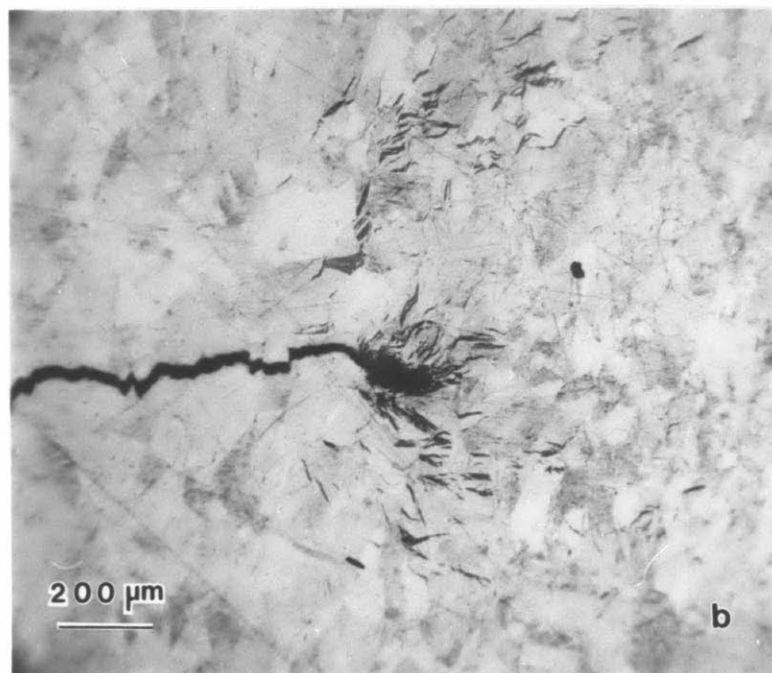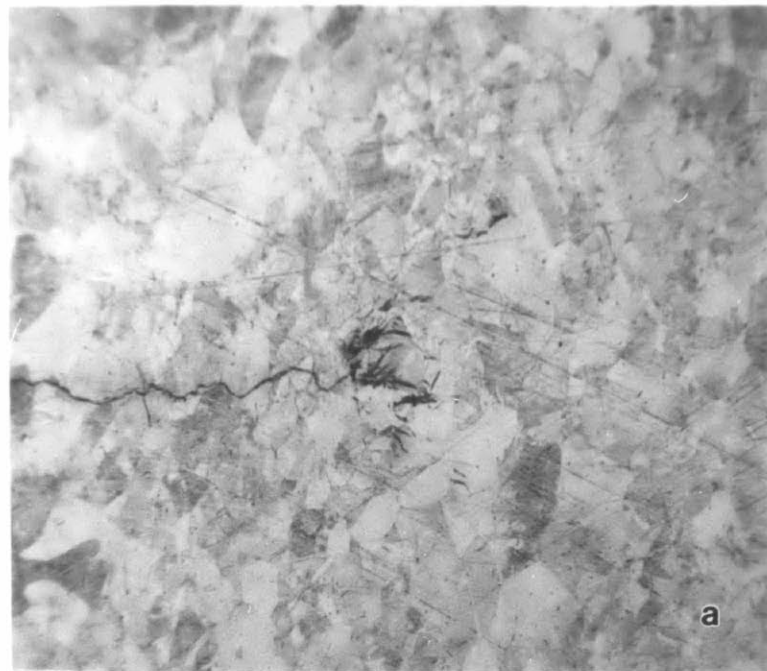
116

Figure 4.25 Crack tip micrograph of alloy 424 loaded to a) 50% J_{IC}, and b) 100% J_{IC}.
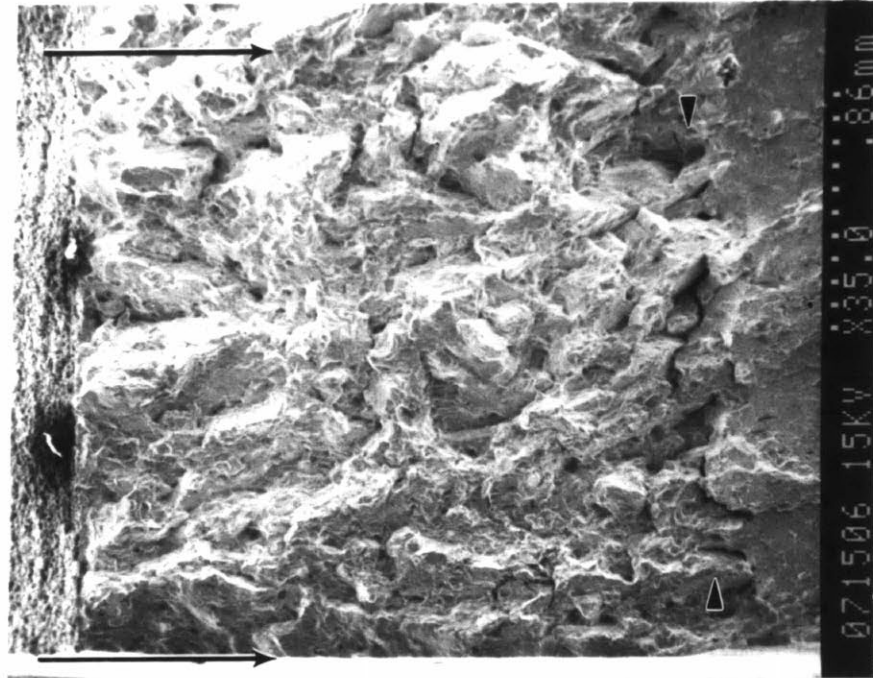
Figure 4.26 Fracture surface of fracture toughness specimen of alloy 424.

4.4.2 T>M$_s^\sigma$(c,t)

The 12% chromium series and alloy 428 are above M$_s^\sigma$(c,t) when tested at room temperature, and they all display similar localization behavior. In many instances, they also behave similarly to what was previously observed and discussed for alloys 424 and 425.

Figure 4.27 shows alloy 1217 after completion of a single-specimen J-integral test. The most noticeable feature not previously observed is the stronger crack branching phenomenon. Two cracks have been trying to propagate, and the lower crack finally propagated. Note the connection of fine strain-induced martensite between the two cracks. This indicates that at one point during the test, there was symmetry between the two cracks, and localization was symmetrically focused in front of the two cracks. The crack branching is related to the previously observed groove in the fractograph of alloy 424. This groove is observed in the fractographs of all seven alloys. The width of the groove is related to the J$_{IC}$-level, and is therefore largest for alloys 428 and 1217.

Figure 4.28 illustrates the difference in load levels for alloy 1217 loaded to 30%, 60%, and 100% of J$_{IC}$. This corresponds to nominal CTOD's of 60, 120, and 200μm which is approximately a factor of two over the observed crack opening. The observed zig-zag of the lath martensite in front of the fatigue crack tip (marked with arrows), is located within the fatigue pre-cracking plastic zone size (r$_y$=280μm). It has formed in a region which has localized during the pre-cracking, and therefore also has been highly strained during the pre-cracking operation. The symmetrical arrow-like martensite zone observed in Figure 4.28b emanates from two crack tips. Since some branching occured during pre-cracking, these two cracks are most likely not due to the same phenomenon responsible for the observed fracture surface groove because of the relatively large distance between them. Figure 4.28c shows an almost square blunted crack tip, with one small crack emanating from the upper corner, and an almost insignificant crack protruding from
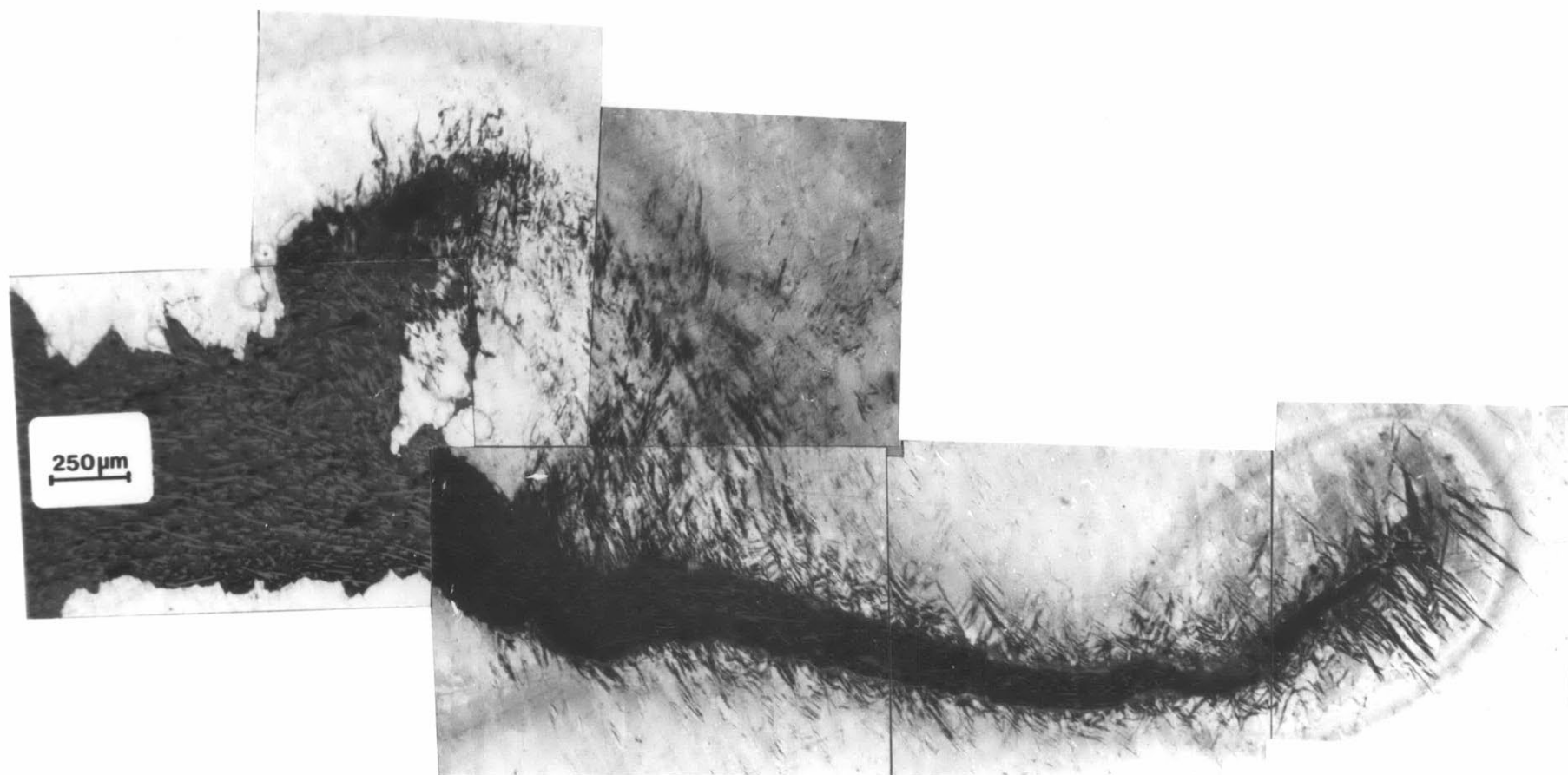
250 μm

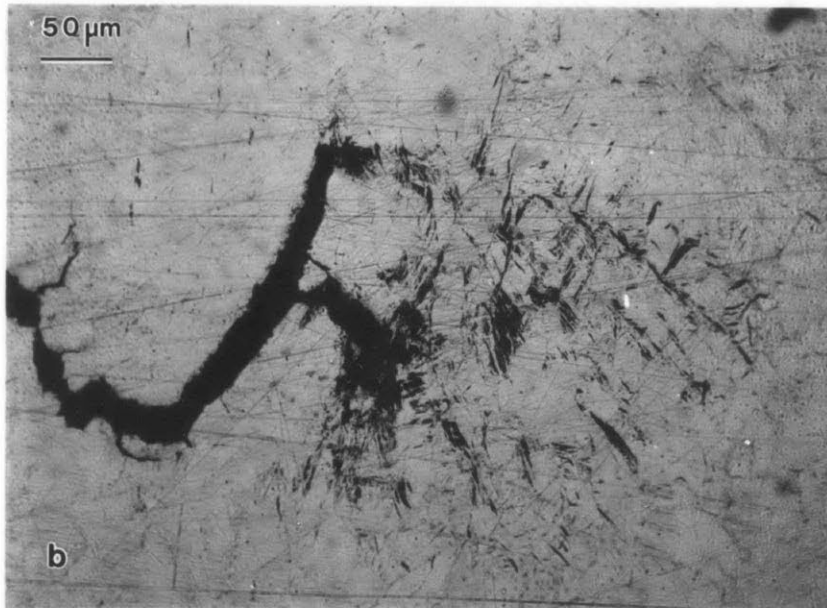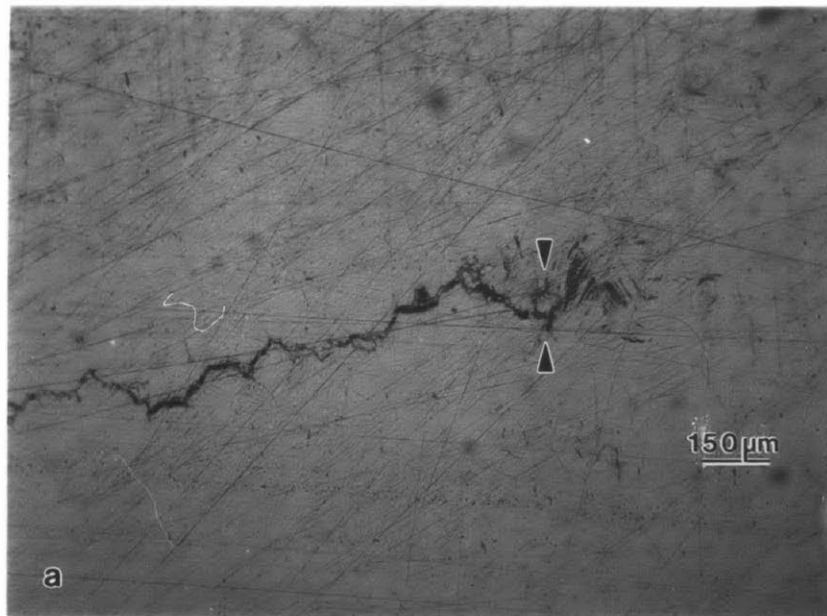**Figure 4.27** Crack tip micrograph of alloy 1217.

Figure 4.28 Crack tip micrograph of alloy 1217 loaded to a) 30% J_{IC}, b) 60% J_{IC}, and c) 100% J_{IC}.

the lower corner. The zone straight ahead of the blunted crack is highly transformed to martensite.

Figure 4.29 illustrates the large amount of deformation possible when transformation plasticity is utilized. The amount of bending of the specimen is quite remarkable considering the yield strength is 1200 MPa.

The mechanism responsible for fracture toughness enhancement appears to be essentially the same for both stress-assisted and strain-induced transformation as schematically illustrated in Figure 4.30. Mechanically-induced martensite is initially formed in front of the crack tip. The associated high strain hardening in this region apparently forces strain localization elsewhere, promoting crack branching and square blunting. Above $M_s^\sigma(c.t)$, continued straining initiates shear fracture in the upper and lower corners of the blunted crack. Continued crack opening then occurs by shearing along a high angle of approximately 75 degrees, until the COD becomes so large that the crack can circumvent the transformed region ahead of the blunted crack. This point corresponds to maximum applied load and J_{IC}. Similar features occur below $M_s^\sigma(c.t)$, but toughening is apparently less effective when the fracture path can follow the more brittle fully transformed zone.

4.5 COMPARISON WITH MODEL PREDICTIONS

The kinetic model for strain-induced martensite developed by Olson and Cohen [17], and described in section 2.1.1.3, does not take into account the effect of the stress-state sensitivity of the transformation kinetics. More martensite is formed during the high triaxiality present during necking in uniaxial tension than predicted by the model. Recently Stringfellow et al. [64] have developed a new refined kinetic model incorporating the effect
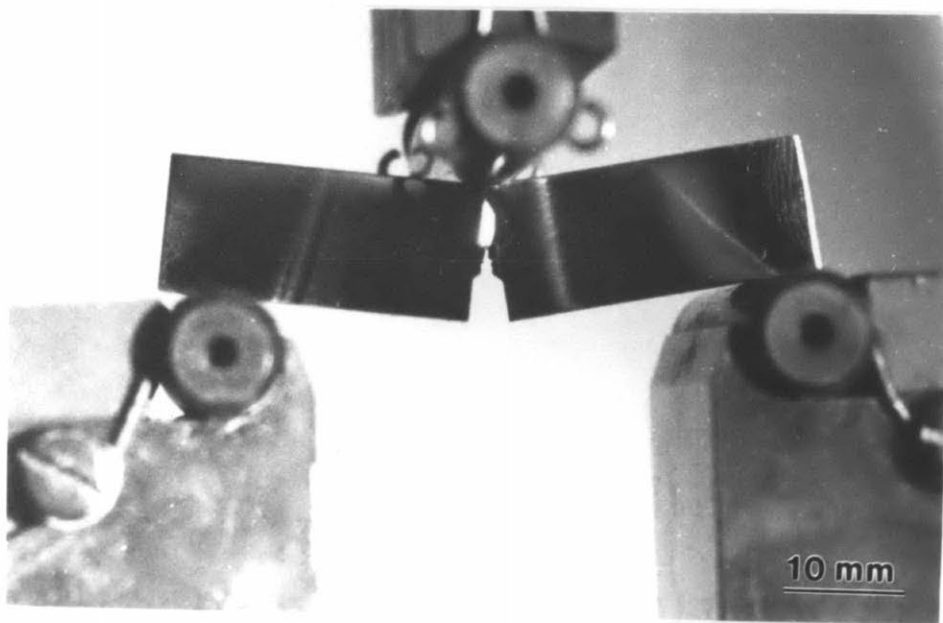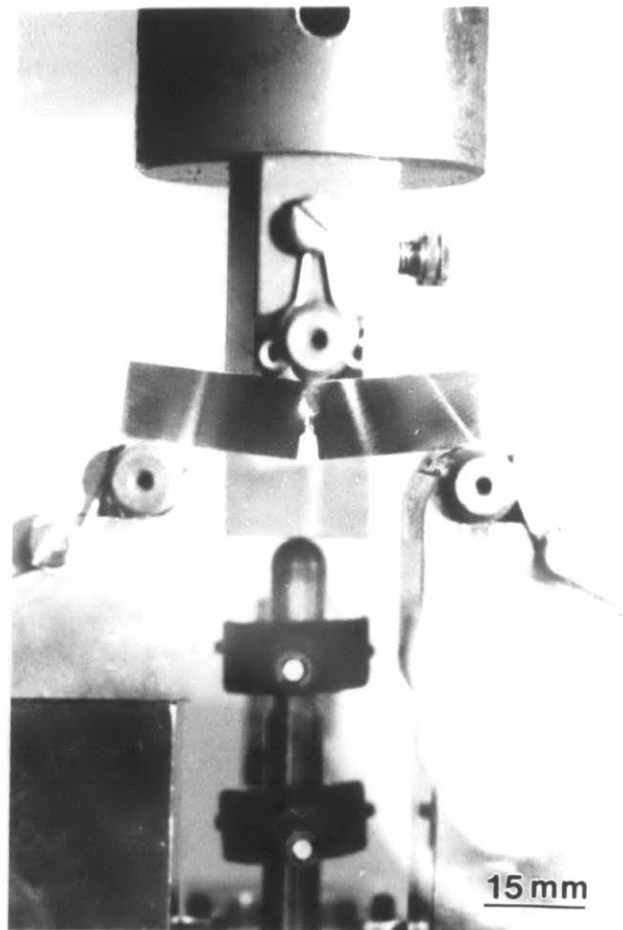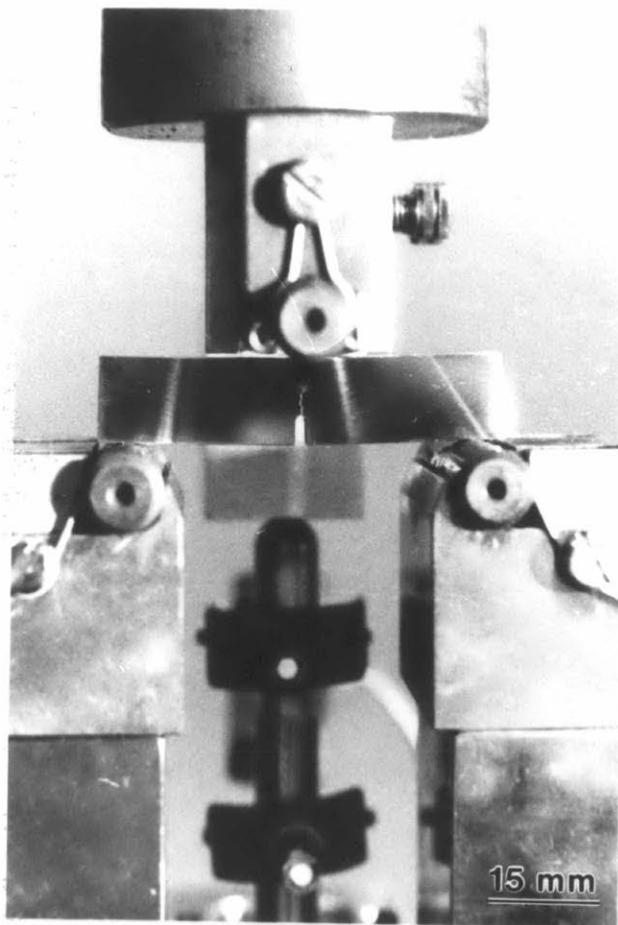
Figure 4.29 Deformation of alloy 1217 during fracture test.

123
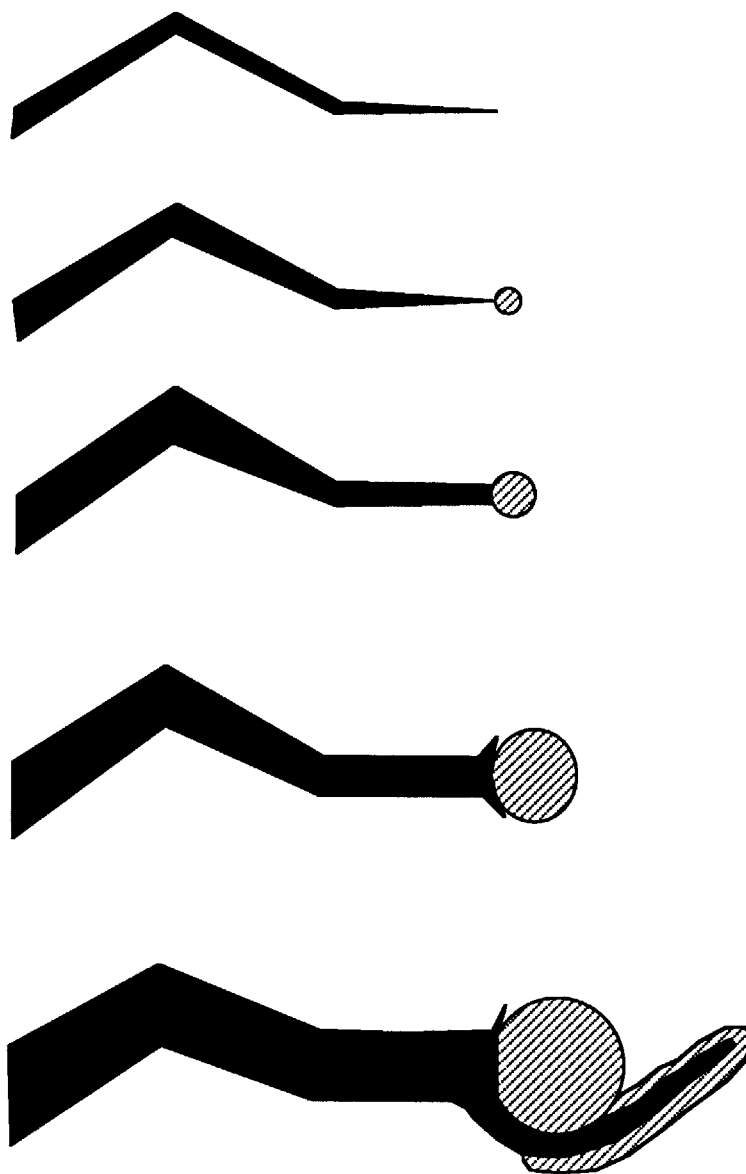
Figure 4.30 Schematic of observed toughening mechanisms.

124

of stress-state sensitivity. They incorporate the stress-state sensitivity into the probability function p in Eq. (2.8) so that p is a function of both temperature and stress state:

$$p = 1 - \frac{1}{\sqrt{2\pi}} \int_{-\infty}^{z} \exp\left[-\frac{1}{2}\left(\frac{x-\bar{x}}{s_x}\right)^2\right] dx \qquad (4.6)$$

where $\bar{x}$ is the dimensionless mean of a given probability function and s_x is its standard deviation. The stress-state dependance of p is through the driving force parameter x, where x is defined as:

$$x = x_0 + x_1\gamma + x_2\Sigma \qquad (4.7)$$

where x_0, x_1, and x_2 are dimensionless constants, γ is a normalized temperature:

$$\gamma = \frac{T}{M_s^\sigma(u.t)} \qquad (4.8)$$

and Σ represents a ratio of the volumetric and deviatoric stress invariants

$$\Sigma = \frac{-p}{\bar{\sigma}} \qquad (4.9)$$

where p is pressure and $\bar{\sigma}$ is the von Mises stress. Both are derived as scalar invariants of the Cauchy stress tensor.

Combining Eq. (4.7-9) we obtain:

$$x = x_0 + x_1\frac{T}{M_s^\sigma(u.t)} + x_2\frac{-p}{\bar{\sigma}} \qquad (4.10)$$

x increases with increasing T, thus decreasing p, but x decreases with increasing triaxiality, thus increasing the probability for martensite nucleation. This is in agreement with

experimental observations [2,8] that positive triaxiality promotes nucleation, while pressure inhibits nucleation.

Stringfellow et al. compared their model to experiments by Young [2] in both uniaxial compression and uniaxial tension. These results are shown in Figure 4.31 and good agreement was obtained for both compression and tension.

The stress-strain behavior for strain-induced martensitic transformation has been developed by Narutani et al. [22]. They assumed equal strain in both austenite and martensite. This leads to an overestimate of the actual stress-strain behavior. They corrected this by subtracting the effect of transformation strain, since the transformation strain does not contribute to strain hardening of either phase. Recently Stringfellow and Parks [65] developed an isotropic viscoplastic, self-consistent model for the evaluation of the one-dimensional stress-strain behavior of a multiphase material. They showed that if the hardness difference between two phases is large, the assumption of equal strain, leads to inaccurate predictions. By partitioning the strain such that the softer phase receives a larger strain, a better estimate of the actual stress-strain behavior is obtained, as illustrated in Figure 4.32. By expanding this new model to incorporate the effect of transformation strain, the following expression for TRIP-steels has been developed by Stringfellow et al. [64]:

$$\overline{D} = f D_m + (1-f) D_a + D_{nucl} \qquad (4.11)$$

where D is the plastic strain rate, subscripts m and a refer to martensite and austenite, the bar refers to the composite material, f is the volume fraction martensite, and D_{nucl} is a nucleation strain rate which corresponds to the transformation shape strain:

$$D_{nucl} = \dot{f} \left(A \overline{N} + \frac{1}{3} \Delta V 1 \right) \qquad (4.12)$$

126
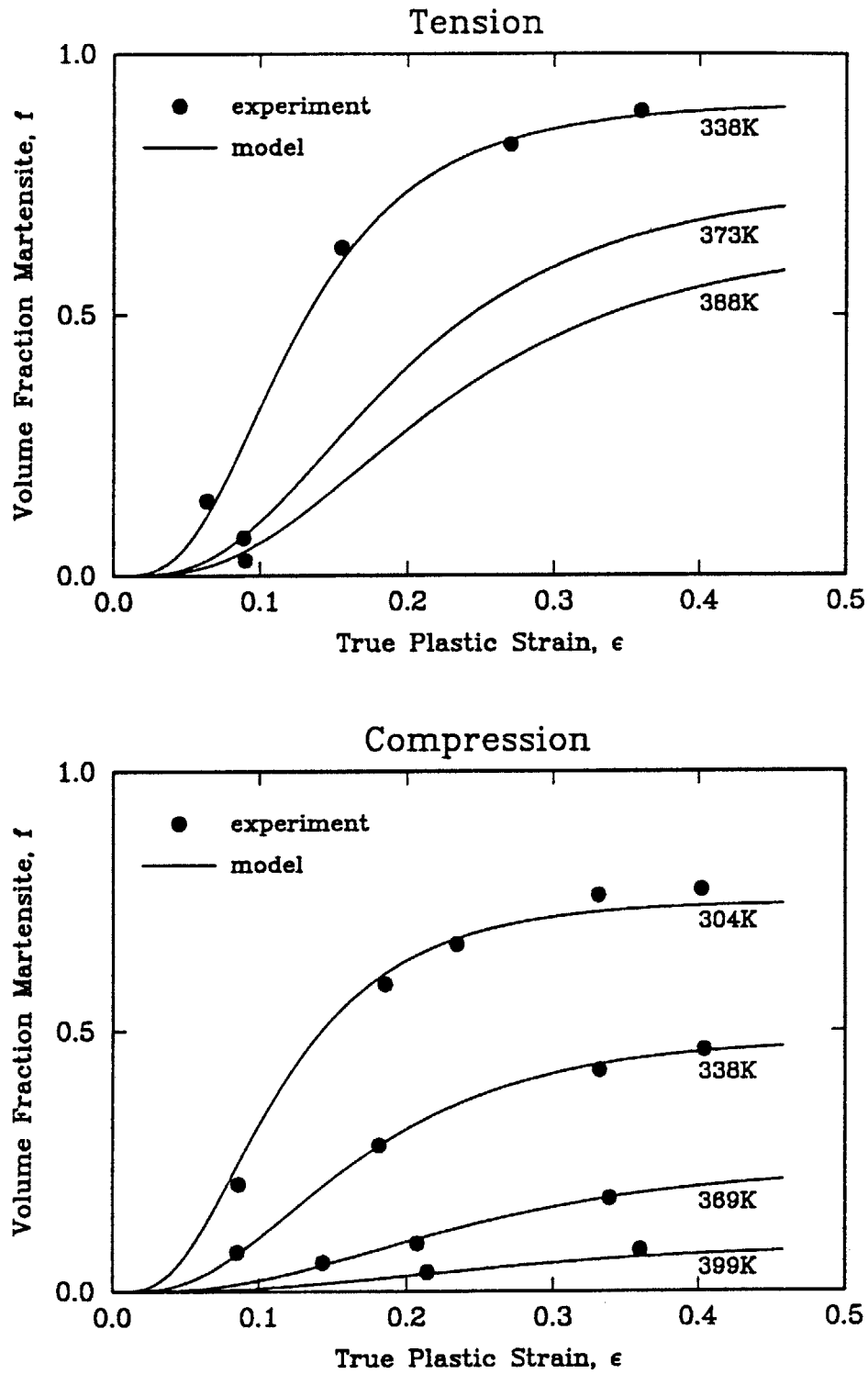
Figure 4.31 Comparison of model predictions for volume fraction martensite versus true plastic strain. Experimental points represent data measured during simple tension and compression tests for a 0.5 Mn overaged phosphocarbide-strengthened strain-induced transformation plasticity steel [64].
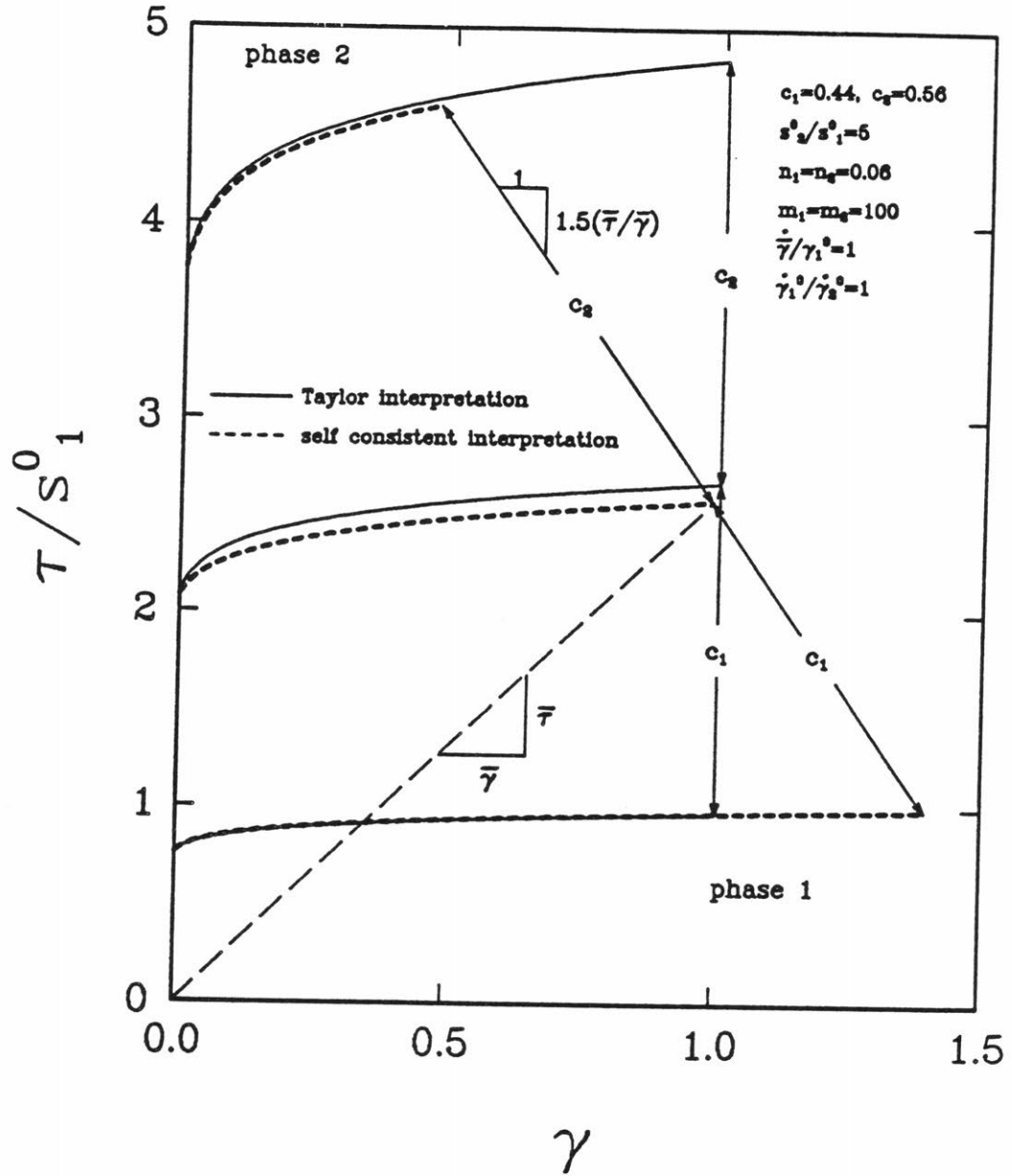
Figure 4.32 Geometric interpretation of partitioning of the strain such that the softer phase receives a larger strain. For equal and relatively small strain-hardening exponents, the slope of the line connecting (τ_1, γ_1) and (τ_2, γ_2) is approximately equal to $-1.5\ \tau/\gamma$ as shown. In addition, the relative distances between (τ, γ), (τ_1, γ_1) and (τ_2, γ_2) are as shown [65].

where 1 is the second-order identity tensor, ΔV is the transformation volume change, and

$$\overline{N} = \frac{\overline{D}}{|\overline{D}|}$$

(4.13)

is the macroscopic deviatoric normal tensor, and A is a coefficient of effective transformation strain. Furthermore,

$$\overline{S} = 2\overline{\mu}\overline{D}$$

(4.14)

where $\overline{S}$ is the stress deviator, and $\overline{\mu}$ is the shearing modulus.

The first two terms in Eq.4.11 represent the strain hardening of the two phases and the last term is the strain softening effect of transformation. In accordance with the Narutani-Olson-Cohen model, the new model retains the feature of strain hardening as a function of volume fraction martensite, and softening as function of nucleation strain rate. Figure 4.33 compares the new model with experimental stress-strain curves and the new model accounts well for the initial strain softening. The new model also incorporates the effect of stress state. Figure 4.34 illustrates the effect of five different stress states at constant temperature. As triaxiality increases, the amount of martensite formed increases, and the flow behavior is altered into the familiar S-shape, indicating TRIP behavior.

Since this new model takes into account the stress-state dependance and the volume-change of the transformation, Stringfellow [24] has recently completed crack tip calculations to model the observations made in this thesis work. Figure 4.35 shows the results of these calculations, expressed as equivalent plastic strain versus a characteristic dimensionless distance s from the crack tip which is located at 0,0.

Along the ligament, i.e., straight ahead of the crack tip, the transformation reduces the strain by a small amount. Along a 45 degree line out from the crack tip, the strain is

129
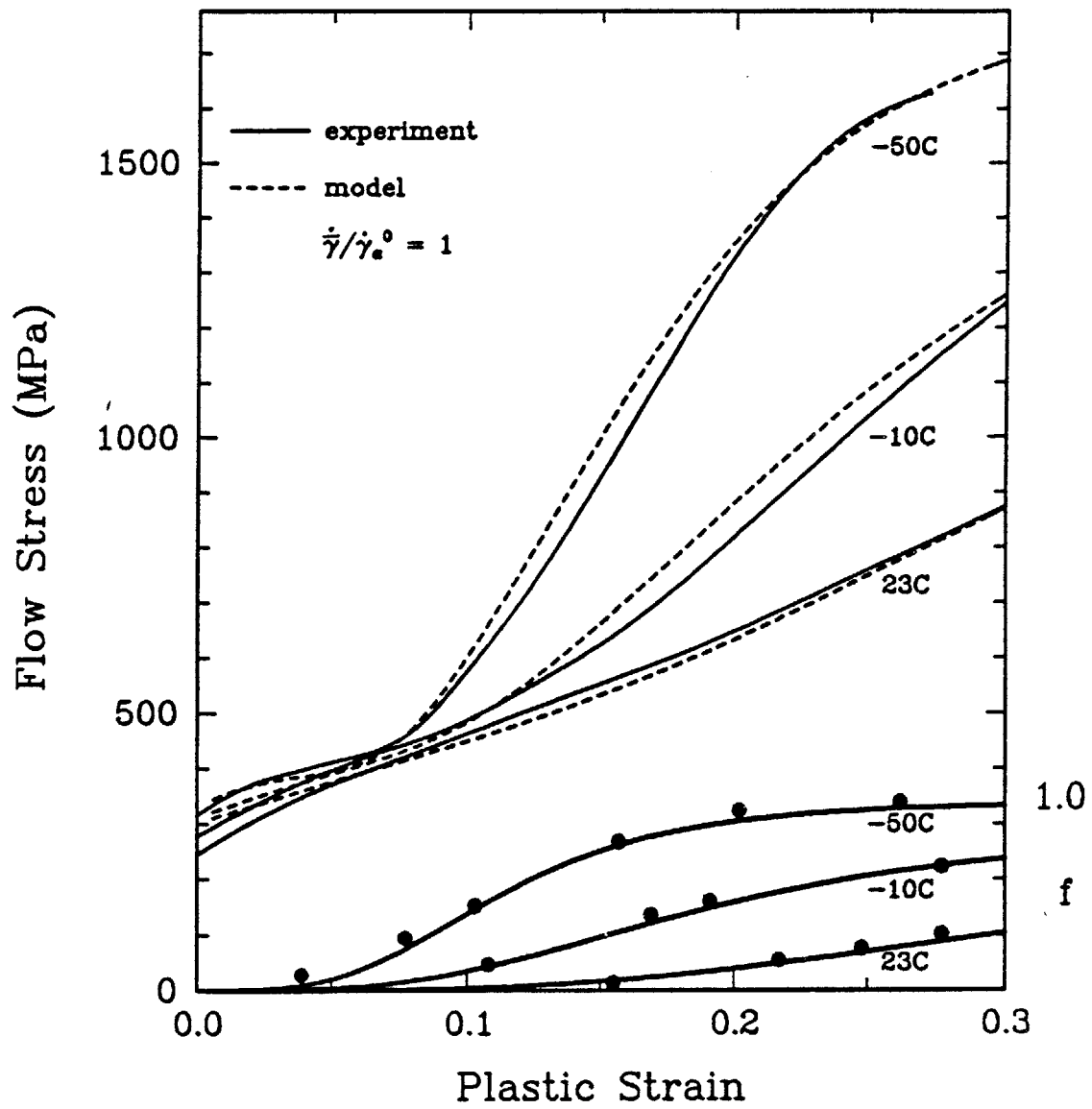
Figure 4.33 Comparison of modified self-consistent model prediction with experimental results from Narutani for a 0.12C-14Cr-7Ni-2Cu-1Mn strain-induced transformation plasticity steel at various temperatures [64].
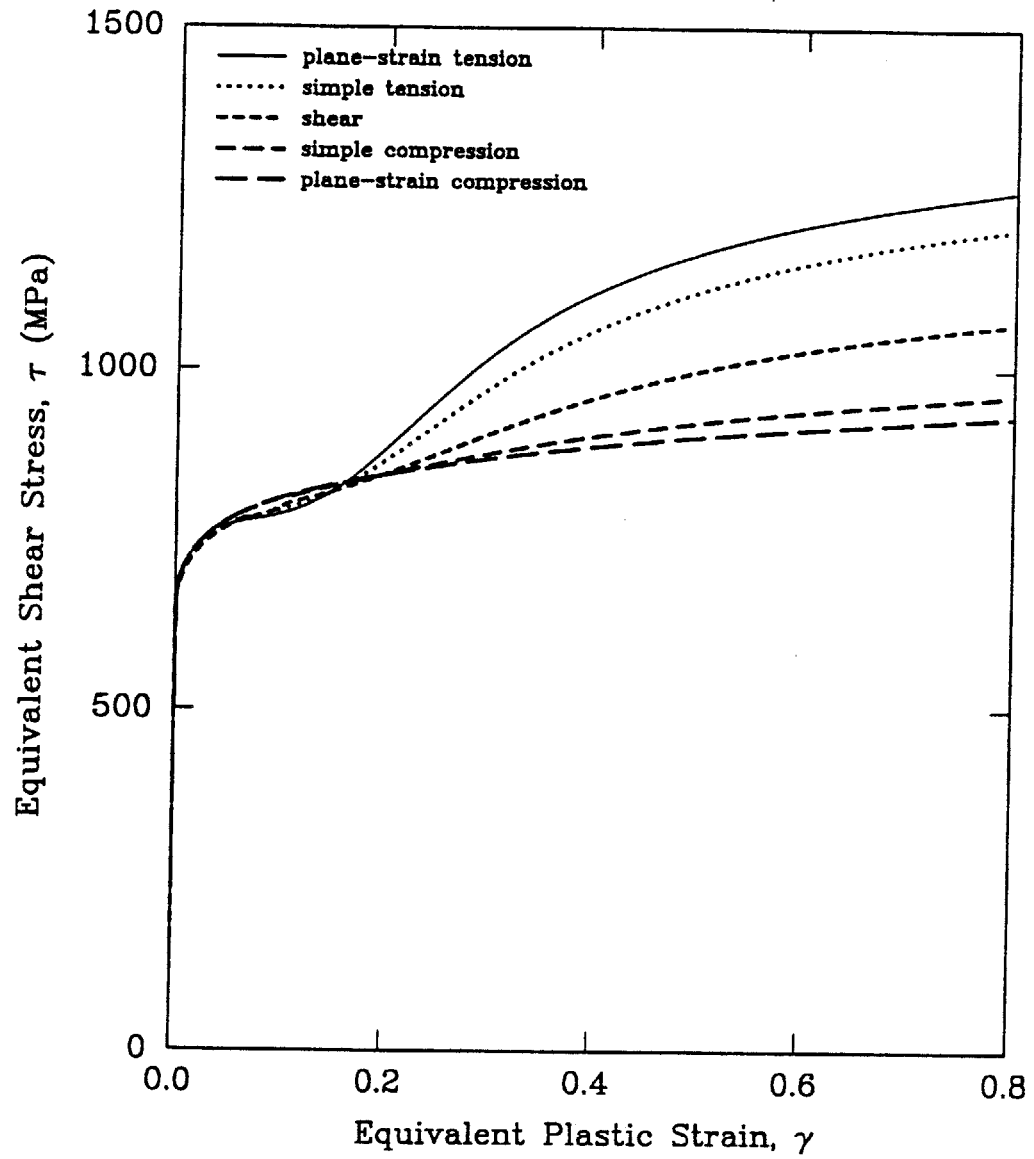
Figure 4.34 Equivalent shear stress, τ, plotted versus equivalent plastic strain, γ,for five one-element loading conditions: plane-strain tension, simple tension, pure shear, simple compression, and plane-strain compression [64].

131
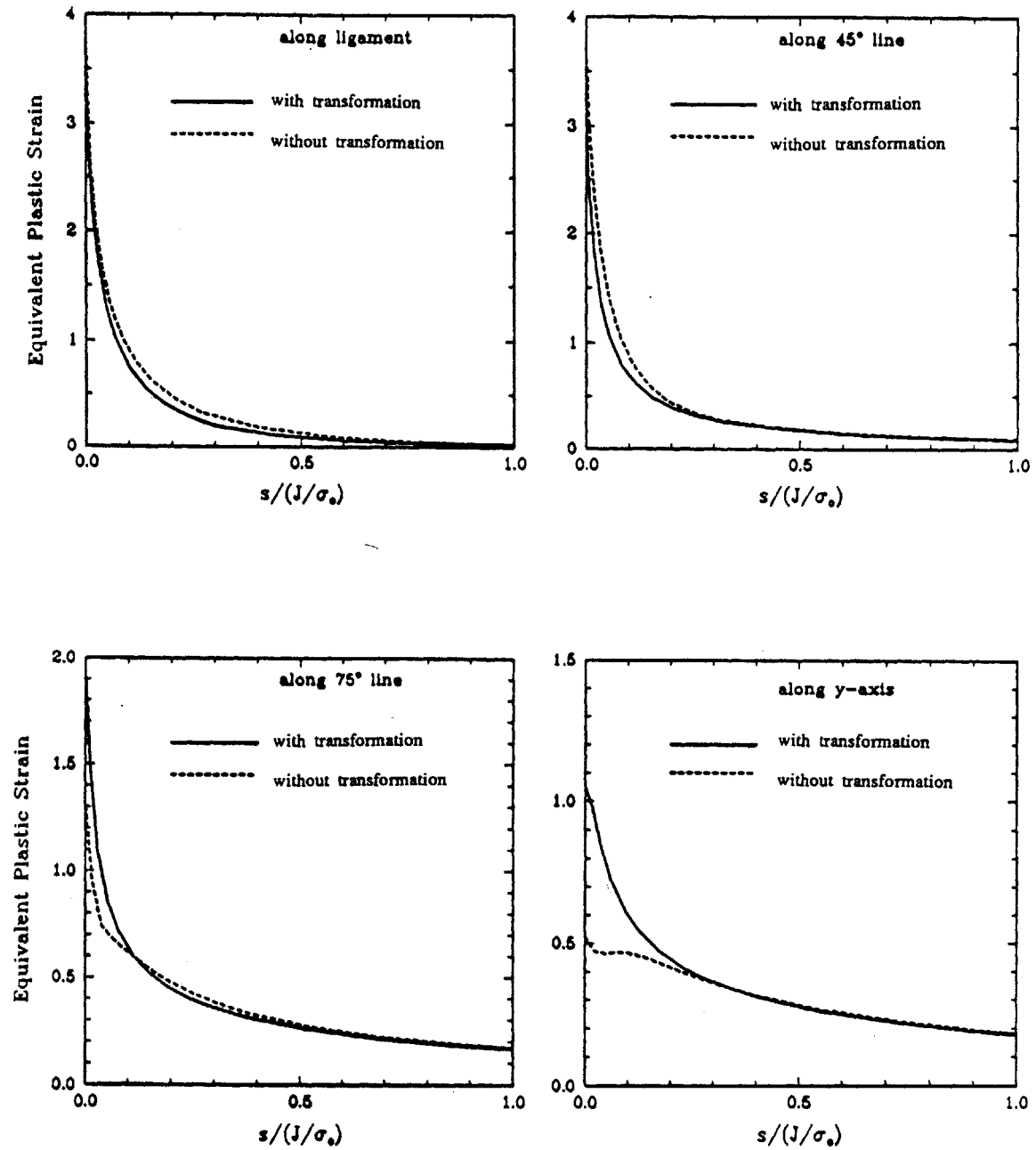
Figure 4.35 Equivalent plastic strain versus characteristic distance, s, along a line out from the crack tip [24].

132

lowered by the transformation until $s/(J/\sigma_y)$ is approximately 0.4, after which the two strains coincide. Thus, along the 45 degree line, transformation is only beneficial close to the crack tip. Figure 4.35c, which is along a 75 degree line, exhibits a very interesting behavior. For $s/(J/\sigma_y)>0.1$, the transformation reduces the strain, but in the region $s/(J/\sigma_y)<0.1$ the strain is higher after the transformation. Similar behavior is also seen in Figure 4.35d, which is along a 90 degree angle with the crack plane. At a distance $s/(J/\sigma_y)>0.3$, the strain is the same with and without transformation, but for $s/(J/\sigma_y)<0.3$, an increase in equivalent plastic strain is observed with transformation and at the crack surface there is a 100 percent increase in strain.

This model calculation predicts a redistribution of strain accompanying the transformation. The strain is lowered for angles less than 45 degrees, while the strain is increased for angles larger than 45 degrees. This indicates that the point of localization can be quite different in the presence of a strain-induced phase transformation. To investigate this, Stringfellow [24] examined the tendency toward localization using the new model. These results are summarized in Figure 4.36 for the nontransforming and transforming cases. Moving towards the crack tip in the nontransforming case and noting that localization is promoted by low $h/\bar{\sigma}$, localization continues to drop as the distance to the crack tip becomes smaller. Thus, as the distance decreases, flow stability is never regained. For the transforming case in Figure 4.36a, flow stability is momentarily lost as the crack tip is approached, but is regained once inside the hatched region. Thereafter, flow stability is again lost approaching the crack tip.

The localization calculations by Stringfellow [24] support the crack-tip observations of transformation toughening in this research. No failure criterion has been incorporated into the model by Stringfellow, so the exact point of failure/localization cannot be predicted, but the qualitative change of localization in the presence of transformation is well described and in agreement with crack-tip observations.
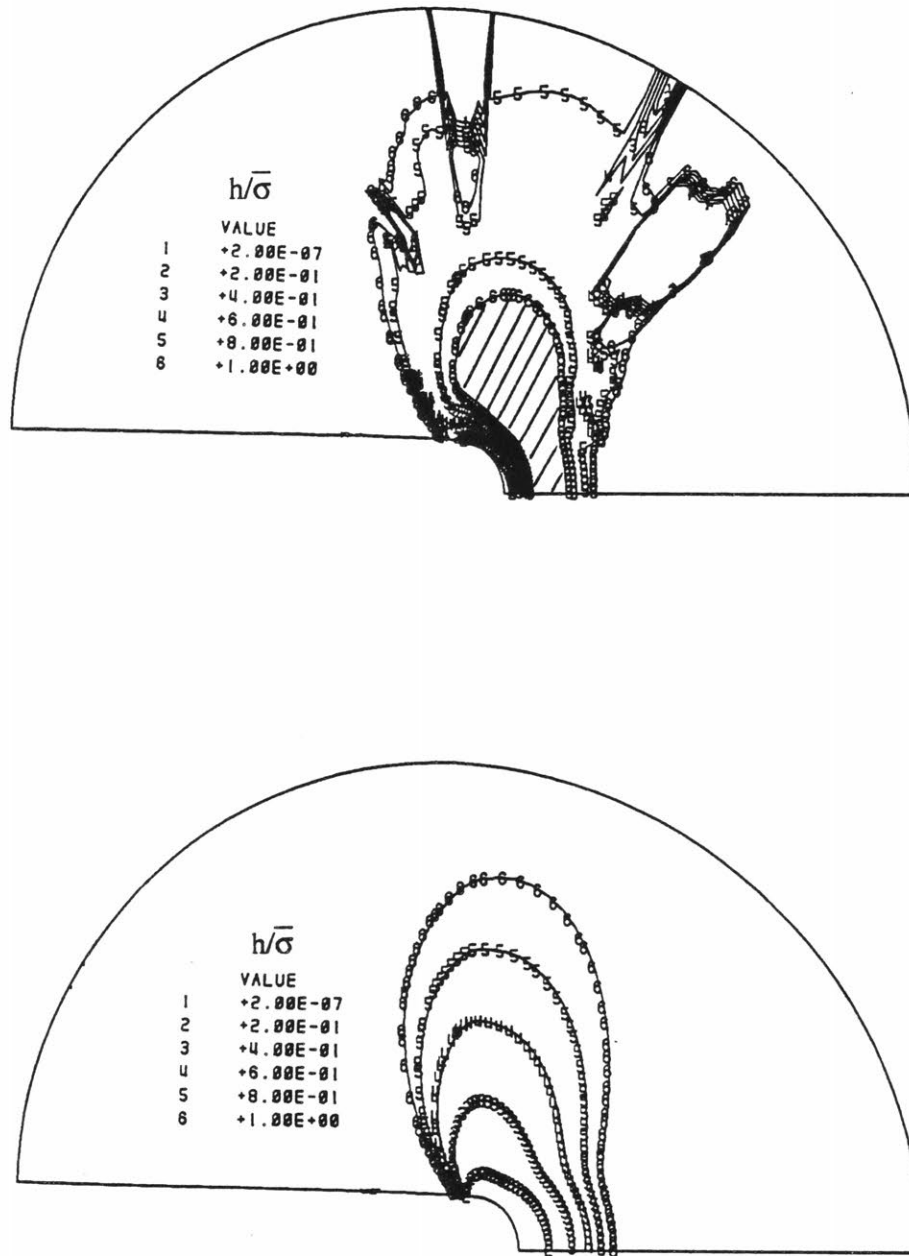
Figure 4.36 Localization parameters around the crack tip using self-similar model [24].
a) Transforming case, and b) Nontransforming case.

The presence of the transformation creates a region of high flow stability in front of the crack tip and the localization behavior is drastically altered. The region of high flow stability effectively blocks further crack advance and further localization must therefore find a path around this region of high flow stability. This forces localization to higher angles from the crack plane and all further straining is localized to very high angles, as illustrated previously by Figure 4.35c and d. To accommodate further increase in crack opening displacement (COD), shear localization is therefore limited to a very narrow region at very high angles as schematically illustrated in Figure 4.37. This permits a large COD with very small actual crack propagation, thus obtaining the extraordinary toughness levels encountered for in this research.

It should further be noted that model calculations previously applied without pressure sensitivity kinetics [23] did not show the dramatic redistribution of strains discussed here. This indicates that focusing of transformation ahead of the crack tip through pressure sensitivity is very important to the toughening, thus accounting for the previously observed important role of transformation dilatation [2].

$$\frac{1}{2}\frac{J}{\sigma_y} \approx CTOD$$
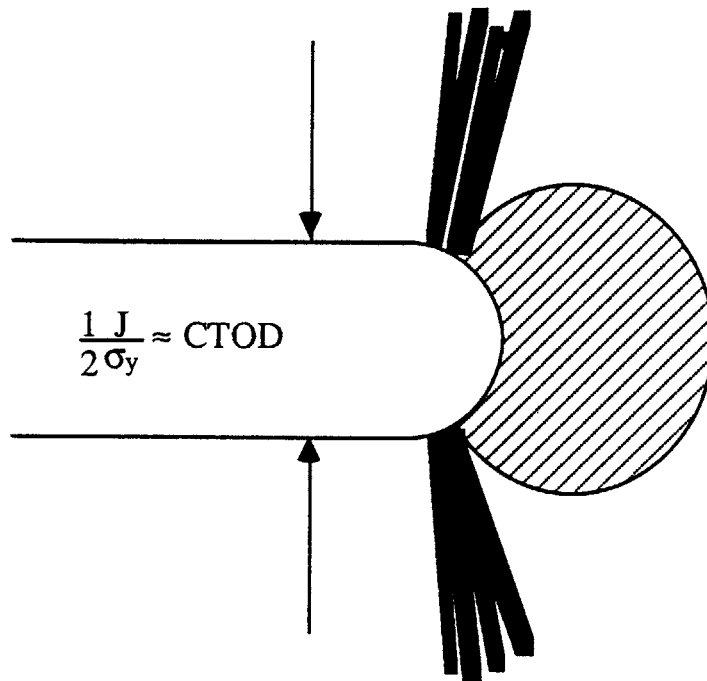
Transformed Zone

High triaxiality and high
strain $\Rightarrow$ high transformation.

Local hardening reduces
strain ahead of transformed
zone.

Flank Shear Zone

Lower strain and triaxiality
$\Rightarrow$ less transformation.

Total CTOD must be accommodated;
transformation ahead enhances strain
in flank shear zones.

Shear localization in flanks blunts
crack to accommodate large CTOD.

Figure 4.37 Schematic illustrating the effect of transformation
toughening on shear localization.

CHAPTER 5

CONCLUSIONS

On the basis of the results gathered and presented in this thesis the following conclusions can be drawn with regard to transformation toughening of γ'-strengthened metastable austenitic steels:

(1)   Utilizing thermodynamic principles, two series of alloys were designed based upon the γ'-precipitation hardened A286, containing 4% and 12% chromium. Thermodynamical driving-force calculations based on the assumption of a fixed critical driving force for transformation, indicated the nickel contents to place the $M_s^\sigma(c.t)$ at room temperature for maximum fracture toughness at room temperature. Measured toughness showed the simple model predicted the optimum nickel content within 3%.

(2)   A relationship between the critical transformation driving force and $(X_{Cr})^{2/3}$ can be used to compensate the effect of chromium on the critical driving force. The tensile strength, true strain, and J_{IC} fracture toughness for both alloy series can then be plotted versus the difference between the total driving force and the critical driving force at M_s^σ. This driving force increment becomes equivalent to the normalized temperature parameter θ previously employed to quantify relative transformation

stability. Incorporating the kinetic effect of chromium allows greater precision in predicting optimal alloy compositions for transformation toughening.

(3) A maximum fracture toughness of 350 MPa√m̄ (320 ksi√in̄) was obtained at a yield strength of 1410 MPa (205 ksi) for the low chromium series, and 335 MPa√m̄ (305 ksi√in̄) was obtained at a yield strength of 1200 MPa (175 ksi) for the high chromium stainless series. This represents an almost three-fold increase in fracture toughness over the stable austenite at 130 MPa√m̄ (120 ksi√in̄), and it is a two-fold increase in fracture toughness over commercial precipitation-hardenable stainless steels of the same strength level.

(4) The strain-induced martensitic transformation was found to change the shape of the fracture-toughness load-displacement curve from a negative to positive curvature, thus delaying the onset of fracture instability to a higher load and larger displacement.

(5) A forked or fan-like extension of martensite out in front of the crack tip is observed in the stress-assisted transformation range $(T<M_s^\sigma(c.t))$, while an elliptical zone is observed in the strain-induced region $(T>M_s^\sigma(c.t))$.

(6) The mechanism responsible for fracture toughness enhancement appears to be essentially the same for both stress-assisted and strain-induced transformation. Mechanically-induced martensite is initially formed in front of the crack tip. The associated high strain hardening in this region forces strain localization elsewhere, promoting crack branching and square blunting. Just above $M_s^\sigma(c.t)$, continued straining initiates shear fracture in the upper and lower corners of the blunted crack. Continued crack opening then occurs by shear localization along a very narrow region located at a high angle of approximately 75 degrees, until the COD becomes so large that the crack can circumvent the transformed region ahead of the blunted

crack. This point corresponds to maximum applied load and J_{IC}. Similar features occur below $M_s^\sigma(c.t)$, but toughening is apparently less effective when the fracture path can follow the more brittle fully transformed zone.

(7)   Comparison of observed localization behavior with crack-tip strain distributions predicted by application of a transformation plasticity constitutive model indicates that the pressure sensitivity of strain-induced transformation kinetics (determined by the transformation volume change) is important to the strain redistribution which favors crack-tip branching and localization at a high angle to the primary crack plane. Such modelling may ultimately allow design of transformation kinetics to allow further enhancement of transformation toughening efficiency.

CHAPTER 6

SUGGESTIONS FOR FUTURE RESEARCH

The following suggestions are made for future research:

(1) To examine the toughening enhancement as a function of aging temperature. There are indications that the overaged condition provides a larger toughening enhancement when compared to the previous work by Leal [1], and Young [2].

(2) To examine the toughening as a function of temperature to determine the maximum achievable fracture toughness, since alloys 428 and 1217 were "end" alloys.

(3) New alloys can be made to further investigate the possibility of maximum fracture toughness outside the range studied in this thesis. From a commercial point of view, it would be attractive to investigate the low nickel end, i.e., the 12% chromium series, because of the high cost of nickel.

(4) Further research to determine the optimum precipitation behavior to optimize the strength level. This in combination with additional warm working should move the strength to higher levels where more fracture toughness is desired.

(5)   Precision lattice parameter measurements as a function of aging temperature to maximize the transformation volume change to gain more transformation toughening.

(6)   A pressure-dependent localization criterion need to be developed to gain insight into shear localization. This will be a very useful tool in conjunction with the crack tip observations to develop a better understanding of the finer points of shear localization.

APPENDIX A

DETERMINATION OF CRACK LENGTH IN THREE-POINT BEND SPECIMEN

In order to successfully perform single-specimen J-integral fracture toughness testing, the crack advance during the test has to be monitored. One way to achieve this is by compliance measurements. As the crack advances during the test, the compliance of the specimen increases. By monitoring the total load point displacement, the specimen compliance can be obtained. In this section the relationship between compliance and crack length for a three-point bend specimen geometry will be derived.

A three-point bend specimen geometry can be treated as a simple beam with the additional presence of a crack. Therefore, the total load point displacement, Δ, for the three-point bend specimen can be expressed as:

$$\Delta = \Delta_{n.c} + \Delta_c \qquad (A1)$$

where $\Delta_{n.c.}$ is the load point displacement without a crack, i.e. a simple beam geometry, and Δ_c is the additional load point displacement due to the presence of a crack.

$\Delta_{n.c.}$ is taken from elementary beam theory [66] and is:

$$\Delta_{n.c} = \frac{P S^3}{48 E' I} \qquad (A2)$$

where P is the load, S is the span, i.e. the distance between the rollers, E' is the modified modulus of elasticity for plane strain, and I is the moment of inertia. E' is:

$$E' = \frac{E}{1 - \nu^2} \qquad (A3)$$

142

where E is the modulus of elasticity and v is Poisson's ratio. I is expressed as:

$$I = \frac{B W^3}{12}$$ (A4)

where B is the thickness of the specimen and W is the width of the specimen. Combining equations (A2-A4) gives:

$$\Delta_{n.c} = \frac{P}{4 B E'} \left(\frac{S}{W}\right)^3$$ (A5)

In this thesis S/W=4 and therefore:

$$\Delta_{n.c} = \frac{16 P}{B E'}$$ (A6)

The additional load point displacement due to the presence of a crack, Δ_c, has been documented by Tada et al. [67].:

$$\Delta_c = \frac{\sigma S}{E'} V_2 \left(\frac{a}{W}\right)$$ (A7)

where

$$\sigma = \frac{6 M}{B W^2}$$ (A8)

where M is the bending moment and is equal to:

$$M = \frac{P S}{4}$$ (A9)

and V_2 is a function of a/W expressed as:

143

$$V_2 = \left(\frac{\frac{a}{W}}{1 - \left(\frac{a}{W}\right)}\right)^2 \left[5.58 - 19.57\left(\frac{a}{W}\right) + 36.82\left(\frac{a}{W}\right)^2 - 34.94\left(\frac{a}{W}\right)^3 + 12.77\left(\frac{a}{W}\right)^4\right] \quad \text{(A10)}$$

Combining equations (A7-A10) and using S/W=4 we obtain:

$$\Delta_c = \frac{24P}{BE'} V_2\left(\frac{a}{W}\right) \quad \text{(A11)}$$

Therefore the total load point displacement is:

$$\Delta = \frac{16P}{BE'} + \frac{24P}{BE'} V_2\left(\frac{a}{W}\right) \quad \text{(A12)}$$

The compliance, C, is:

$$C = \frac{\Delta}{P} \quad \text{(A13)}$$

and therefore:

$$\frac{\Delta E' B}{P} = 16 + 24V_2\left(\frac{a}{W}\right) \quad \text{(A14)}$$

where $(\Delta E'B)/P$ is the normalized specimen compliance.

Equation A14 gives the normalized specimen compliance as a function of (a/W). In an experiment the normalized specimen compliance is known and we are therefore searching for (a/W) as a function of the normalized specimen compliance:

$$\frac{a}{W} = f\left(\frac{\Delta E' B}{P}\right) \quad \text{(A15)}$$

This can be achieved by assuming an n-th order polynomial [68]:

144

$$\frac{a}{W} = C_0 + C_1U + C_2U^2 + \dots + C_nU^n \tag{A16}$$

Saxena and Hudak [69] have for many different specimen geometries used the following expression for U:

$$U = \left[\frac{1}{1 + \left(\frac{\Delta E'B}{P}\right)^{\frac{1}{2}}} \right] \tag{A17}$$

An attempt to solve equation (A16) gives rise to the following system of equations:

$$
\begin{bmatrix}
1 & U_1 & (U_1)^2 & \cdots & (U_1)^n \\
1 & U_2 & (U_2)^2 & \cdots & (U_2)^n \\
1 & U_3 & (U_3)^2 & \cdots & (U_3)^n \\
\vdots & \vdots & \vdots & & \vdots \\
1 & U_n & (U_n)^2 & \cdots & (U_n)^n
\end{bmatrix}
\begin{bmatrix}
C_0 \\
C_1 \\
C_2 \\
\vdots \\
C_{(n-1)}
\end{bmatrix}
=
\begin{bmatrix}
\left(\frac{a}{W}\right)_1 \\
\left(\frac{a}{W}\right)_2 \\
\left(\frac{a}{W}\right)_3 \\
\vdots \\
\left(\frac{a}{W}\right)_n
\end{bmatrix}
\tag{A18}
$$

or

$$[A]\,\overline{X} = \overline{B} \tag{A19}$$

The solution to this system of equations is

$$[A^T][A]\,\overline{X} = [A^T]\,\overline{B} \tag{A20}$$

This system of equations was solved numerically by Gaussian Elimination and Pivoting.

For $0.5 \leq (a/W) \leq 0.9$ and using six constants for high accuracy, the following expression was obtained:

$$\frac{a}{W} = C_0 + C_1 U + C_2 U^2 + C_3 U^3 + C_4 U^4 + C_5 U^5 \qquad \text{(A21)}$$

where $C_0 = 0.9878$, $C_1 = -3.0106$, $C_2 = -15.4301$, $C_3 = 59.9455$, $C_4 = 296.505$, $C_5 = -2171.2354$, and U is obtained from equation (A17). This expression has better than 1% accuracy in the range stated above.

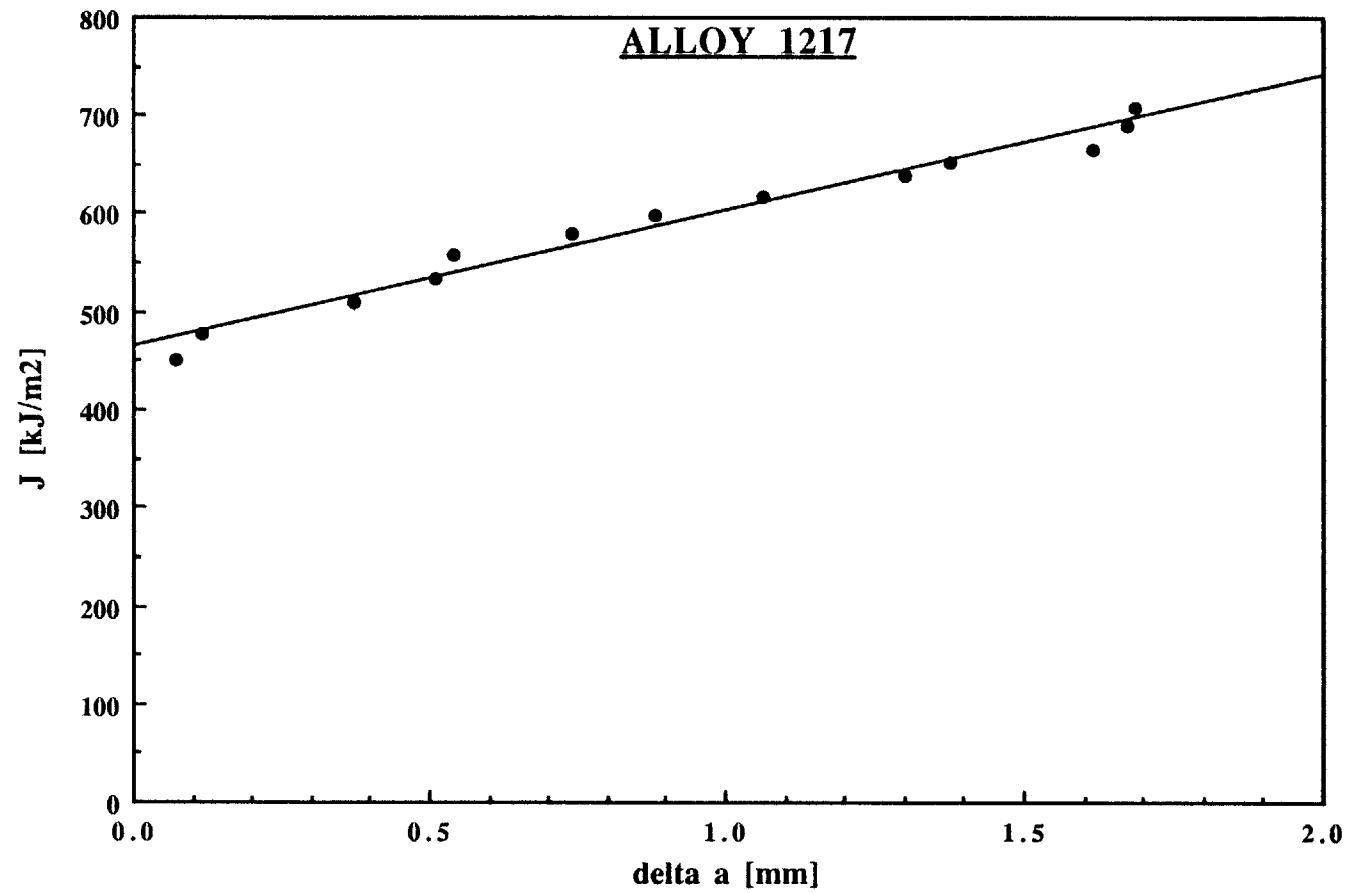# APPENDIX B

J vs. CRACK EXTENSION FOR ALL ALLOYS

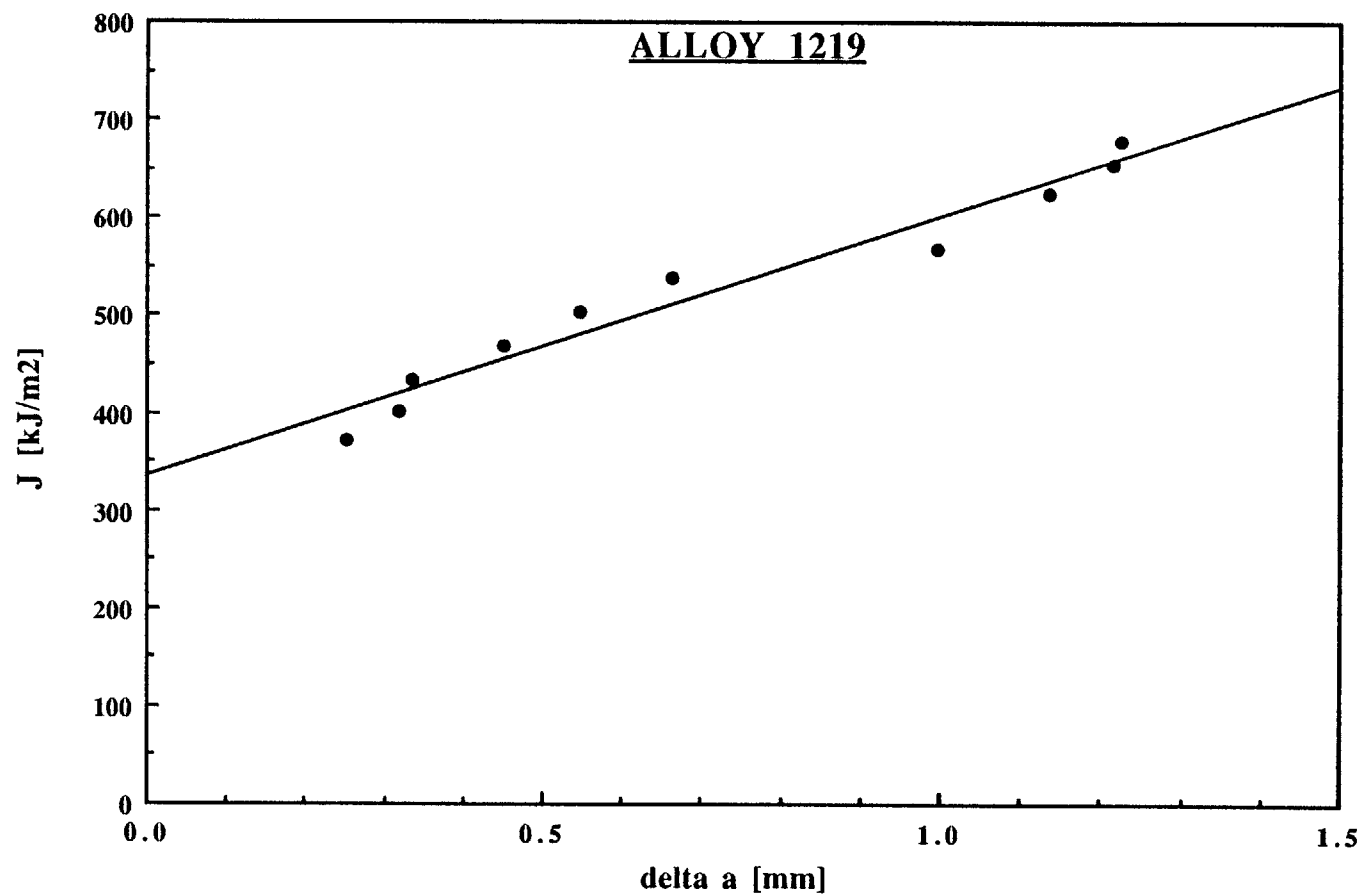**Figure B.1** J values versus crack extension Δa for alloy 1217.

Figure B.2 J values versus crack extension Δa for alloy 1219.

Figure B.3 J values versus crack extension Δa for alloy 1221.

Figure B.4 J values versus crack extension Δa for alloy 1223.

ALLOY 424

Figure plot: J [kJ/m2] versus delta a [mm]
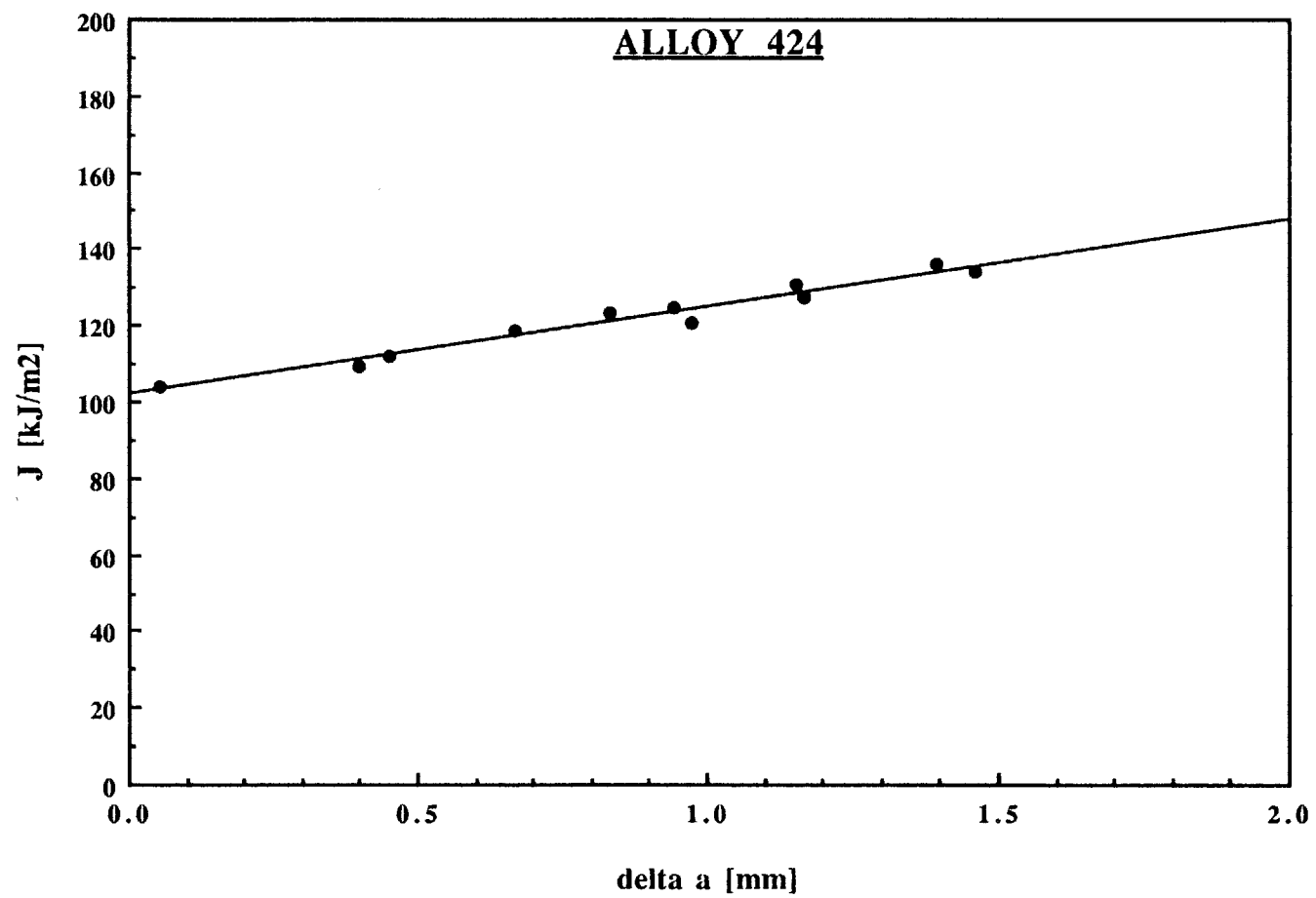
Figure B.5 J values versus crack extension Δa for alloy 424.
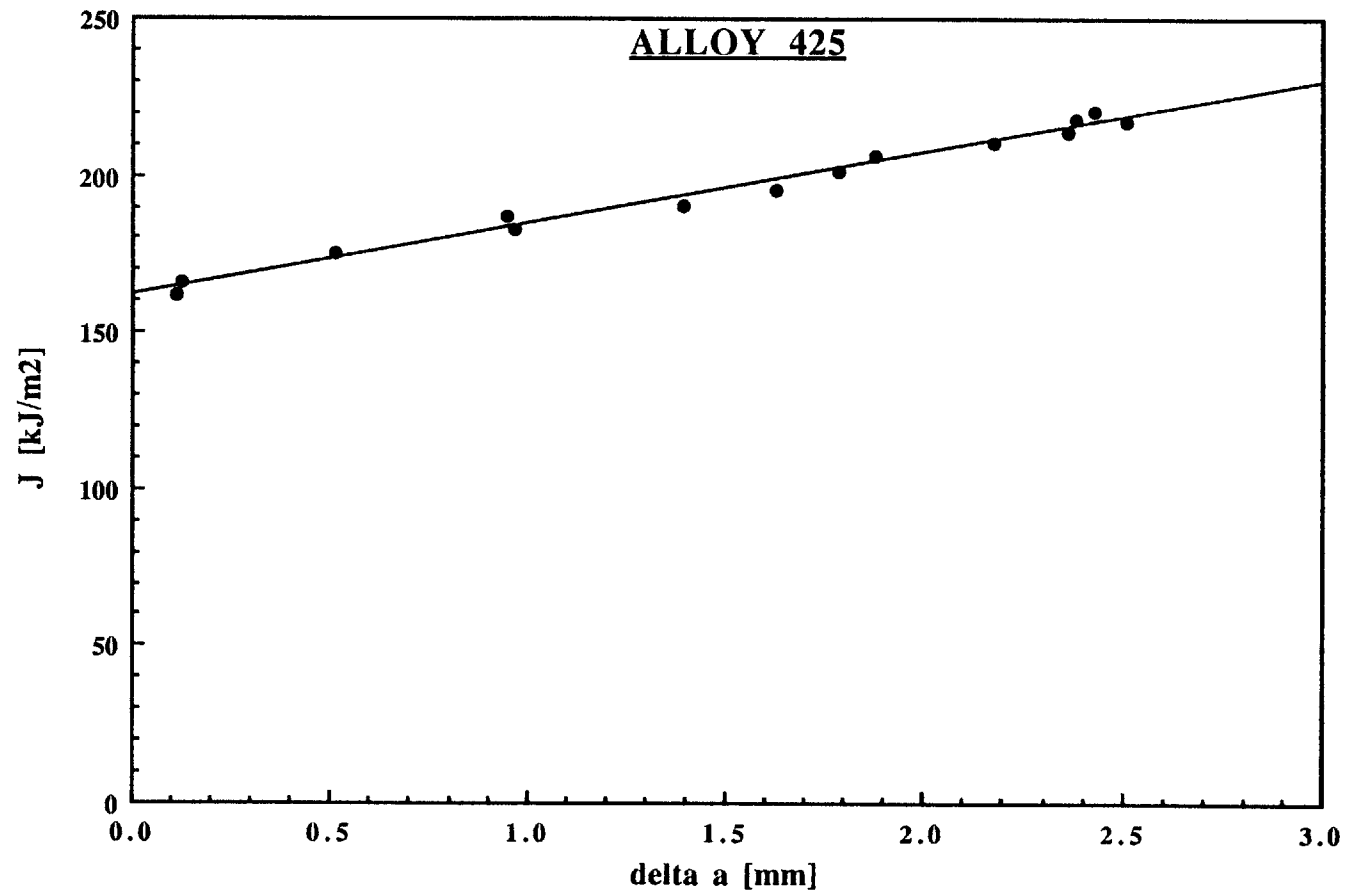
Figure B.6 J values versus crack extension Δa for alloy 425.

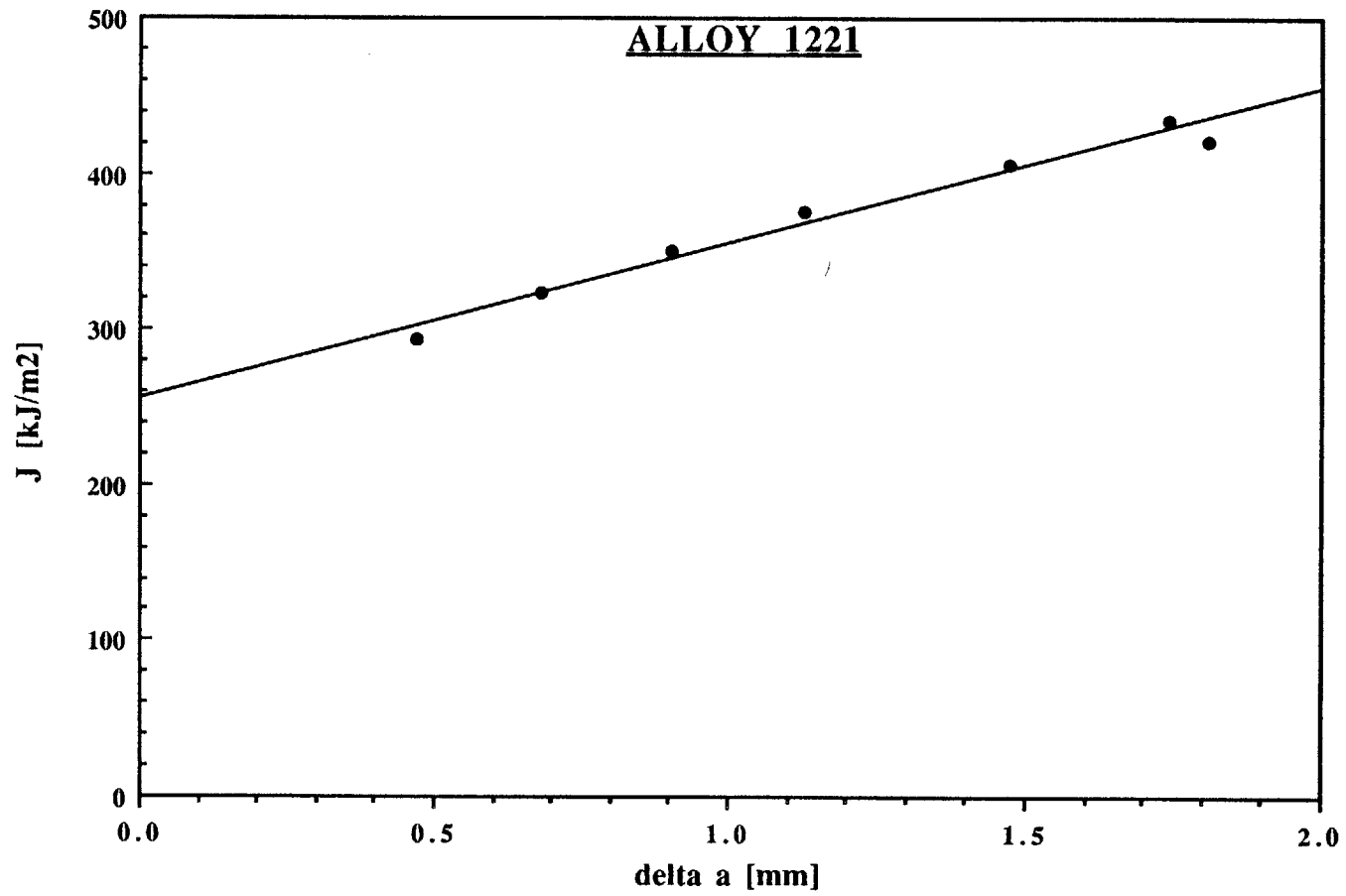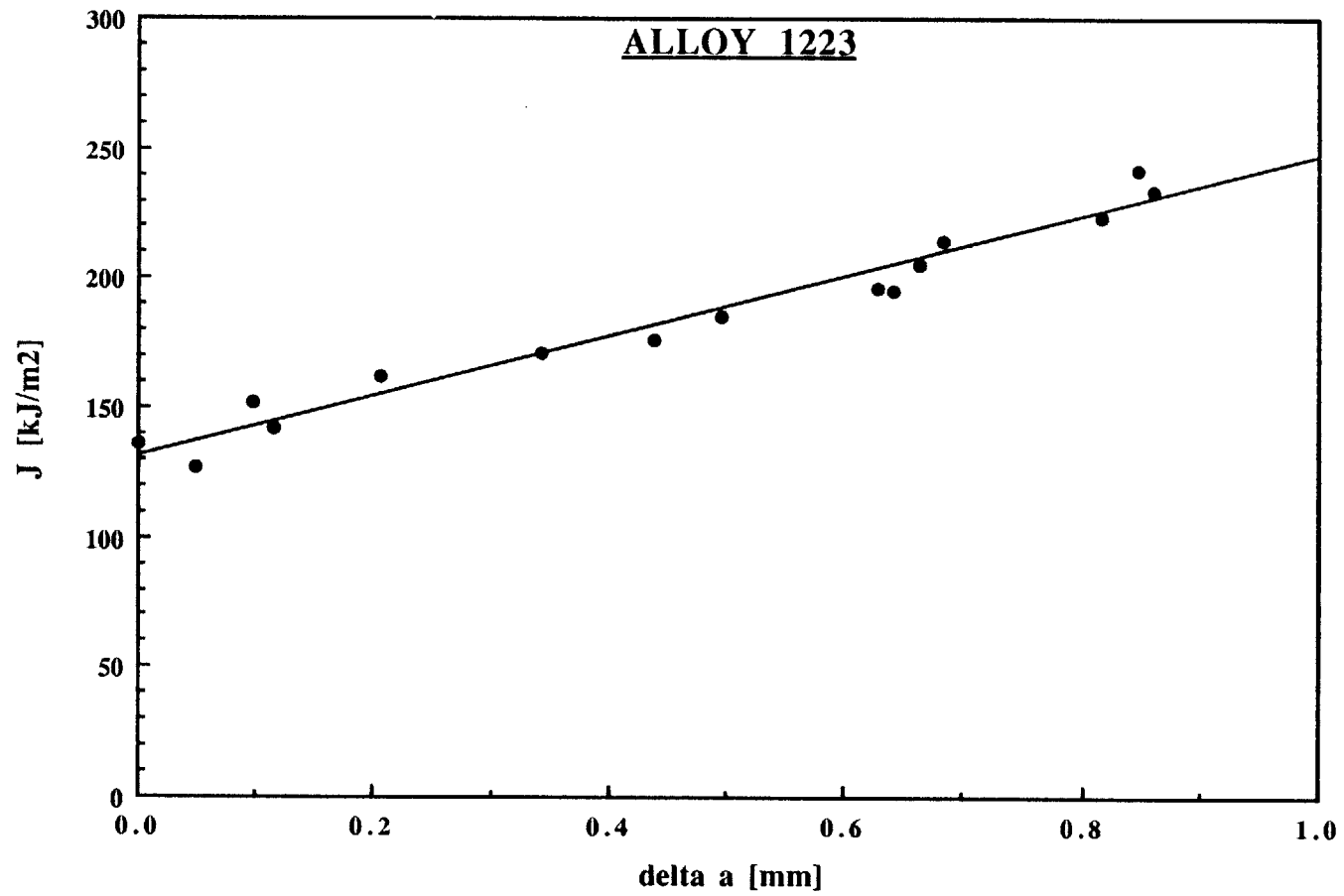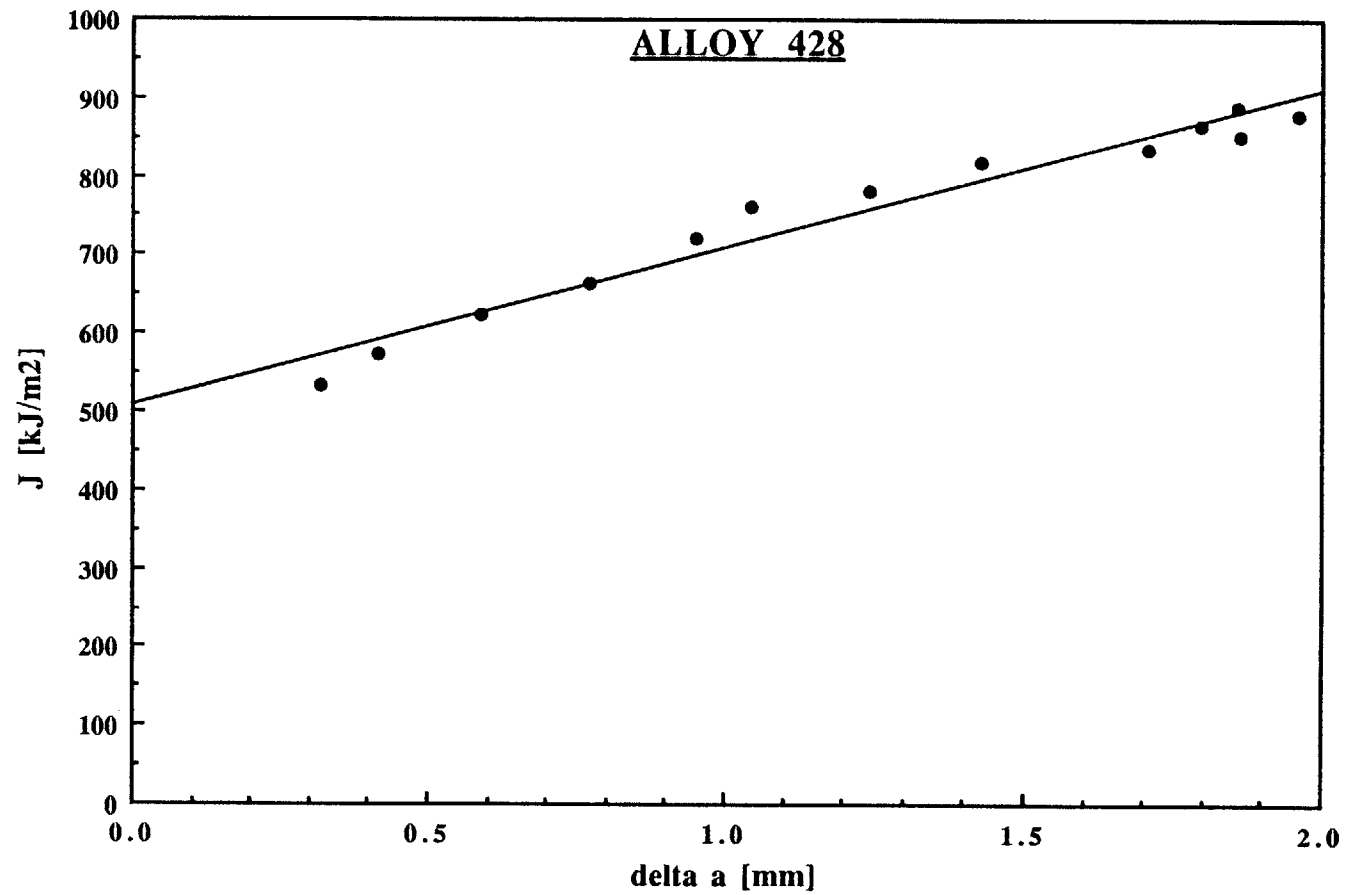**Figure B.7** J values versus crack extension Δa for alloy 428.

APPENDIX C

LOAD-DISPLACEMENT CURVES FOR ALL ALLOYS

Figure C.1 Load-displacement curve for alloy 1217.

$a_0 = 6.128$ mm

Figure C.2 Load-displacement curve for alloy 1219.

Figure C.3 Load-displacement curve for alloy 1221.

Figure C.4 Load-displacement curve for alloy 1223.

Figure C.5 Load-displacement curve for alloy 424.

Figure C.6 Load-displacement curve for alloy 425.

LIST OF REFERENCES

1. R.H. Leal, "Transformation Toughening of Metastable Austenitic Steels," Doctoral Thesis, Department of Materials Science and Engineering, Massachusetts Institute of Technology, Cambridge, MA (1984).
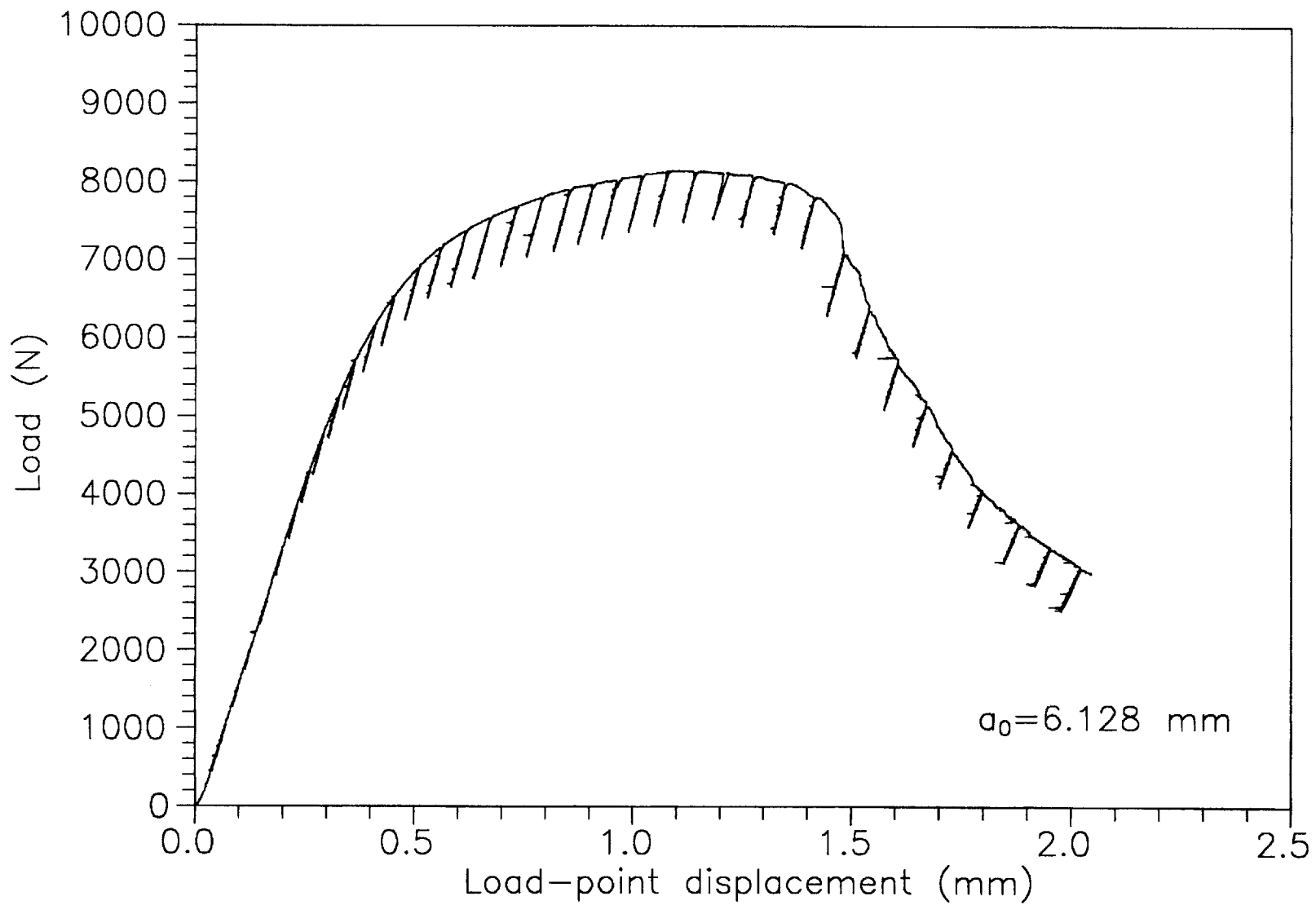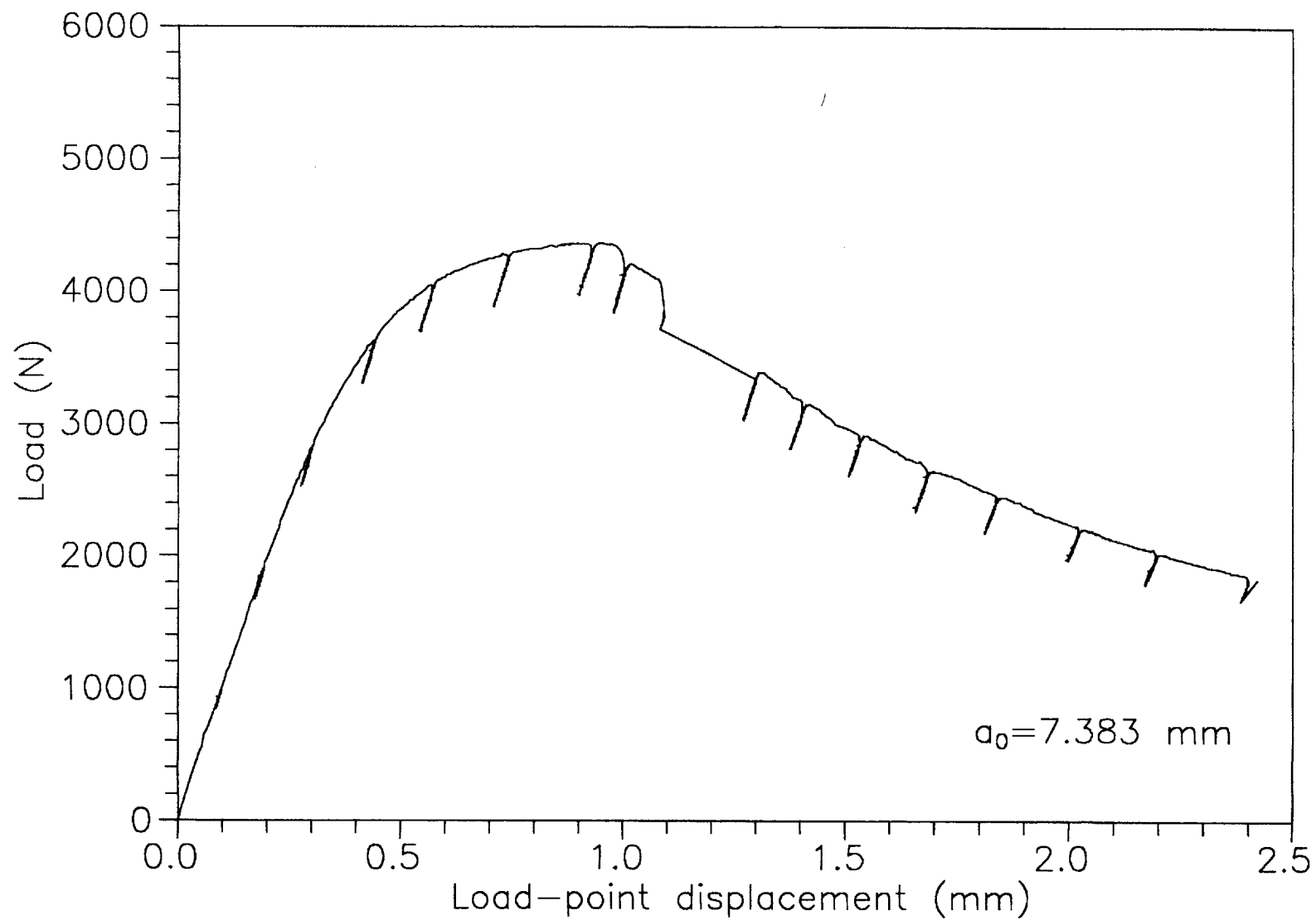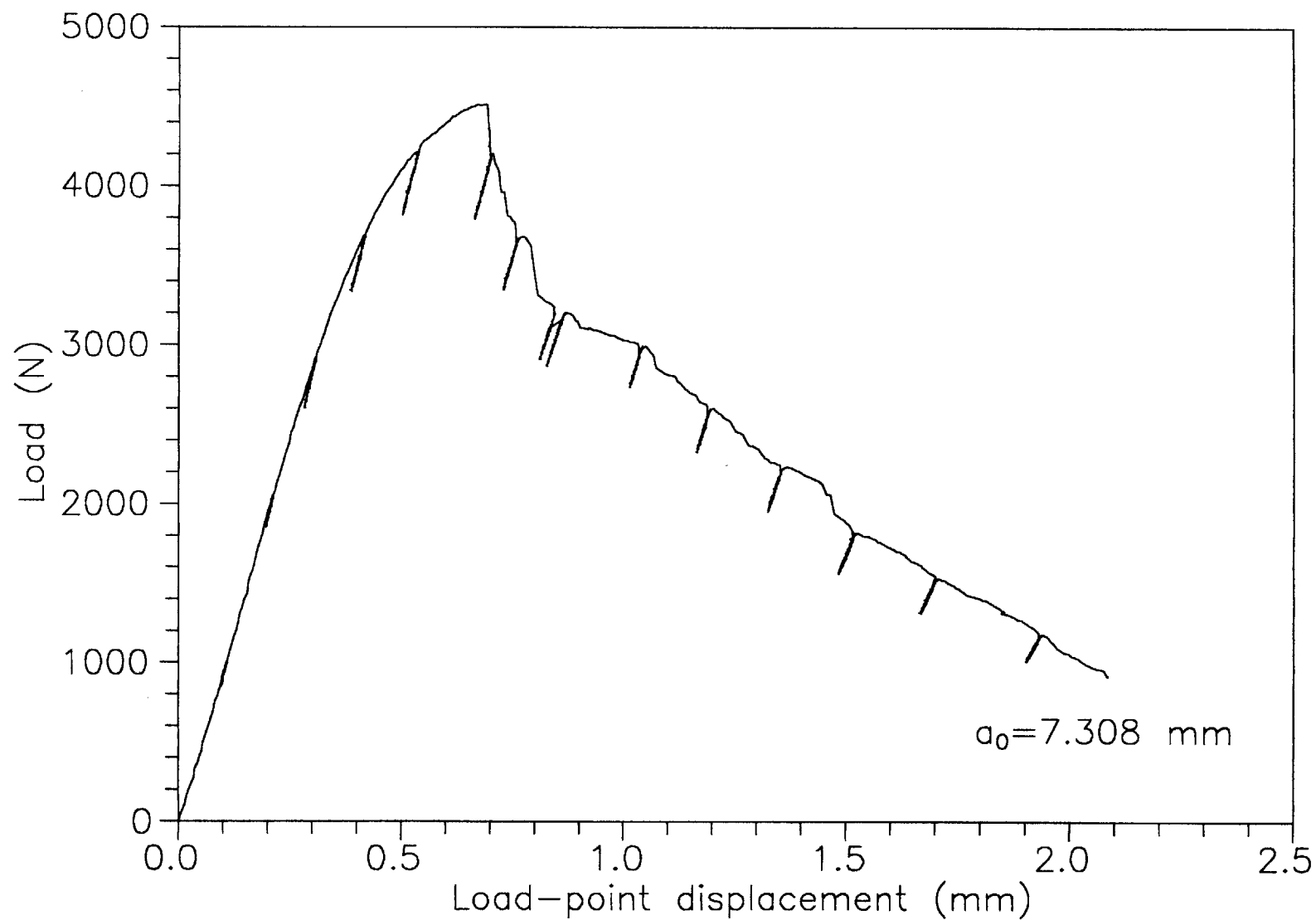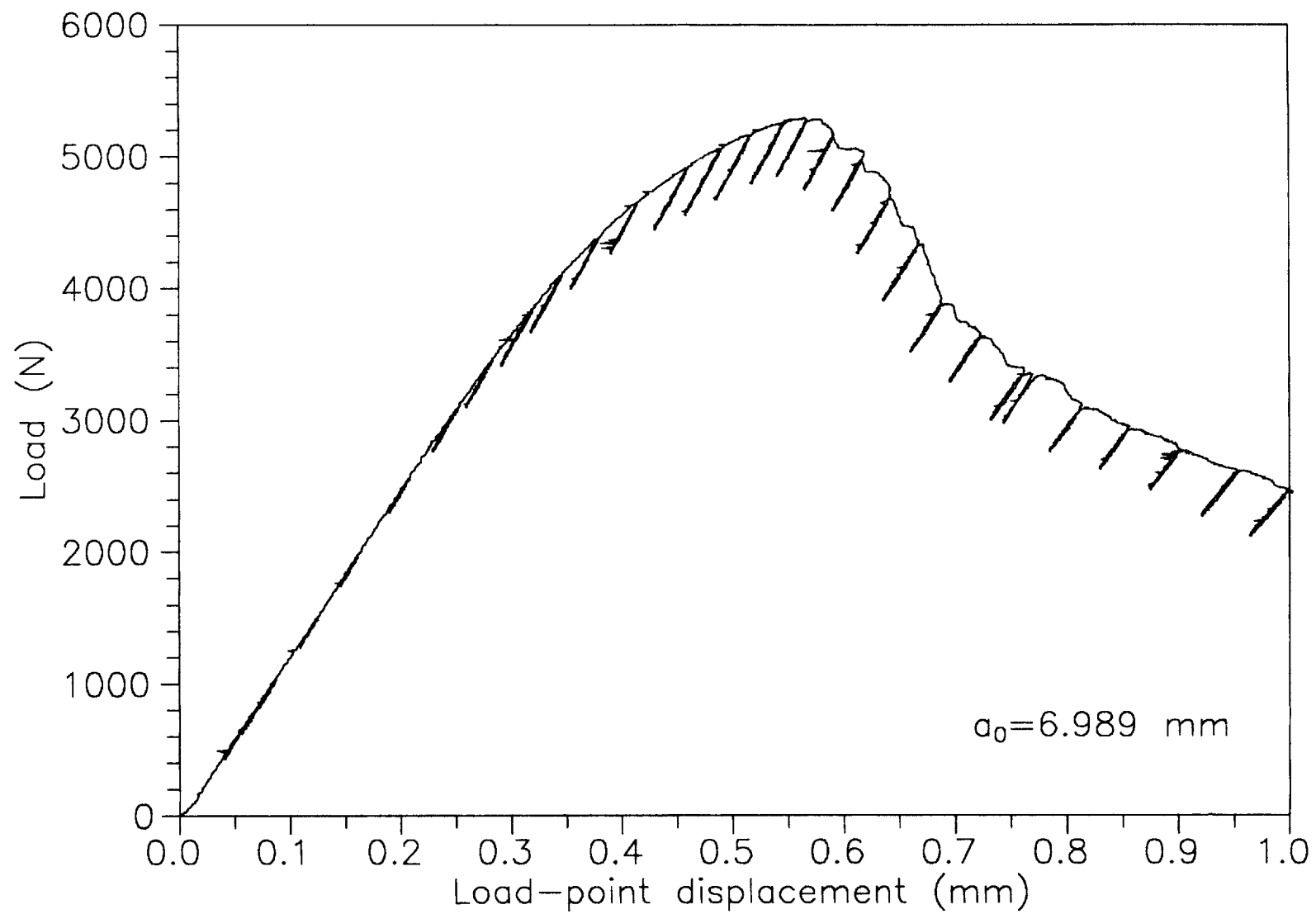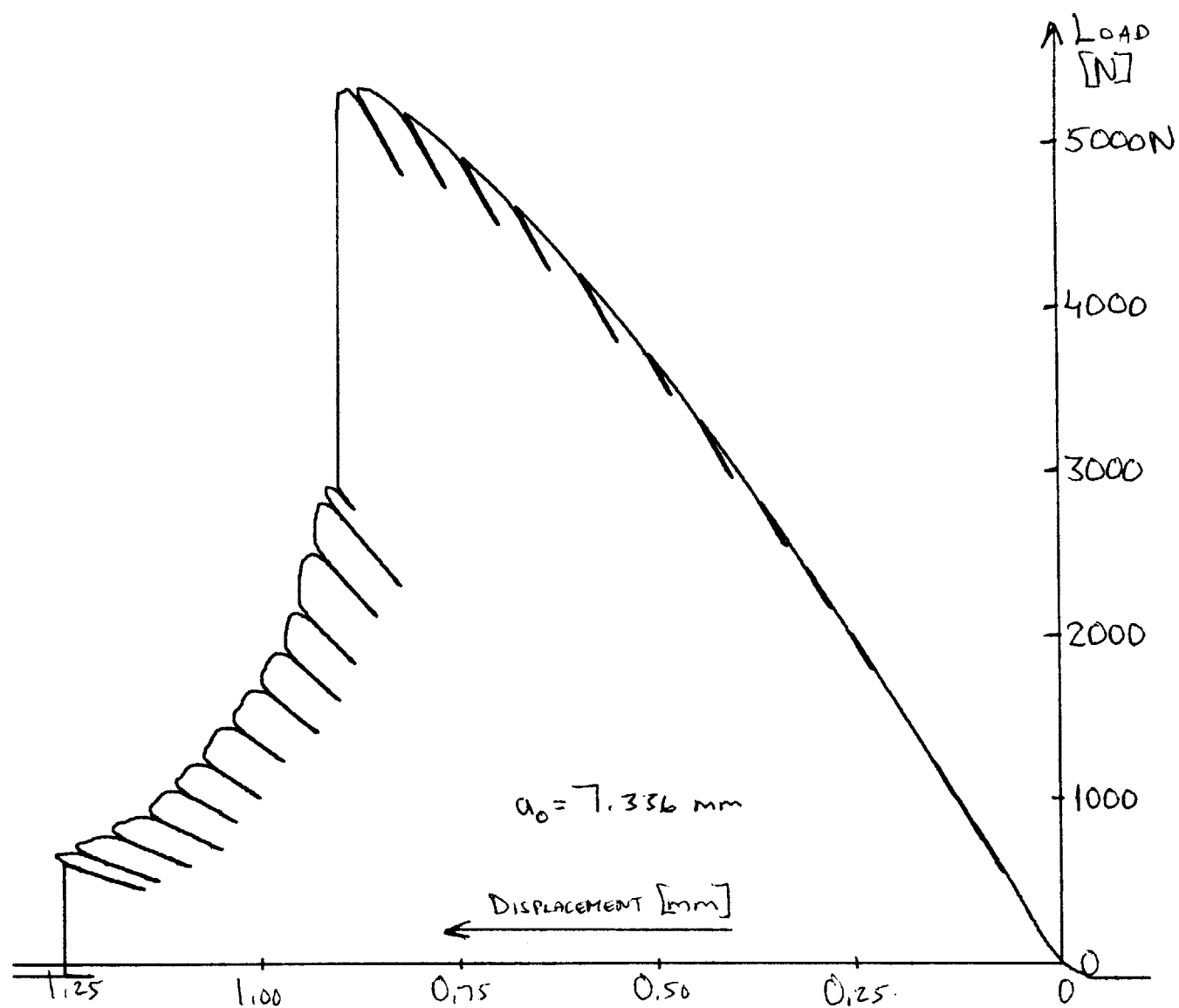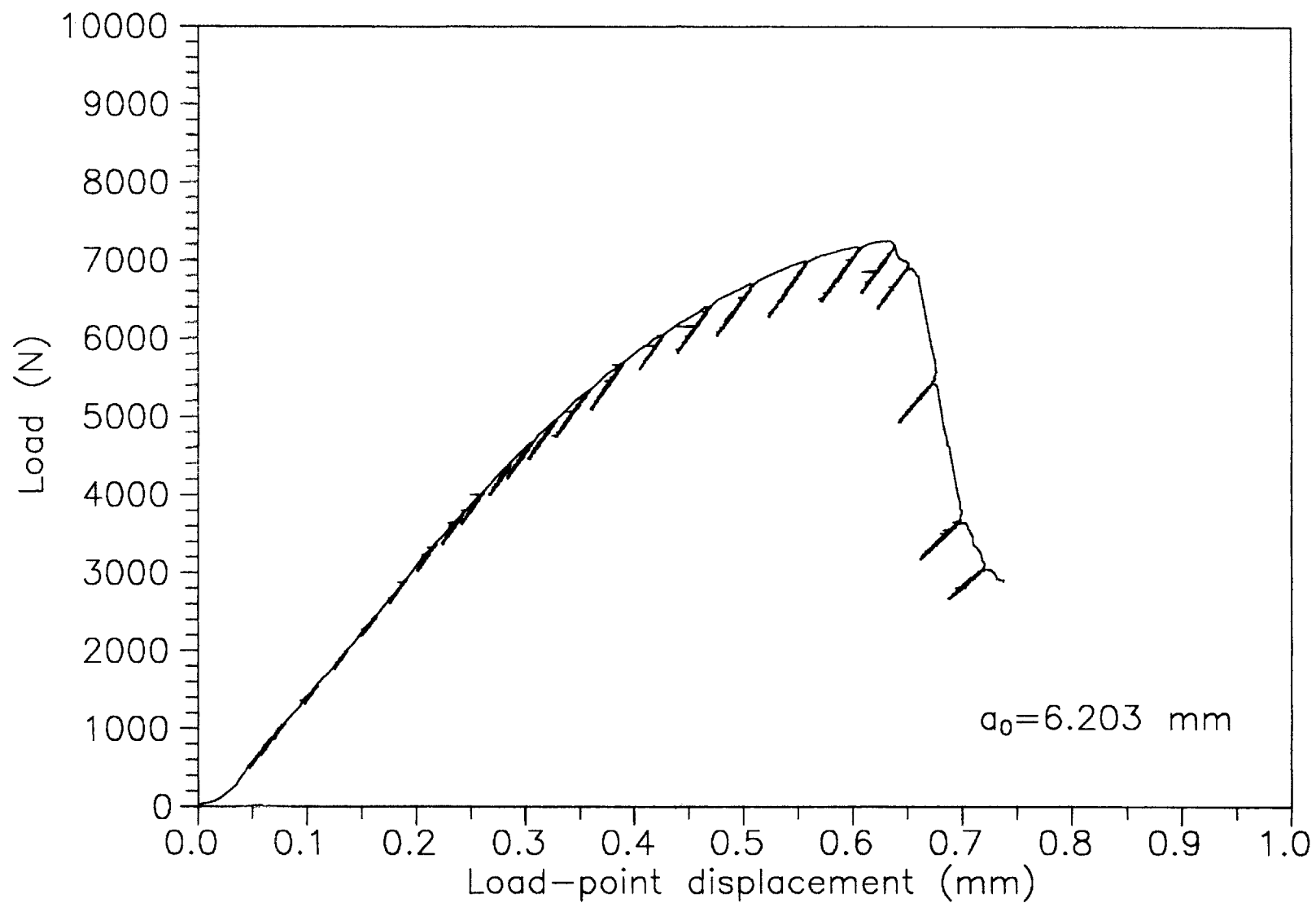
2. C-C. Young, "Transformation Toughening in Phosphocarbide-Strengthened Austenitic Steels," Doctoral Thesis, Department of Materials Science and Engineering, Massachusetts Institute of Technology, Cambridge, MA (1988).

3. G.B. Olson, "A Mechanism for the Strain-Induced Nucleation of Martensitic Transformations," *J. Less-Common Metals* **28** (1972) 107-118.

4. G.B. Olson and M. Azrin, "Transformation Behavior of TRIP Steels," *Met. Trans.* **9A** (1978) 713-721.

5. Z. Nishiyama, *Martensitic Transformation*, Academic Press, Inc., New York, NY (1978).

6. L.A. Carapella, "Computing A" or M_S (Transformation Temperature on Quenching) From Analysis," *Met. Progr.* **46** (1944) 108.

7. K.W. Andrews, "Empirical Formulae for the Calculation of some Transformation Temperatures," *JISI* **203** (1965) 721-727.

8. S.A. Kulin, Morris Cohen and B.L. Averbach, "Effect of Applied Stress on the Martensitic Transformation," *Trans. AIME* **194** (1952) 661-668.

9. J.R. Patel and Morris Cohen, "Criterion for the Action of Applied Stress in the Martensitic Transformation," *Acta Met.* **1** (1953) 531-538.

10. G.B. Olson and Morris Cohen, "Stress-Assisted Isothermal Martensitic Transformation: Application to TRIP Steels," *Met. Trans.* **13A** (1982) 1907-1914.

11. J.R.C. Guimarães and J.C. Gomes, "The Influence of Prior Deformation on the Yield Stress of a Metastable Fe-Ni-C Austenite," *J. Mat. Sci. Lett.* **12** (1977) 2534-2537.

12. I. Tamura, T. Maki, H. Hato, Y. Tomota and M. Okaoa, "Strength and Ductility of Austenitic Iron Alloys Accompanying Strain-Induced Martensitic Transformation," *Second International Conference on the Strength of Metals and Alloys,* Asilomar Conference Grounds, Pacific Grove, CA, 1970, American Society for Metals, Metals Park, OH (1970) 900-904.

13. J.A. Venables, "The Martensite Transformation in Stainless Steel," *Phil. Mag.* **7** (1962) 35-44.

14. R. Lagneborg, "The Martensite Transformation in 18% Cr-8% Ni Steels," *Acta. Met.* **12** (1964) 823-843.

15. F. Lecroisey and A. Pineau, "Martensitic Transformations Induced by Plastic Deformation in the Fe-Ni-Cr-C System," *Met. Trans.* 3 (1972) 387-396.

16. T. Angel, "Formation of Martensite in Austenitic Stainless Steels: Effects of Deformation, Temperature, and Composition," *J. Iron Steel Inst.* 177 (1954) 165-174.

17. G.B. Olson and Morris Cohen, "Kinetics of Strain-Induced Martensitic Nucleation," *Met. Trans.* 6A (1975) 791-795.

18. D. Fahr, "Stress- and Strain-Induced Formation of Martensite and its Effects on Strength and Ductility of Metastable Austenitic Stainless Steels," *Met. Trans.* 2 (1971) 1883-1892.

19. G.W. Powell, E.R. Marshall and W.A. Backofen, "Strain Hardening of Austenitic Stainless Steel," *Trans. ASM* 50 (1958) 478-497.

20. J.P. Bressanelli and A. Moskowitz, "Effects of Strain Rate, Temperature, and Composition on Tensile Properties of Metastable Austenitic Stainless Steels," *Trans. ASM* 59 (1966) 223-239.

21. G.B. Olson, K. Tsuzaki and Morris Cohen, "Statistical Aspects of Martensitic Nucleation," *Mat. Res. Soc. Symp. Proc.* 57 (1987) 129-148.

22. T. Narutani, G.B. Olson and Morris Cohen, "Constitutive Flow Relations for Austenitic Steels During Strain-Induced Martensitic Transformation," *J. de Physique* 43(C4) (1982) 429-434.

23. R.G. Stringfellow, "Mechanics of Strain-Induced Transformation Plasticity," Masters' Thesis, Department of Mechanical Engineering, Massachusetts Institute of Technology, Cambridge, MA (1988).

24. R.G. Stringfellow, Doctoral Research in Progress, Department of Mechanical Engineering, Massachusetts Institute of Technology, Cambridge, MA, (1990).

25. A. Needleman and J.R. Rice, "Void Nucleation Effects on Shear Localization in Plastic Solids" in: *Mechanics of Sheet Metal Forming,* D.P. Koistinen and N.W. Wang, eds., Plenum Publishing Company, New York, NY (1978) 237.

26. J.R. Rice, "A Path Independent Integral and the Approximate Analysis of Strain Concentration by Notches and Cracks," *J. Appl. Mech.* 35 (1968) 379-386.

27. J.W. Hutchinson, "Singular Behavior at the end of a Tensile Crack in a Hardening Material," *J. Mech. Phys. Solids* 16 (1968) 13-31.

28. J.R. Rice and G.F. Rosengren, "Plane Strain Deformation near a Crack Tip in a Power-Law Hardening Material," *J. Mech. Phys. Solids* 16 (1968) 1-12.

29. J.R. Rice, P.C. Paris and J.G. Merkle, "Some Further Results of J-Integral Analysis and Estimates" in: *ASTM STP 536,* American Society for Testing and Materials, Philadelphia, PA (1973) 231-245.

30. J.W. Hutchinson, "Chapter 13. J-Integral Testing" in: *Nonlinear Fracture Mechanics*, Department of Solid Mechanics, The Technical University of Denmark, Lyngby, Denmark (1979) 63-69.

31. "E 813-81: Standard Test for J_{IC}, A Measure of Fracture Toughness" in: *Metals-Mechanical Testing; Elevated and Low-Temperature Tests; Metallography*, 1987 Annual Book of ASTM Standards, Vol. 03.01, American Society for Testing and Materials, Philadelphia, PA (1987) 810-828.

32. Metals Handbook 9th ed., *Volume 3, Properties and Selection: Stainless Steels, Tool Materials, and Special-Purpose Metals*, American Society for Metals, Metals Park, OH (1980).

33. William F. Smith, *Structure and Properties of Engineering Alloys*, McGraw-Hill, Inc., New Work, NY (1981) 270-314.

34. G. Krauss, "Chapter 12: Stainless Steels" in: *STEELS: Heat Treatment and Processing Principles*, ASM International, Materials Park, OH (1990) 351-399.

35. A.K. Sinha, "Section 4.7: Precipitation Hardening" in: *Ferrous Physical Metallurgy*, Butterworth Publishers, Stoneham, MA (1989) 150-184.

36. H.J. Rack and David Kalish, "The Strength, Fracture Toughness, and Low Cycle Fatigue Behavior of 17-4 PH Stainless Steel," *Met. Trans.* 5 (1974) 1595-1605.

37. S. Paetke and A.R. Waugh, "A Study of the Precipitation Reactions in a 17/7 PH Stainless Steel, Using an IAP Atom-probe," *Proceedings of an International Conference on Solid-Solid Phase Transformations*, Carnegie-Mellon University, Pittsburgh, PA, August 10-14, 1981, H.I. Aaronson, D.E. Laughlin, R.F. Sekerka and C.M. Wayman, eds., The Metallurgical Society of AIME, Warrendale, PA (1982) 769-773.

38. T.J. Headley, M.M. Karnowsky and W.R. Sorensen, "Effect of Composition and High Energy Rate Forging on the Onset of Precipitation in an Iron-Base Superalloy," *Met. Trans.* 13A (1982) 345-353.

39. D.R. Muzyka, "The Metallurgy of Nickel-Iron Alloys" in: *The Superalloys*, C.T. Sims and W.C. Hagel, eds., John Wiley & Sons, Inc., New York, NY (1972) 113-143.

40. *ARMCO Precipitation-Hardening Stainless Steels*, ARMCO, Inc., Middletown, OH (1984).

41. *Carpenter Stainless Steels*, Carpenter Technology Corporation, Reading, PA (1987).

42. D.C. Perry and J.C. Jasper, "Structure and Constitution of Wrought Precipitation-Hardenable Stainless Steels" in: *Handbook of Stainless Steels*, D. Peckner and I.M. Bernstein, McGraw-Hill, Inc., New York, NY (1977).

43. S. Jin, Jr J.W. Morris and Y.L. Chen, "An Investigation of Transformation Strengthening in Precipitation-Hardened Fe-Ni Austenite," *Met. Trans.* 9A (1978) 1625-1633.

44. L. Kaufman, *Manlabs-NPL Thermochemical Database*, Cambridge, MA (1977).

45. K.M. Delargy and G.D.W. Smith, "Phase Composition and Phase Stability of a High-Chromium Nickel-Based Superalloy, IN939," *Met. Trans.* 14A (1983) 1771-1783.

46. "E 112-85: Standard Methods for Determining the Average Grain Size" in: *Metals-Mechanical Testing; Elevated and Low-Temperature Tests; Metallography*, 1987 Annual Book of ASTM Standards, Vol. 03.01, American Society for Testing and Materials, Philadelphia, PA (1987) 403-436.

47. A.W. Thompson, "Calculation of True Volume Grain Diameter," *Metallog.* 5 (1972) 366-369.

48. J.B. Nelson and D.P. Riley, "An experimental investigation of extrapolation methods in the derivation of accurate unit-cell dimensions of crystals.," *Proc. Phys. Soc.* 57 (1945) 160-177.

49. A. Taylor and H. Sinclair, "On the determination of lattice parameters by the Debye-Scherrer method," *Proc. Phys. Soc.* 57 (1945) 126-135.

50. "E 399-83: Standard Test Method for Plane Strain Fracture Toughness of Metallic Materials" in: *Metals-Mechanical Testing; Elevated and Low-Temperature Tests; Metallography*, 1987 Annual Book of ASTM Standards, Vol. 03.01, American Society for Testing and Materials, Philadelphia, PA (1987) 680-715.

51. K. Hellan, *Introduction to Fracture Mechanics*, McGraw-Hill, Inc., New York, NY (1984).

52. G.E. Dieter, *Mechanical Metallurgy*, 2nd ed., McGraw-Hill, Inc., New York, NY (1976) 513.

53. UnkelScope Level 2 Plus, Ver. 2.45, Unkel Software Inc., Lexington, MA (1987).

54. G.B. Olson, "Transformation Plasticity and the Stability of Plastic Flow," *1982 ASM Materials Science Seminar, "Deformation, Processing, and Structure"*, St. Louis, MO, October 23-24, 1982, G. Krauss, ed., American Society for Metals, Metals Park, OH (1983) 391-424.

55. A.J. McEvily, jr. and R.C. Boettner, "On Fatigue Crack Propagation in FCC Metals," *Acta Met.* 11 (1963) 725-743.

56. H. Ishii and J. Weertman, "Fatigue Crack Propagation in Copper and Cu-Al Single Crystals," *Met. Trans.* 2 (1971) 3441-3452.

57. J.T. McGrath and R.C.A. Thurston, "The Effect of Cross Slip on the Fatigue Behavior of Copper and Copper-Zinc Alloys," *Trans. TMS-AIME* 227 (1963) 645-650.

58. G.A. Miller, D.H. Avery and W.A. Backofen, "Fatigue-Crack Growth in Some Copper-Base Alloys," *Trans. TMS-AIME* 236 (1966) 1667-1673.

59. B.L. Bramfitt and A.R. Marder, "Splitting Behavior in Plate Steels," *Toughness Characterization and Specifications for HSLA and Structural Steels,* Atlanta, GA, March 6-10, 1977, P.L. Mangonon, jr., ed., The Metallurgical Society of AIME, New York, NY (1979) 236-256.

60. D.M. Haezebrouck, Unpublished research, MIT, (1988).

61. G.B. Olson and Morris Cohen, "Dislocation Theory of Martensitic Transformations" in: *Dislocations in Solids,* Vol. 7, F.R.N. Nabarro, ed., North-Holland Physics Publishing, Amsterdam, The Netherlands (1986) 295-407.

62. F.R.N. Nabarro, "Solution Hardening" in: *Dislocations and Properties of Real Materials,* The Institute of Metals, London, England (1985) 152-169.

63. R. Labusch, "A Statistical Theory of Solid Solution Hardening," *Phys. Stat. Sol.* **41** (1970) 659-669.

64. R.G. Stringfellow, D.M. Parks and G.B. Olson, "A Constitutive Model for Strain-Induced Transformation Plasticity in Metastable Austenitic Steels," To be published.

65. R.G. Stringfellow and D.M. Parks, "A Self-Consistent Model of Isotropic Viscoplastic Behavior in Multiphase Materials," To be published in: *Int. J. Plast.*

66. "Chapter 9" in: *Formelsamling i Hållfasthetslära,* G. Hedner, Vol. 8th, Institutionen för Hållfasthetslära, Stockholm, Sweden (1978) 51-63.

67. H. Tada, P.C. Paris and G.R. Irwin, *The Stress Analysis of Cracks Handbook,* Del Research Corporation, Hellertown, PA (1974).

68. D.A. Jablonski, B. Journet, R.S. Vecchio and R. Hertzberg, "Compliance Functions for Various Fracture Mechanics Specimens," *Eng. Fract. Mech.* **22** (1985) 819-827.

69. A. Saxena and S.J. Hudak, "Review and Extension of Compliance Information for Common Crack Growth Specimens," *Int. J. of Fract.* **14** (1978) 453-468.

BIOGRAPHICAL NOTE

The author was born November 28, 1958 in Odda, Norway where he lived until 1965 when the family moved to Sweden. After one year in Västerås the family finally settled down in Torshälla where he graduated from Gökstensskolan in 1974. The same year he enrolled in the four-year engineering high school program at Rinmansskolan, Eskilstuna from where he graduated with a Mechanical Engineering degree in 1978. During the academic year of 1978-79 he worked as a high school teacher at Djurgårdsskolan, Eskilstuna, and during 1979-80 at Oskarsströmskolan, Oskarsström, teaching math and physics both years. From 1977-1980 he also played volleyball in the highest league in Sweden, winning a bronze medal for the 1977-78 season with Eskilstuna Finska Förening, and another bronze medal for the 1979-80 season with Åtradalens Volleybollklub. During these years he participated in numerous national and international tournaments with both teams. In the fall of 1980 he enrolled in the Metallurgy and Materials Technology program at the Royal Institute of Technology in Stockholm. Having won a scholarship at the Royal Institute of Technology to study the last year abroad, he came to MIT for the academic year 1983-84 to attend classes. After completion of classes and a thesis project at MIT, he returned to the Royal Institute of Technology, graduating in 1984 with a Master of Science degree. In the fall of 1984 he returned to MIT and enrolled in the Doctoral program in the Department of Materials Science and Engineering. Following graduation, he will assume a research position in industry.